SOFOS -
A new Satellite-based Operational Fog Observation Scheme

Dissertation
zur
Erlangung des Doktorgrades
der Naturwissenschaften
(Dr. rer. nat.)

dem
Fachbereich Geographie
der Philipps-Universität Marburg
vorgelegt von

Jan Cermak
aus Viernheim

Marburg / Lahn 2006

Eine gedruckte Ausgabe dieser Dissertation wird in der Reihe
“Marburger Geographische Schriften” erscheinen.
This thesis will appear in print as a volume of the
“Marburger Geographische Schriften”.

Vom Fachbereich Geographie
der Philipps-Universität Marburg als Dissertation
am 25. April 2006 angenommen.

Erstgutachter: Prof. Dr. Jörg Bendix (Marburg)
Zweitgutachter: Prof. Dr. Eberhard Parlow (Basel)
Drittgutachter: Prof. Dr. Wilfried Endlicher (Berlin)

Tag der mündlichen Prüfung: 6. Juli 2006

Mist

Low-anchored cloud,
Newfoundland air,
Fountain head and source of rivers,
Dew-cloth, dream drapery,
And napkin spread by fays;
Drifting meadow of the air,
Where bloom the dasied banks and violets,
And in whose fenny labyrinth
The bittern booms and heron wades;
Spirit of the lake and seas and rivers,
Bear only purfumes and the scent
Of healing herbs to just men's fields!

Henry David Thoreau (1817 - 1862)

Preface

In a colloquial and poetical context, fog is frequently used as a symbol for disorientation and loneliness. I am very fortunate to say that these are not the primary sentiments I associate with the past months and my work on this thesis. The encouragement and support I received were manifold and I am grateful to a large number of organizations, colleagues and friends for their presence in this "fenny labyrinth".

With special gratitude I acknowledge the extensive counsel and backing by my supervisor Jörg Bendix. He at all times met my requests with open ears and was always ready to provide any support needed. I thank him for opening many doors to me, not least the door to the the cosmos of fog detection.

My colleagues at the Laboratory for Climatology and Remote Sensing were of particular help. I thank them for their support ranging from little everyday matters to being open-minded discussants in in-depth scientific discourse. I especially thank Christoph Reudenbach (now GIS section) and Thomas Nauß for many fruitful exchanges and scientific discussions as well as for helpful comments on the manuscript. A Diplom dissertation prepared by Boris Thies was of great use as a precursor study for this work, as were a study by Jonas Vogel and the help of my student assistants, Jan Lange, Katharina Appel, Monika Weißschnur. I thank Maik Dobbermann for his patience and enthusiasm in weaving a technical net around the vagaries of scientific output.

I am very thankful to many colleagues within the ESF COST actions 720 and 722 for the numerous enlightening discussions and suggestions, particularly to Otto Hyvärinen (Finnish Meteorological Institute, FMI), Marc Schneebeli (University of Bern), Daniela Nowak (ETH Zürich, MeteoSwiss), Matthieu Masbou (University of Bonn), Mathias Müller (University of Basel) and Ismail Gultepe (Environment Canada).

Many colleagues and organizations provided the data basis for this work and validation studies. Meteosat Second Generation (MSG) data was kindly

provided by EUMETSAT during the system's commissioning phase already, within the EUMETSAT/ESA MSG Principal Investigator Programme. Validation and intercomparison data was made available by Peter Bissoli (Deutscher Wetterdienst, DWD); the Cloudnet project (Ewan O'Connor, University of Reading, and Ulrich Görsdorf, DWD); members of the ESF COST720 action (Dominique Ruffieux, MeteoSwiss; Darren Lyth, UK MetOffice; Christian Mätzler, University of Bern); Otto Klemm (University of Münster); Dario Cano (Instituto Nacional de Meteorologia, INM); and Thierry Bergot (Météo-France).

Another fundamental contribution to this thesis came from the open source software community. Large parts of the work were made possible or significantly eased by free software tools. Not the least of these are the GNU Emacs editor within which this thesis was typed, and the LaTeX system.

The project around this thesis was made possible by financial support from the Deutsche Forschungsgemeinschaft (DFG) within the NEKAMM project (BE 1780/8-1; 8-3). This is gratefully acknowledged.

Finally, I thank my parents for their support and encouragement throughout my education, and my partner Katja for enduring my quest for fog and for reminding me of the real priorities in life whenever needed.

Jan Cermak
Marburg, April 2006

Contents

List of Figures **v**

List of Tables **ix**

List of Acronyms **x**

List of Symbols **xiii**

1 Motivation, Aims and Outline **1**
1.1 Why Fog? 1
1.2 Why Satellites? 3
1.3 Aim of this Work and Outline 4

2 Conceptual Design **7**
2.1 Fog Processes and Properties 7
2.2 Approaches to Fog Detection 11
2.3 SOFOS Design 15

3 Data, Models and Operational Framework **20**
3.1 Satellite Data – The MSG SEVIRI System 20
3.2 Ancillary Data and Models 21
3.2.1 Synoptical Data 21
3.2.2 Digital Elevation Model 23
3.2.3 Radiative Transfer Model 24
3.3 FMet: An Operational Framework Including Data Processing 24
3.3.1 MetGet: Raw Data Handling and Import 25
3.3.2 MetGeo: Geolocation and Geometry 27
3.3.3 MetCal: Image Calibration 28
3.3.4 MetProd: Operational Product Generation 28
3.3.5 MetOut: Output Formatting 29
3.4 Auxiliary Satellite Products 29

4 Method Development **36**
4.1 Theoretical Basis . . . 37
4.1.1 The Theoretical Challenge: Inverse Problems . . . 37
4.1.2 Cloud Properties and Their Effect on Radiative Transfer 38
4.2 Detection of Very Low Stratus . . . 43
4.2.1 Cloud Identification . . . 45
4.2.2 Snow Pixel Elimination . . . 49
4.2.3 Cloud Phase Determination . . . 50
4.2.4 Small Droplet Proxy Test . . . 53
4.2.5 Spatial Entity Identification . . . 56
4.2.6 Stratiformity Test . . . 58
4.2.7 Very Low Cloud Plausibility Test . . . 58
4.3 Cloud Top Height Determination . . . 61
4.3.1 Existing Approaches . . . 61
4.3.2 Method Design and Implementation . . . 63
4.4 Cloud Geometrical Thickness . . . 70
4.4.1 Physical Basis . . . 70
4.4.2 Approaches to Cloud Geometry Retrieval . . . 73
4.4.3 Vertical Stratification of Fog and Very Low Stratiform Clouds . . . 77
4.4.4 Development and Implementation of a Cloud Water Model . . . 81

5 Validation and Appraisal **91**
5.1 Validation Approach . . . 91
5.1.1 Aims and Data Selection . . . 91
5.1.2 Sources of Uncertainty . . . 93
5.1.3 Intercomparison Methodology . . . 95
5.2 Validation Study . . . 98
5.2.1 Product Data Set . . . 98
5.2.2 Very Low Cloud/Ground Fog Plus Elevated Fog . . . 100
5.2.3 Ground Fog . . . 105
5.3 Validation Summary . . . 111

6 Summary and Outlook **113**
6.1 Summary . . . 113
6.2 Outlook . . . 116

Zusammenfassung **121**

Bibliography **125**

List of Figures

1.1 The effect of clouds at various altitudes on global warming/cooling of the earth surface as a function of liquid water path or ice water path. 2
1.2 Structure of this work. Bold numbers on the left are chapter and section numbers. 5

2.1 Emissivities as a function of droplet size and wavelength vs. cloud optical depth, after HUNT (1973). 14
2.2 Concept I: Low stratus delineation requires the separation of competing surfaces in the 2-dimensional domain. 16
2.3 Concept II: Ground fog detection requires knowledge of cloud geometry, i.e. 3-dimensional information on the cloud, including its boundaries (z_t and z_b) and thickness (Δ_z), and surface elevation z_s. 17
2.4 Overview of SOFOS. The major steps, Very low stratus delineation and very low stratus geometry retrieval are embedded in an operational context. 18
2.5 Approximate study area, presented as a clear sky broadband surface reflection map for a summer day. 19

3.1 SEVIRI spatial coverage, presented as a false-colour composite image (1.6 μm: red, 0.8 μm: green, 0.6 μm: blue). 22
3.2 Sites of airports with METAR within the study region. 23
3.3 Overview of the FMet scheme. Explanations see text. 26
3.4 Precipitable water computed with two different methods, 1130 UTC, 16 August 2005. 32
3.5 Example for spatial skin temperature interpolation, 1030 UTC, 16 January 2005, for a region around the Alps 35

4.1 The path of a radiation quantity I_λ through a cloudy atmosphere. 39

4.2 An overview of the fog/very low stratus area delineation algorithm. 44
4.3 Earth and sun electromagnetic spectra. 45
4.4 Blackbody temperature difference $T_{10.8} - T_{3.9}$ for 1000 UTC, 5 November 2003. 47
4.5 Frequency distribution of $T_{10.8} - T_{3.9}$ for 5 November 2003, 1000 UTC (left) and 18 April 2004, 1600 UTC (right). 48
4.6 The sum of VIS and NIR reflectances Σr vs. the difference of both reflectances Δr as used in the Normalised Difference Snow Index (NDSI). 51
4.7 Imaginary part of the refractive index (absorption) for liquid water and ice in part of the infrared. 52
4.8 Viewing zenith angle θ vs. blackbody temperature difference $\Delta T_{12.0-8.7\mu m}$ for clouds in the water and ice phases. 53
4.9 Middle infrared intensity $I_{3.9\mu m}$ as a function of droplet radius a_e and viewing zenith angle θ for a water cloud with a thickness of 200 m. 54
4.10 A 3.9 μm radiance image for 5 December 2003, 1300 UTC and the corresponding 0.6 μm visible image. 55
4.11 A profile of radiances registered in the 3.9 μm channel over central France, 5 December 2003, 1300 UTC. 55
4.12 Water cloud entities as identified in the course of very low stratus detection scheme. 57
4.13 Very low stratus/cloud classification for 5 November 2003, 1000 UTC. 60
4.14 Overview of the cloud top height scheme. 64
4.15 Criteria for DEM selection. 66
4.16 The concept of the margin height extraction scheme. 67
4.17 The concept of the height determination scheme using an environmental lapse rate. 68
4.18 Radio soundings of temperature and humidity for 1200 UTC, 16 January 2005, with cloud top heights computed from satellite imagery. 69
4.19 Imaginary part of the refractive index (absorption) for liquid water and ice. 71
4.20 The dependence of middle infrared (3.9 μm) and visible range (0.6 μm) reflectances on cloud optical depth and droplet effective radius. 72
4.21 Geometrical thickness retrieved using a range of approaches presented in the text. 76

4.22 Processes in fog and very low stratus development. 79
4.23 Overview of the cloud base height retrieval scheme. 82
4.24 The cloud profile parameterisation used for cloud liquid water path computation. 84
4.25 Dependence of simulated cloud thickness on liquid water path and cloud top temperature, at a constant cloud top height of 500 m above ground. 86
4.26 A low stratus cloud profile observed by SLINGO *et al.* (1982), with a cloud base of 745 m. 86
4.27 Deviation of the computed cloud base height from observed cloud base height in metres as a function of β, cloud base transition and cloud top transition. 87
4.28 A ground fog profile taken from PINNICK *et al.* (1978). 88
4.29 A profile of uplifted fog as reported by PINNICK *et al.* (1978) with a cloud base height of 57.5 m. 89

5.1 Share of low water cloud pixels in each scene, from the first to the last scene in the data set (abscissa in % of total scenes used, chronological order). 99
5.2 Share of ground fog pixels in each scene, from the first to the last scene in the data set (abscissa in % of total scenes used, chronological order). 99
5.3 Threat scores by station for the validation study period (3 by 3 pixel approach). 101
5.4 Simplified satellite cloud classification and corresponding METAR observations, 1030 UTC, 8 November 2005. 103
5.5 10.8 μm channel blackbody temperature image, as a complement to figure 5.4. 104
5.6 Distribution of missed low cloud situations by cloud cover classes. 105
5.7 Cloud cover observed at METAR stations compared with the satellite classification, 0900 UTC, 22 September 2005. 106
5.8 Reflectance measured in the 0.6 μm channel, 0900 UTC, 22 September 2005. 107
5.9 Threat scores by station for the validation study period (3 by 3 pixel approach) for ground fog presence. 110
5.10 The skill of the fog detection algorithm at different ground fog confidence levels. 111

6.1 Number of days with daytime very low stratus cover in 2004, based on 12823 scenes (366 days). 117
6.2 Hours with daytime ground fog in the study area, December 2004, based on 1665 scenes (31 days). 118
6.3 Hours with daytime ground fog in and around Germany, December 2004, based on 1665 scenes (31 days). 119

List of Tables

3.1 SEVIRI channels, (Schmetz *et al.*, 2002). 21

4.1 NDSI values modelled for various surfaces. 50
4.2 Comparison of cloud base heights for the profiles presented in figures 4.26, 4.28 and 4.29 by different methods. 89

5.1 Contingency table. A: Correctly identified situations (hits), B: False alarms, C: Misses, D: Correct negatives. 96
5.2 Statistical indicators used in this study, with computation, theoretical range of values and best value (for a maximum skill prediction). 97
5.3 Shares of individual (cloud) classes in percent of the total area of the 1030 scenes considered. 98
5.4 Statistical summary of the very low cloud validation study for the single-pixel approach and the 3 by 3 pixel environment. 100
5.5 Statistical summary of the ground fog validation study for the single-pixel approach and the 3 by 3 pixel environment, using elevation data from a digital elevation model at satellite spatial resolution. 108
5.6 Statistical summary of the ground fog validation study for the single-pixel approach and the 3 by 3 pixel environment, using real elevation data for each ground station. 108

List of Acronyms

AVHRR	Advanced Very High Resolution Radiometer
CCN	Cloud condensation nuclei
CERES	Clouds and the Earth's Radiant Energy System
COST	Co-operation in the field of Scientific and Technical Research
DEM	Digital elevation model
DWD	Deutscher Wetterdienst
ECMWF	European Centre for Medium Range Forecasting
EKU	EUMETCast Key Unit
ESA	European Space Agency
ESF	European Science Foundation
EUMETCast	EUMETSAT Broadcast system for Environmental Data
EUMETSAT	European Organisation for the Exploitation of Meteorological Satellites
FMet	Framework for Meteosat data processing
GEO	Geostationary
GERB	Global Earth Radiation Budget
GMS	Geostationary Meteorological Satellite
GOES	Geostationary Operational Environmental Satellite

HRIT	High Rate Information Transmission
HRV	High Resolution Visible
IR	Infrared
ISCCP	International Satellite Cloud Climatology Project
IWP	Ice water path
LEO	Low earth orbiting
Lidar	Light detection and ranging
LUT	Look-up table
LWP	Liquid water path
METAR	METeorological Aerodrome Report
MIR	Middle infrared
MODIS	Moderate Resolution Imaging Spectroradiometer
MSG	Meteosat Second Generation
MSS	Marburg Satellite Station
NDSI	Normalised Difference Snow Index
NDVI	Normalised Difference Vegetation Index
NOAA	National Oceanic and Atmospheric Administration
NRT	Near-real-time
RAO	Research Announcement of Opportunity
RTC	Radiative transfer computations
SAFNWC	EUMETSAT Nowcasting Satellite Application Facility
SEVIRI	Spinning-Enhanced Visible and Infrared Imager
SOFOS	Satellite-based Operational Fog Observation Scheme
SST	Sea surface skin temperature
UTC	Universal time co-ordinated

VAS	Visible and Infrared Spin Scan Radiometer Atmospheric Sounder
WMO	World Meteorological Organization

List of Symbols

Symbol	Meaning	Units
a	Droplet radius	μm
a_e	Droplet effective radius	μm
a_n	Equivalent nucleus radius	μm
A	Albedo	
β	Turbulent mixing parameter	
β_a	Absorption coefficient	m^{-1}
β_e	Extinction coefficient	m^{-1}
β_s	Scattering coefficient	m^{-1}
c	Speed of light	$m\,s^{-1}$
C_w	Moist adiabatic condensate coefficient	$g\,m^{-3}\,m^{-1}$
Δ_z	Cloud geometrical thickness	m
ϵ	Emissivity	
ε	Contrast threshold	
E_i	Spectrally integrated extraterrestrial irradiance in channel i	$W\,m^{-2}\,\mu m^{-1}$ or $W\,m^{-2}\,cm$
$F_\odot$	Incident solar flux density	$W\,m^{-2}$
$F\uparrow$	Flux density reflected to space	$W\,m^{-2}$
Γ	Atmospheric temperature lapse rate	$K\,m^{-1}$
h	Planck constant	$J\,s$
H_T	Rate of temperature change	$K\,s^{-1}$
I	Spectral intensity (spectral radiance)	$W\,m^{-2}\,sr^{-1}\,\mu m^{-1}$ or $W\,m^{-2}\,sr^{-1}\,cm$

Symbol	Meaning	Units
k	Boltzmann constant	$J\,K^{-1}$
k_λ	Mass extinction cross section at λ	$m^2\,g^{-1}$
λ	Wavelength	μm
L	Latent heat of vapourisation	$J\,kg^{-1}$
L_i	Spectral irradiance in channel i	$W\,m^{-2}\,\mu m^{-1}$
m_l	Liquid water mixing ratio	$g\,kg^{-1}$
m_l^{ad}	Adiabatic liquid water mixing ratio	$g\,kg^{-1}$
m_v	Water vapour mixing ratio	$g\,kg^{-1}$
n	Noise quantity	
p	Pressure level	hPa
p'	Atmospheric vapour pressure	hPa
p_a	Saturation vapour pressure around a spherical body with radius a	hPa
p_e	Equivalent saturation vapour pressure	hPa
p_s	Saturation vapour pressure	hPa
P_c	Cloud confidence level	
ϕ_e	Longitude on earth	
ϕ_n	Nadir longitude	
ψ	Relative azimuth angle	
q	Air humidity	%
Q_e	Extinction efficiency factor	
r_λ	Reflectance at wavelength λ	
R_v	Gas constant	$J\,kg^{-1}\,K^{-1}$
ρ_a	Density of air	$g\,m^{-3}$
ρ_c	Cloud liquid water content (concentration)	$g\,m^{-3}$
ρ_c^{ad}	Adiabatic cloud liquid water content	$g\,m^{-3}$
ρ_l	Density of liquid water	$g\,m^{-3}$
σ	Surface tension	$J\,cm^{-2}$
sr	Steradian	
t_c	Cloud transmissivity	
T	Temperature (type depends on subscript)	K
T_a	Air temperature	K
T_t	Cloud top temperature	K

Symbol	Meaning	Units
T_i	Observed black body temperature in channel i	K
T_s	Surface temperature	K
T_λ	Black body temperature at $\lambda\,\mu$m	K
τ	Optical depth	
θ	Viewing/satellite zenith angle	
θ_0	Solar zenith angle	
U	Total precipitable water column	$g\,cm^{-2}$
v	Any data value	
v_t	Threshold value	
V	Visibility/visual range	m
W	Cloud liquid water path	$g\,m^{-2}$
W^{ad}	Adiabatic cloud liquid water path	$g\,m^{-2}$
x	Size factor	
z	Height	m
z_b	Cloud base height	m
z_s	Surface height	m
z_t	Cloud top height	m

Chapter 1

Motivation, Aims and Outline

1.1 Why Fog?

Fog impacts on a wide range of areas; it is a phenomenon with meteorological and climatological, economical and ecological, hygienic and aesthetic ramifications, evasive and impenetrable, dispiriting and inspiration for poetry, all at the same time. From a scientific and socio-economical point of view, fog is of importance as a modifier within the climate system, as an obstruction to traffic and for its association with air quality impairment.

The presence of low clouds alters the radiative budget of the earth-atmosphere system and thus has an important impact on climatic warming (Houghton *et al.*, 2001). Most commonly, low clouds are expected to have a stronger cooling effect than clouds at higher altitudes, with slight latitudinal effects (cf. the review by Stephens, 2005). This relationship is exemplified in figure 1.1, where expected surface temperature change is shown for clouds at three levels as a function of cloud thickness. The cooling effect is further enhanced by the droplet number concentration within a cloud. Increased (anthropogenic) production of aerosols in this way enhances cloud radiative forcing and thus radiative cooling ('Twomey effect', Twomey, 1977a; Duda *et al.*, 1996; Baker, 1997; Taylor *et al.*, 2000). Generally, a reduced frequency of low cloud occurrence is thought to enhance global warming, while an increased frequency would probably slow down this process. Detailed climatological information on fog and low cloud occurrence would therefore be a significant contribution to climate change modelling (Duda *et al.*, 1996).

Apart from these considerations concerning future effects, fog situations present a very tangible obstruction to traffic at land, at sea and in the

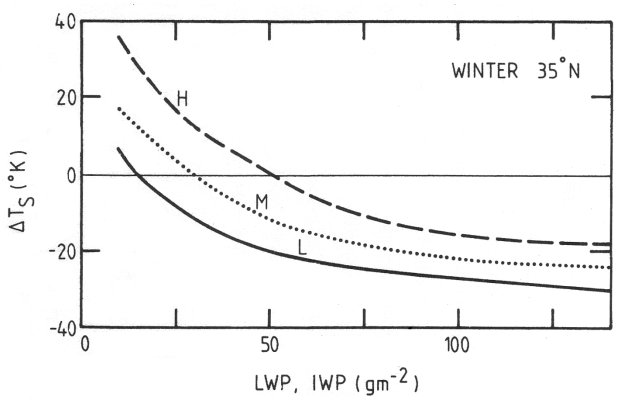

Figure 1.1: *The effect of clouds at various altitudes on global warming/cooling of the earth surface (ΔT_S) as a function of liquid water path (LWP) or ice water path (IWP), a measure of cloud thickness. Low-level clouds (L) are expected to have stronger cooling effects than higher-level clouds (M and H), as indicated by the relative positions of the corresponding lines. The winter situation shown is valid for 35° N. Figure taken from* Stephens & Webster *(1981).*

air (Andre *et al.*, 2004; Pagowski *et al.*, 2004). In a study centred on Sydney airport, Leigh (1995) put the economic value of information on both storms and low visibility events at around 7 million Australian dollars (about 5.2 million US dollars at the time) per year for this airport alone.

In continental areas, fog is associated with air quality impairment. Especially in industrialised areas, air pollutants are trapped under temperature inversions associated with fog. The bright top of the fog layer acts as a cooling surface and delays the thermal dissipation of the inversion. Air pollutants are frequently the nuclei in fog droplets and can be deposited in large concentrations along with these. Severe winter smog episodes can be closely related to fog occurrence (Jaeschke *et al.*, 1998; Fuzzi *et al.*, 1984; Kraus & Ebel, 1989; Bendix, 1998, 2002).

Research and applications in climatology, traffic safety and air quality studies equally depend on reliable information on fog occurrence. Ideally, information on fog presence, persistence and properties is needed:

- At a high spatial resolution, in order to accurately map the effects and impediments associated with fog.
- At a high temporal resolution (i.e., frequently updated), to allow for continuous monitoring of the phenomenon in nowcasting systems, i.e. schemes aimed at the assessment of the present state of meteorological parameters, and very short-range forecasts (Browning, 1982).

- For long time series, to allow for aggregate analysis and the study of long-term effects.

This need has been widely recognised and led to a number of cooperations and initiatives such as action 722 of the European Science Foundation (ESF) Co-operation in the field of Scientific and Technical Research (COST) programme, which is specifically concerned with the nowcasting and very short-range forecasting of fog and low clouds (Jacobs *et al.*, 2005).

In the light of these applications, reliable fog detection and mapping in the way outlined above would be a fundamental contribution of great value to the solution of many scientific and socio-economic problems.

1.2 Why Satellites?

Traditionally, fog detection is based on visibility observations at meteorological stations. These are either performed as subjective assessments by individual observers or as measurements using transmission efficiency (transmissometers) (cf. WMO, 1996, for a detailed description of methods). In the former case remarkable deviations in subjective visibility observations need to be taken into account (Wanner & Kunz, 1983). More importantly though, the most obvious drawback of station-based fog observations is their spatial incoherence (Schulze-Neuhoff, 1976).

An obvious solution to this may be seen in the interpolation of these measurements. However, as Wanner & Kunz (1983) note, fog is not a consistent and continuous phenomenon like air pressure, making interpolation very difficult. Some recent feasibility studies have underlined this point (Hyvärinen, Finnish Meteorological Institute, personal communication 2005; Tzanos, Meteo-France, personal communication 2005).

Numerical models are another possible approach to obtaining spatially coherent information on fog distribution. Both two-dimensional (2D) and three-dimensional (3D) models fulfil the basic requirement of providing spatial information. However, no useful results are obtained during model spin-up phase, which takes about 12 hours; temporal resolution after this stage is poor (Müller, 2005; Masbou & Bott, 2006; Jacobs *et al.*, 2005). While existing models may therefore be well-suited for forecasts, they are not applicable to the time-critical near-real-time assessment of fog cover.

The obvious data source to fill this gap is satellite imagery. In the light of the requirements outlined above, a satellite system is needed with both, good spatial and temporal data resolutions. The latter criterion can only be met by geostationary (GEO) systems. In the past, the spectral potential of GEO

platforms, especially European systems, was very poor however, and only low earth orbiting (LEO) satellite systems had the potential for fog detection. With the advent of the first Meteosat Second Generation (MSG) GEO satellite this situation has improved markedly. The Spinning-Enhanced Visible and Infrared Imager (SEVIRI) aboard this platform provides 12 spectral channels at a 15 minute repeat rate (see chapter 3 for a detailed description of the system). With this new system, fog detection in a timely fashion and with good spatial coverage may be possible for the first time.

1.3 Aim of this Work and Outline

The timely availability of fog distribution information has been mentioned before as a requirement of a fog detection scheme. It is needed in near-real-time (NRT) applications such as fog monitoring and nowcasting. Also, for climatological evaluations, the continual buildup of a product data base with accompanying aggregation is essential. The scheme to be developed therefore has to be fully automated.

The need for automation has two main implications to be considered: a) no subjective preselection of satellite scenes by visual inspection is possible, the scheme must be very stable; b) the computation of the fog product must be accomplished within a 15 minute time frame, following the satellite system's repeat rate.

Based on these considerations, the central theses of this work are:

- It is possible to devise a fog mapping scheme for operational (objective) application, i.e. suitable for automated processing without prior scene selection.
- MSG SEVIRI is suitable for fog detection. Its spectral potential allows for the development of a new technique of this kind.

Accordingly, and addressing the needs and requirements identified, the central aims of the present work are:

- To develop a technique suitable for the objective detection of fog in satellite data, i.e. a *S*atellite-based *O*perational *F*og *O*bservation *S*cheme (*SOFOS*).
- To develop this scheme based on MSG SEVIRI data.

A methodology of this kind will be a valuable contribution in the fields outlined above.

The structure of this work is presented in figure 1.2. After a review of fog processes and previous research, more detailed hypotheses and objectives are introduced with the conceptual design of the newly developed scheme in chapter 2. Satellite data, ancillary data and the operational processing framework are introduced in chapter 3. Chapter 4 is at the core of this work as it contains a detailed description of method development and implementation. Based on a discussion of the theoretical basis it introduces method components in three steps. Literature of direct relevance to the development of an individual method component is presented in the corresponding section. An assessment of the scheme's performance with validation studies is presented in 5, followed by summary and outlook in chapter 6.

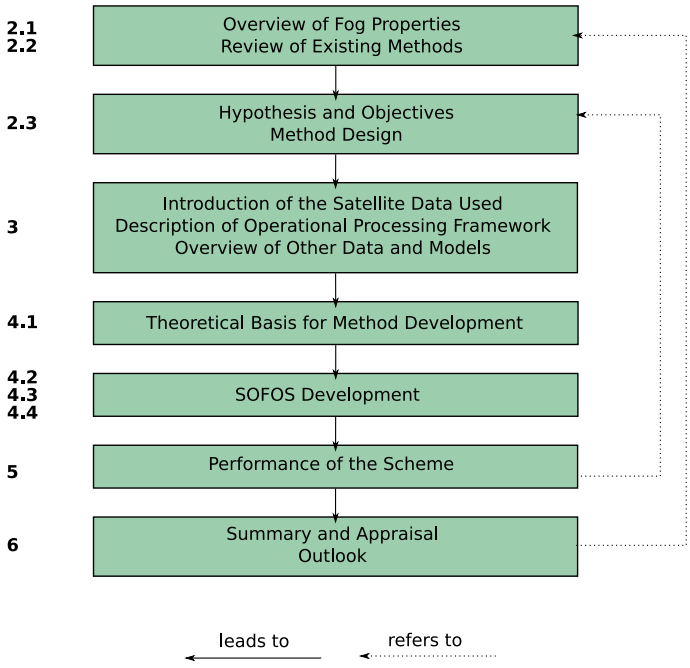

Figure 1.2: *Structure of this work. Bold numbers on the left are chapter and section numbers.*

This research is embedded in the wider framework of the MSG Principal Investigator Research Announcement of Opportunity (RAO) programme conducted by the European Space Agency (ESA) and the European Organisation for the Exploitation of Meteorological Satellites (EUMETSAT). It is integrated into the ESF COST action 722 and a co-operation agreement with the Deutscher Wetterdienst (DWD) SatKlim Climate Monitoring unit. The work also concurs with the main objective of the International Satellite Cloud Climatology Project (ISCCP) to infer cloud properties from satellite

data to enlighten the role of clouds in global climate interactions (Schiffer & Rossow, 1983).

Chapter 2

Conceptual Design

This chapter introduces the design of the new scheme and places it in the context of physical basics and existing techniques. In a first section, the fundamental processes governing fog are discussed as a foundation for satellite-based fog detection. Then, existing schemes are introduced to identify weaknesses and shortcomings to be addressed in the newly developed method.

2.1 Fog Processes and Properties

An appraisal of fog processes and properties is a useful backdrop for the design of a scheme intended to identify this meteorological phenomenon. Concepts and characterisations of the meteorological phenomenon fog vary slightly with the context of the studies in which they are found. There are two main approaches to defining fog:

1. From a technical point of view, any situation with a visibility of 1 km or less is defined as fog. This definition has a long tradition, is very widely cited, and finds its main application in weather analysis at meteorological stations (e.g. Glickman, 2000; Roach, 1994; Taylor, 1917). By this definition, fog is not a cloud but rather a *condition*. This condition may however (and normally does) arise from the 'geographical' situation of a cloud being in touch with the ground (Houze, 1993; Bendix *et al.*, 2005).

2. A second type of definition found in World Meteorological Organization (WMO) manuals addresses fog as a *physical phenomenon*, i.e. a "suspension of very small, usually microscopic water droplets in the air, generally reducing the horizontal visibility at the earth's surface to less than 1 km" (WMO, 1992, 284). Here, reduced visibility is

not the main criterion but rather a consequence of a fog *cloud*. Fog droplets are characterised as having radii between 1 and 40 μm (typically 10 – 20 μm, ROACH, 1994), which fall at velocities of no more than approximately 5 cm s^{-1} (WMO, 1996).

While these definitions appear to be contradictory, they actually only address the same phenomenon from different perspectives. Therefore, for the purpose of the present study both definitions are combined. *Fog* is thus defined as a cloud reducing visibility to 1 km or less at a given location. In this light, *ground fog* is used to address a cloud with local ground contact. Depending on its relative position to the terrain, the same *very low cloud* may manifest itself as ground or *hill fog* in some high locations in touch with the cloud, and as *elevated fog* in others without cloud ground contact. The latter type of situation does not cause visibility impairment directly at the surface, but very close to it, and thus is of great relevance as well, for instance in aviation.

In order to more accurately appraise the properties of fog clouds, and and as a basis for the new method to be developed, the consideration of the dynamics leading to the formation of such as cloud is of use. The basic processes will be presented in the following paragraphs.

The formation of any cloud is a function of the water vapour saturation ratio. The liquid phase becomes more stable than the vapour phase when the observed atmospheric water vapour pressure p' surpasses its saturation value p_s. This situation is called supersaturation. p_s depends on temperature, as given by

$$p_s = p_{s0} \exp\left(\frac{L}{R_v T_0}(1 - T_0/T)\right) \quad [hPa] \tag{2.1}$$

(Clausius-Clapeyron equation, MANTON, 1983), where $T\,[K]$ is the temperature. The other terms are constant, with $R_v\,[J\,kg^{-1}\,K^{-1}]$ the gas constant for water vapour, $L\,[J\,kg^{-1}]$ the latent heat of vapourisation, $T_0 = 273.15\,K$ and $p_{s0} = 6.108\,hPa$.

According to this relationship, cooling reduces p_s and thus favours cloud formation. Ideally, therefore, cloud development would be governed by temperature alone. However, equation 2.1 is valid for level water bodies only. Clouds on the other hand are composed of individual spherical droplets, with a certain degree of surface tension. This property inhibits molecular exchange and thus significantly elevates saturation pressure around spherical liquid bodies, according to

$$p_a = p_s \exp\left(2\sigma / R_v T \rho_l a\right) \quad [hPa] \tag{2.2}$$

(Kelvin equation according to MANTON, 1983), with p_a: saturation vapour pressure for a droplet with radius a $[cm]$, σ $[J\,cm^{-2}]$: surface tension, and ρ_l $[kg\,cm^{-3}]$ the density of liquid water.

Therefore, the smaller a droplet (a), the higher the saturation vapour pressure p_a. If the observed pressure p' is less than p_a, a droplet evaporates. This means that especially small water droplets are prone to evaporation, and cloud formation therefore requires a very large water vapour saturation level.

However, the presence of soluble microscopic particles in the atmosphere significantly reduces the saturation pressure in a process known as heterogeneous condensation. They act as condensation kernels and are known as cloud condensation nuclei (CCN). Raoult's law relates the mole ratio of solvent and solute to vapour pressure over a solution, according to

$$p'/p_s = n_0(n_0 + n_s)^{-1} \tag{2.3}$$

(MANTON, 1983), with p' the vapour pressure over the solution, n_0 and n_s the numbers of solvent (water) and solute (CCN) molecules. At a constant saturation vapour pressure, p' therefore decreases with increasing solute concentration n_s.

The effects of droplet curvature and CCN presence are summarised in Köhler's equation (MANTON, 1983; FLOSSMANN, 1998; BOTT *et al.*, 1990; HENNING *et al.*, 2005). The equilibrium water vapour pressure p_e over a droplet with radius a and an equivalent nucleus (solute) radius a_n is given by

$$p_e = p_s + \left(\frac{a_\sigma}{a} - c_1\frac{a_n}{a}\right) \quad [hPa] \tag{2.4}$$

(KÖHLER, 1936), where $a_\sigma = 2\sigma/R_v T\rho_l$ with ρ_l the density of liquid water, and c_1 proportional to the solute mole fraction.

The Köhler equation shows how surface tension increases and CCN concentration decreases the water vapour pressure over a spherical droplet and both thus directly influence cloud formation processes.

These processes and determinants of cloud formation equally apply to the special case of fog formation, i.e. cloud formation at or near the ground surface. The following paragraphs explore in more detail the circumstances of fog formation and present a typology of fog types.

As shown above, the following preconditions are conducive to fog formation:

- Presence of precipitable water (water vapour).

- Presence of cloud condensation nuclei (CCN).
- Cooling of the air.

CCN can be assumed to be ubiquitous. As shown above, their concentration modulates the humidity threshold at which condensation sets in. Regarding the process of cooling of humid air, the heat budget of an atmospheric layer can be expressed as

$$H_T = H_R + H_E + H_L + H_A \quad [K\,s^{-1}] \tag{2.5}$$

(Roach *et al.*, 1976), with H_T the locally observed rate of temperature change, H_R temperature change due to radiative flux divergence, H_E sensible heat eddy fluxes, H_L latent heat fluxes, and H_A advection of sensible heat.

Cooling of humid air most frequently occurs either by local radiative cooling (H_R) or by mixing of air masses as a result of humidity or heat advection (H_A). Based on these processes the following main types of fog are commonly identified:

Radiation Fog. The development of radiation fog is driven by radiative cooling of a moist atmospheric layer near the surface. Once the ground has cooled sufficiently by unobstructed longwave radiation through a clear atmosphere, the air near the ground loses heat by radiative flux divergence (H_R). Light winds lead to a further loss of sensible heat from the air to the ground. As the air continues cooling, an inversion develops, which blocks further winds and deposition of developing drops as dew. With droplet formation, the surface of the fog layer becomes the radiative surface and cools and thickens further, also facilitated by its high albedo (Houze, 1993; Oke, 1987; Roach, 1995, 1994; Brown & Roach, 2004).

Advection Fog. When warm humid air moves over a cool surface the dewpoint is reached and condensation sets in. A subsidence inversion develops and the fog layer builds downwards from the inversion base. In a similar way 'steam fog' or 'warm water advection fog' develops when cold air is advected over a much warmer water surface (e.g. ice-free lakes in winter) (Wanner, 1979; Oke, 1987; Roach, 1995; Matveev, 1984).

Frontal Fog. When air masses mix, frequently in warm fronts, condensation and stratus formation may set in. Where this stratus touches the ground, a ground fog situation can be identified (Wanner, 1979).

The presence of a temperature inversion at the fog top is the most prominent feature shared by the different fog types. It constitutes the interface between the cloud and the air masses above it. In addition to the cases introduced here, fog can also occur in the form of ice fog, with hydrometeors in the ice phase instead of water. This form is only common at high latitudes. By definition, warm fog has temperatures above 0 °C, super-cooled fog droplets are between 0 and -30 °C cold, and ice fog particles are colder than -30 °C (Wanner, 1979; Oke, 1987). In this study, only warm fog as the by far most common form will be considered.

In summary, fog dynamics as presented above suggest that for the purpose of this study, fog can be addressed as a very low cloud made up of small water droplets trapped under an inversion and thus with a homogeneous, stratiform surface. Ground fog occurs where this cloud touches the surface. These insights will be used as a basis for the present study.

2.2 Approaches to Fog Detection

In the following paragraphs, an overview of existing satellite-based fog detection schemes is presented. Both, daytime and night algorithms are considered, their strengths and weaknesses highlighted. It must be noted that in all of the schemes cited in this chapter, no distinction is made between ground fog, elevated fog and other low clouds. Also, while most of the approaches are designed specifically for fog detection, others include a fog, low stratus or low cloud class in the context of a wider cloud classification scheme.

Fog identification is implemented either as a qualitative decision of an informed observer, or quantitatively tied to statistical analysis or application of a threshold value in hard classifications. In the latter case, thresholds are determined in a number of ways: empirically, by histogram interpretation or based on theory and radiative transfer modelling. The satellite data values are then compared to the threshold to reach a decision on class membership:

$$v(a) \geq v_t(C) \rightarrow a \in C \tag{2.6}$$

with $v(a)$ the data value at pixel a and $v_t(C)$ the threshold value for class C.

Algorithms proposed for fog identification and more widely, cloud classification based on satellite data are manifold. A progression towards more sophisticated and computationally intensive approaches can be observed over time and with improving spectral potential of the satellite sensors available.

The algorithms very roughly fall into two categories:

1. Those designed for application on individual, pre-selected scenes. In most of these cases, the automated separation of fog areas from other clouds is not essential, because fog is predominant. Fog detection therefore focuses on the rejection of clear areas. There are numerous such methods, all of which deal with daytime fog detection.

2. Other schemes are suitable for automated, operational (i.e. objective) processing. These need to reliably separate fog not only from clear areas, but also from other cloud types. This type of scheme is available for nighttime fog detection only.

Algorithms belonging to the former category are numerous and reach various degrees of complexity. The following paragraphs present an overview of the non-operational fog detection techniques. These methods almost exclusively use a channel in the visible range of the electromagnetic spectrum and therefore focus on daytime fog detection.

The simplest schemes make use of only one spectral band. Wanner & Kunz (1983) thus identify fog by visual inspection of National Oceanic and Atmospheric Administration (NOAA) Advanced Very High Resolution Radiometer (AVHRR) images. A similar qualitative approach is taken by Greenwald & Christopher (2000) using Geostationary Operational Environmental Satellite (GOES) data. Ahn *et al.* (2003) compare a clear-sky radiance composite map with Geostationary Meteorological Satellite (GMS) infrared images and radiance ranges expected for fog based on radiative transfer calculations.

As the identification of surfaces at only one wavelength is prone to include unwanted features, such as other clouds with similar spectral properties or snow, textural image information has been included by some authors as a further source of information. In this way, Güls & Bendix (1996) not only apply minimum and maximum reflectance thresholds to the Meteosat visible channel, but complement it with a test for spatial variance. Similarly, Karlsson (1989) uses the texture of a 5 by 5 pixel infrared channel environment to separate cloud types. However, these approaches are still very limited by their use of only one spectral band offering limited distinction between surfaces.

More commonly, a combination of two or more spectral channels is used in a multispectral classification. Many techniques are based on a combination of a channel in the visible range and one in the infrared (around 11 μm). Two-dimensional histogram analysis is performed on the basis of Meteosat

and NOAA AVHRR data by several authors (Billing *et al.*, 1980; Simmer *et al.*, 1982; Liljas, 1981; Porcu & Levizzani, 1992). More advanced techniques of pattern recognition were introduced at a later stage; Kietzig (1991) uses spectral similarities of neighbouring pixels to enhance the classification scheme, Pankiewicz (1995) and Pankiewicz (1997) apply a neural network approach to Meteosat visible and infrared data.

However, not only do these tests perform poorly at the separation of cloud and snow areas due to similar spectral behaviour of both surfaces; they also do not attain a proper discrimination between low stratus and other cloud types, even after the inclusion of a near-infrared channel (1.6 μm) (Liljas, 1982; Dyras, 2000), so that only manually selected scenes can be processed. The same applies to an algorithm presented by Bendix & Bachmann (1991) and Bendix (1995). In their approach, the middle infrared (MIR) signal (around 4 μm) is subtracted from the infrared (IR) signal. Since only the former contains a reflective component and clouds have a larger reflection than clear areas, the radiance difference is smaller for clouds. However, although the separation of fog from clear ground works well in this way, the distinction from other cloud types remains an unsolved problem at daytime.

The only algorithm truly suitable for operational fog detection is a nighttime-only method and was first applied by Eyre *et al.* (1984). The authors take the difference in radiances at 10.8 and 3.7 μm (MIR) at night as an indication for fog presence. In essence, this technique identifies clouds with predominantly small droplets. It is based on differences in emissivity between infrared and middle infrared wavelengths as a function of cloud droplet size as presented by Hunt (1973). This relationship is shown in figure 2.1 for clouds of various optical depths (a measure of cloud thickness, cf. section 4.1.2). It can be seen that emissivity differences between both wavelengths are much larger for small droplets (effective radius = 4 μm in the example) than for larger droplets (effective radius = 10 μm). This principle is used to identify small-droplet clouds in satellite imagery. While the original scheme produced colour composites for interpretation by a forecaster, a threshold value was soon introduced to obtain a classification. The method has since been widely used by numerous authors and on a wide range of platforms (Turner *et al.*, 1986; Allam, 1987; D'Entremont & Thomason, 1987; Bendix & Bachmann, 1991; Derrien *et al.*, 1993; Bendix, 1995; Ellrod, 1995; Lee *et al.*, 1997; Reudenbach & Bendix, 1998; Putsay *et al.*, 2001; Bendix, 2002; Underwood *et al.*, 2004). This method has been shown to provide accurate detection of small-droplet clouds in the studies cited, with clear separations of low stratus from cloud-free regions, snow and

other clouds. The scheme has also successfully been ported to MSG SEVIRI (Cermak *et al.*, 2004).

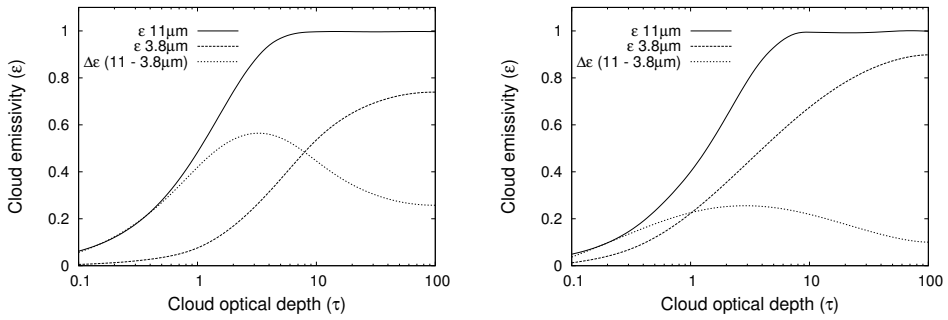

Figure 2.1: *Emissivities as a function of droplet size and wavelength vs. cloud optical depth, after* Hunt *(1973).* ϵ *is the emissivity at wavelength* λ*,* $\Delta\epsilon$ *the difference in emissivities. The panel on the left hand side shows the emissive behaviour for an effective droplet radius of 4* μm*, the right hand side for 10* μm*.*

However, due to its use of a channel in the MIR region, the algorithm can only be applied at night. At daytime, solar radiation mixes into the signal at 3.7 μm (cf. figure 2.3, upper part). Cloud emissivity and droplet size can therefore no longer be inferred. The obvious solution for applying this method at daytime would be a correction of the MIR signal, i.e. the attempt to remove the solar component of the signal. Assuming similar emissivities in the middle (MIR) and thermal IR, the thermal component of the MIR signal is commonly computed by substituting the IR brightness temperature into the Planck function (cf. chapter 3):

$$L^t_{\mathrm{MIR}} = \frac{2hc^2}{\lambda^5_{c,\mathrm{MIR}} e^{hc/\lambda_c k T_{\mathrm{IR}}} - 1} \quad [W\,m^{-2}\,\mu m^{-1}] \tag{2.7}$$

with L^t_{MIR} the thermal part of MIR spectral irradiance, $h\,[J\,s]$ the Planck constant, $c\,[m\,s^{-1}]$ the speed of light, $\lambda_{c,MIR}\,[\mu m]$ the effective central wavelength of the MIR channel, $k\,[J\,K^{-1}]$ the Boltzmann constant, and $T_{\mathrm{IR}}\,[K]$ the thermal IR blackbody temperature. However, this approach is impractical for small droplet clouds as here the assumption of similar emissivities at both wavelengths is invalid (Hunt, 1973, cf. figure 2.1, left hand panel). Therefore, the solar component of the signal cannot be removed and this approach not be applied for daytime fog detection.

In summary, while advances have been made in satellite-based fog detection with improving sensors, a solid scheme for small-droplet cloud detection is only available for nighttime data so far. The daytime techniques in ex-

istence do not accomplish a satisfactory discrimination between fog, other clouds and snow, and can thus not be used in operational fog detection. A stable scheme applicable at daytime is still alack and will have to be an entirely new development.

Further to not presenting a feasible solution to daytime fog detection, the approaches introduced above do not distinguish between low-level clouds with and without ground contact. Therefore, a separation between elevated fog and ground fog is not possible. While the schemes presented are two-dimensional (2D) only, information on cloud geometry would be needed in order to distinguish between low clouds and ground fog.

2.3 SOFOS Design

The theses stated in chapter 1 were that a) an operational fog mapping scheme can be developed on the basis of satellite data and b) MSG SEVIRI has the spectral potential for this. The review presented above shows that existing satellite-based fog detection schemes fail in two central areas:

- No operationally applicable scheme is available for daytime fog detection. The schemes that do exist fail to separate fog from other clouds and thus can only be applied to pre-selected scenes.
- No distinction is offered between elevated fog and ground fog. None of the existing schemes, including night and daytime approaches, separate ground fog from other low clouds.

These shortcoming have very much limited the usability of satellite-based fog detection up to now. To overcome them, the following hypotheses are put forth based on the review of fog processes and properties presented above:

1. The delineation of very low stratus from other surfaces can be performed by explicitly addressing its main physical and spatial properties as identified above: Fog can be addressed as a very low stratiform water cloud with small droplets limited by an inversion and thus a fairly homogeneous top.

   The problem of surface separation is visualised in figure 2.2. Cloudy surfaces need to be discriminated from clear areas, and very low stratus clouds have to be singled out from the former.

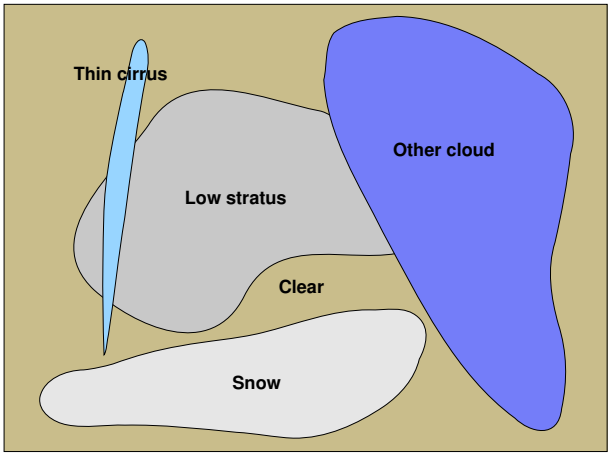

Figure 2.2: *Concept I: Low stratus delineation requires the separation of competing surfaces in the 2-dimensional domain.*

2. A discrimination between ground fog and other very low stratus clouds can be achieved based on cloud geometry information. This is based on the assumption that ground fog can be addressed as a cloud with ground contact. A decision on ground contact can be reached by comparing surface elevation z_s and cloud base height z_b, given by

$$z_b = z_t - \Delta_z \quad [m] \tag{2.8}$$

   with z_t $[m]$ cloud top height and Δ_z $[m]$ cloud geometrical thickness. Thus z_t and Δ_z need to be known (cf. figure 2.3).

3. The criteria for very low stratus and ground fog detection stated above are of a sufficient solidity to allow operational application of a newly developed scheme. On this basis, it is possible to automatically single out fog-covered pixels from any unknown satellite data set.

The design of the new scheme needs to follow and incorporate these hypotheses. Thus, the aim of developing a Satellite-Based Operational Fog Observation Scheme (SOFOS, see chapter 1) is complemented with the following scientific objectives:

- Develop a technique for the delineation of very low stratus areas in satellite imagery at daytime.
- Develop a technique for the determination of very low stratus geometry and thus cloud ground contact.

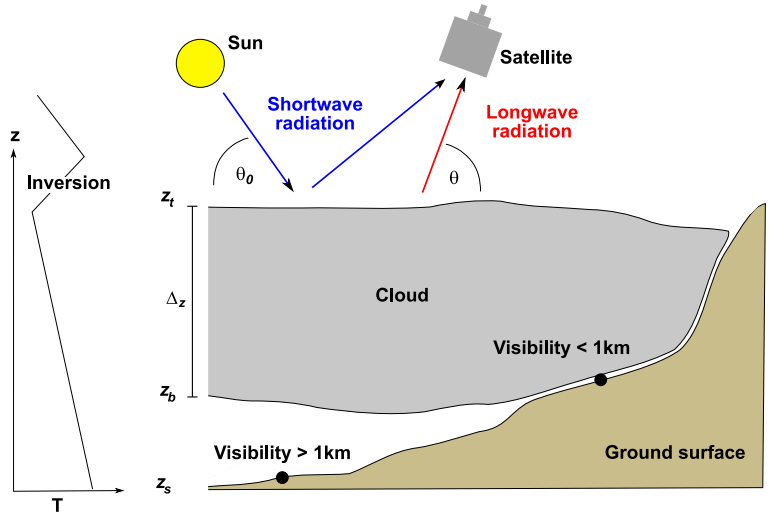

Figure 2.3: *Concept II: Ground fog detection requires knowledge of cloud geometry, i.e. 3-dimensional information on the cloud, including its boundaries (z_t and z_b) and thickness (Δ_z), and surface elevation z_s. These properties manifest themselves in the shortwave and longwave radiation transferred from the cloud to the satellite sensor (see chapter 4).*

A third, technical objective is to develop an operational framework for the near-real-time processing of SEVIRI data and product generation. While this is not part of the scientific scope of this work, it forms an integral part and indispensable precondition for the success of the new scheme.

The development of the Satellite-based Operational Fog Observation Scheme (SOFOS) is governed by these objectives. An overview of the scheme's design is presented in figure 2.4. This figure shows the components of the scheme and their embedding into the operational framework. The latter handles preprocessing of satellite data and provides an environment for fog product generation.

As a study region, an area comprising large parts of Western and Central Europe was chosen (see figure 2.5). This region is ideally suited for this study for the following reasons:

- Different types of fog can be found in this region, so that a scheme developed here will be transferable to other areas.
- The spatial domain is sufficiently large to ensure the scheme is of supra-local validity.

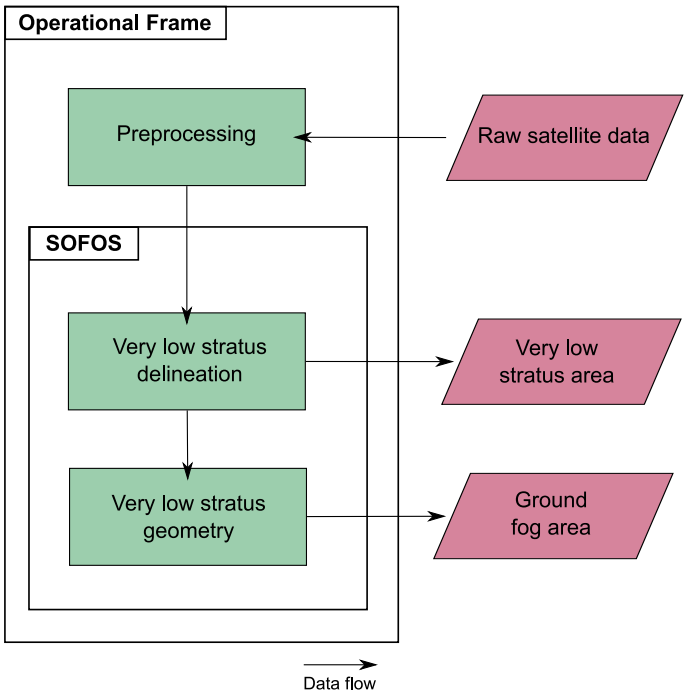

Figure 2.4: *Overview of SOFOS. The major steps, Very low stratus delineation and very low stratus geometry retrieval are embedded in an operational context. SOFOS components are introduced in detail in chapter 4, the operational frame is presented in chapter 3.*

- The availability of both satellite and validation data is comparatively good (see chapter 3).
- Most member countries of COST action 722 (cf. chapter 1) are covered, so the new method can be fully integrated into this domain.

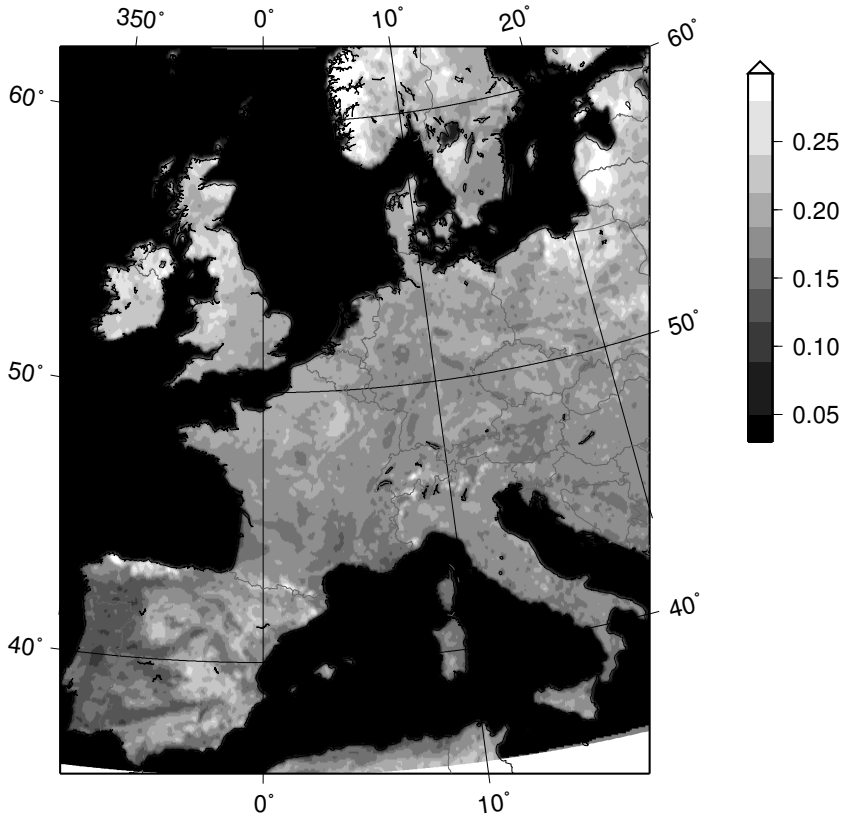

Figure 2.5: *Approximate study area, presented as a clear sky broadband surface reflection map (cf. chapter 3) for a summer day. This map, as most other satellite maps in this work, is presented in a Lambert conic projection, with the origin at 0°, and standard parallels at 40 and 60° N.*

The entire scheme was developed in Fortran 90 and runs on a standard Linux PC. Its modular structure allows for the effortless inclusion of additional components or satellite systems in the future. For near-real-time processing, the scheme provides for the distribution of processes on several machines. In the presented form, two standard PCs easily manage the workload involved.

Chapter 3

Data, Models and Operational Framework

This chapter provides an overview of all the data and models used in the present study. First, the MSG SEVIRI satellite system is introduced. In the second section, ancillary data and models used in this study are presented. The third section describes the newly developed operational framework together with the techniques used for satellite data processing (such as calibration and regional sub-setting). Finally, some enhanced and adapted preliminary satellite products used as preconditions for the new method are presented in the last section.

3.1 Satellite Data – The MSG SEVIRI System

With increasing user demands and improving technical possibilities, the Meteosat Second Generation (MSG) series of meteorological satellites was designed in the last decade of the 20^{th} century. After a commissioning phase of about one year, the first of a planned three MSG systems, MSG 1, became operational in early 2004. It has since then been known as 'Meteosat 8'. The identical MSG 2 satellite is now in standby orbit and will replace the current system as Meteosat 9. MSG 3, the last in the series, is planned to remain in operation until about 2015, so that continuity is provided for (Munro *et al.*, 2002; Schmetz *et al.*, 2002; Schumann *et al.*, 2002).

The MSG satellites carry two sensors: the Global Earth Radiation Budget (GERB) instrument and the Spinning-Enhanced Visible and Infrared Imager (SEVIRI). GERB, as its name reveals, is intended to study the earth's radiation budget, and is equipped with one shortwave and one longwave band (Mueller *et al.*, 1999; Sandford *et al.*, 2003; Harries &

Crommelynck, 1999).

SEVIRI on the other hand is designed for the continuous monitoring of the earth-atmosphere system. At a repeat rate of 15 minutes data is collected in 12 spectral bands (see table 3.1). The satellite is centred at 3.4 ° W; one scan cycle covers the hemisphere seen from this point (see figure 3.1).

Band No.	λ_c	λ_{min}	λ_{max}	Main Absorber/Window
1	0.64	0.56	0.71	Window
2	0.81	0.74	0.88	Window
3	1.64	1.50	1.78	Window
4	3.90	3.48	4.36	Window
5	6.25	5.35	7.15	Water vapour
6	7.35	6.85	7.85	Water vapour
7	8.70	8.30	9.10	Window
8	9.66	9.38	9.94	Ozone
9	10.80	9.80	11.80	Window
10	12.00	11.00	13.00	Window
11	13.40	12.40	14.40	CO_2
12	(Broadband)	~ 0.4	~ 1.1	Window, water vapour

Table 3.1: *SEVIRI channels, (*Schmetz et al.*, 2002, modified). λ_c: central wavelength, λ_{min} and λ_{max}: lower and upper wavelength limits (all in μm).*

Channel 12, the High Resolution Visible (HRV) channel, has a spatial resolution of 1.67 km. With an oversampling factor of 1.67 this yields a sampling distance of 1 km at sub-satellite point. The other channels feature spatial resolutions of 4.8 km, yielding a 3 km sampling distance at nadir with an oversampling factor of 1.6 (Aminou *et al.*, 1999; Aminou, 2002; Pili, 2000; Schmetz *et al.*, 2002).

3.2 Ancillary Data and Models

The development and validation of the new method required the use of some data and models in addition to the satellite data described above. These are briefly introduced in this section.

3.2.1 Synoptical Data

For validation of the scheme, METeorological Aerodrome Report (METAR) data was used. By international convention, large and medium size airports

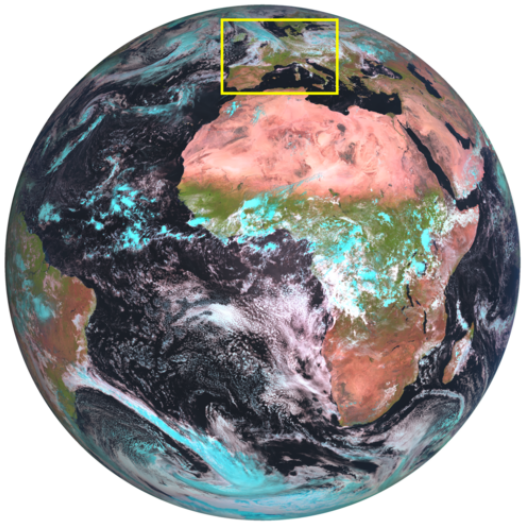

Figure 3.1: *SEVIRI spatial coverage, presented as a false-colour composite image (1.6 µm: red, 0.8 µm: green, 0.6 µm: blue). Image taken on 30 September 2004 at 1100 UTC. The approximate study area (cf. figure 2.5) is indicated in yellow.*

around the world publish reports in this format at least hourly. The full convention is outlined in WMO (1995). Although the contents of a METAR vary, most commonly the following parameters are reported:

- Temperature at 2 m above ground
- Dew point temperature
- Wind speed
- Wind direction
- Precipitation type
- Cloud cover
- Cloud base height (ceiling)
- Visibility
- Barometric pressure

The two parameters used in this study are visibility and cloud ceiling height (chapter 5). These parameters are retrieved either automatically or estimated by human observers at each station. Light detection and ranging

(Lidar) ceilometers are commonly used for automated cloud base height retrieval. These instruments emit a laser beam and measure the reflection by the cloud base. Visibility ("meteorological optical range") is often obtained using transmissometers. The transmission of light through a volume of air is measured between a transmitter and a receiver component of the instrument (WMO, 1996).

The reasons for using METAR data rather than other synoptic data are explained in context in chapter 5. Figure 3.2 shows the sites producing METARs within the study region.

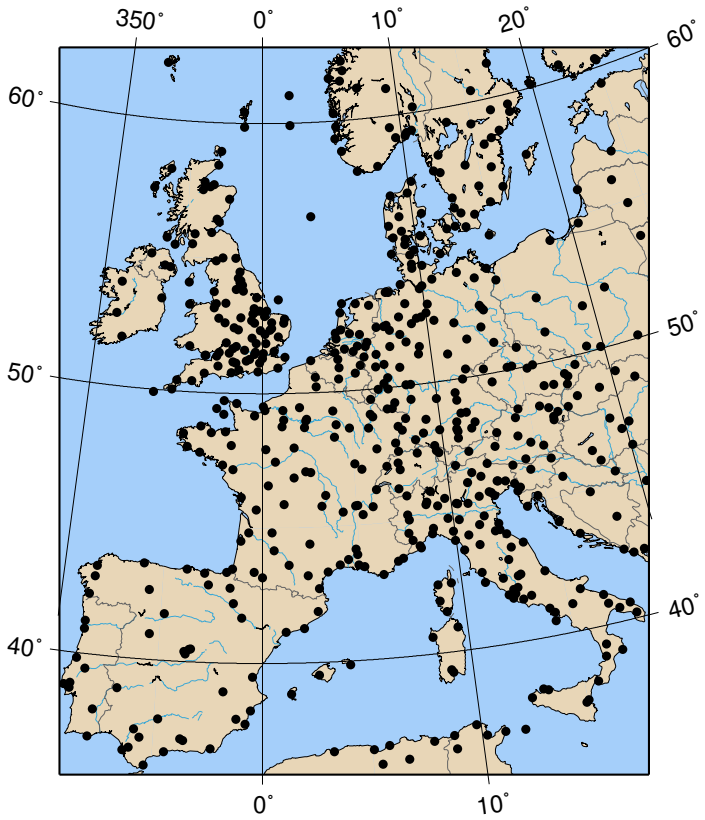

Figure 3.2: *Sites of airports with METAR within the study region (dots). Location data according to United States National Center for Atmospheric Research (NCAR).*

3.2.2 Digital Elevation Model

A digital elevation model (DEM) is a digital representation of surface height on a raster grid. The GTOPO30 DEM provided by the United States Geo-

logical Survey (USGS, 1993) was re-sampled to MSG viewing geometry. A bilinear interpolation was performed. With an original sampling distance of 30 arc seconds, roughly corresponding to 1 km, the resolution of the DEM is sufficient for use with SEVIRI data. Re-sampling was done for both, the HRV channel and the 3 km channels. Also, a binary land-sea mask was extracted from this data.

3.2.3 Radiative Transfer Model

A radiative transfer model is used with the main purpose to simulate radiances received at the satellite sensor for a variety of atmospheric situations (cf. chapter 4). A range of well-tested radiative transfer models are available for this type of application, among these 6s (Vermote *et al.*, 1997), LOWTRAN (Low resolution transmittance code, Kneizys *et al.*, 1988), MODTRAN (Moderate resolution transmittance code, Snell *et al.*, 1995), RTTOV (Radiative Transfer for TOVS, Saunders *et al.*, 2002) and Streamer (Key & Schweiger, 1998). Out of these, Streamer was chosen because it is the only model meeting all of the following requirements:

- Provision for both, longwave and shortwave computations
- Detailed parameterisation of cloud situations
- Inclusion of sensor-specific response functions
- Direct computation of radiances, reflectances and blackbody temperatures
- Flexible choice of atmospheric profiles to be used

Radiance computations in Streamer use the discrete ordinate solver, DISORT (Discrete ordinates radiative transfer, Stamnes *et al.*, 1988), water cloud parameterisation follows Hu & Stamnes (1993), ice clouds are implemented after Fu & Liou (1993). As the SEVIRI channels have a comparatively large spectral width, they can easily be represented using the spectral bands implemented in Streamer (based on Slingo & Schrecker, 1982).

3.3 FMet: An Operational Framework Including Data Processing

The automated handling of satellite and ancillary data requires an operational framework. This section introduces the programs developed to provide this and details the procedures involved.

MSG SEVIRI data has been received at the Marburg Satellite Station (MSS) since 2003, when MSG 1 was still in the commissioning phase (Reudenbach *et al.*, 2004; Bendix *et al.*, 2003). The raw data provided is referred to as level 1.5 data (EUMETSAT, 2005b). Since this data does not have a geophysical meaning it cannot be used directly in product generation.

The Framework for Meteosat data processing (FMet) toolbox has been newly developed specifically for this study to provide both, a framework for the processing of SEVIRI data and a logistic wrapper for operational product generation. An overview of this scheme with its modules is given in figure 3.3. Within FMet, level 1.5 data is transformed into elementary geophysical (level 2.0) and higher level (3.0) products.

FMet is fully configurable. Options include: the satellite channels to be processed; the calibration level desired for each channel; products required; free configuration of all relevant parameters and settings for each routine. The program can be run in online (i.e. operational processing) and offline (i.e. reprocessing of saved data) modes. The FMet modules shown in figure 3.3, MetGet, MetGeo, MetCal, MetProd and MetOut, are described in detail in the following. Some of these modules combine several small program utilities, each of which adds to the task of the module. These utilities are given in italics and also shown in the overview figure.

3.3.1 MetGet: Raw Data Handling and Import

In a first module, MetGet, raw data conversion, import and regional subsetting is performed. Level 1.5 data is thus made accessible for higher level product generation. The High Rate Information Transmission (HRIT) raw data stream received contains wavelet encrypted, compressed and segmented imagery. In a first step, the individual channels of a scene therefore need to be decrypted, decompressed and concatenated (EUMETSAT, 2001, 2003).

Decryption is performed by the EUMETSAT Broadcast system for Environmental Data (EUMETCast) Client Software (EUMETSAT, 2004), with a hardware device, the EUMETCast Key Unit (EKU). Wavelet decompression requires a software package available under license from EUMETSAT. This software is incorporated in the *xrit2pic* package (Alblas, 2006), which also handles image concatenation. MetGet controls the operation of *xrit2pic* and captures its output for further use. The image concatenated by *xrit2pic* is then converted from pgm (pixel grey map) to a flat binary format with geometry information in separate text files by the *pgm2rst* utility. The EUMETCast software and *xrit2pic* are the only external components used in the entire FMet scheme. All other utilities were newly developed for the

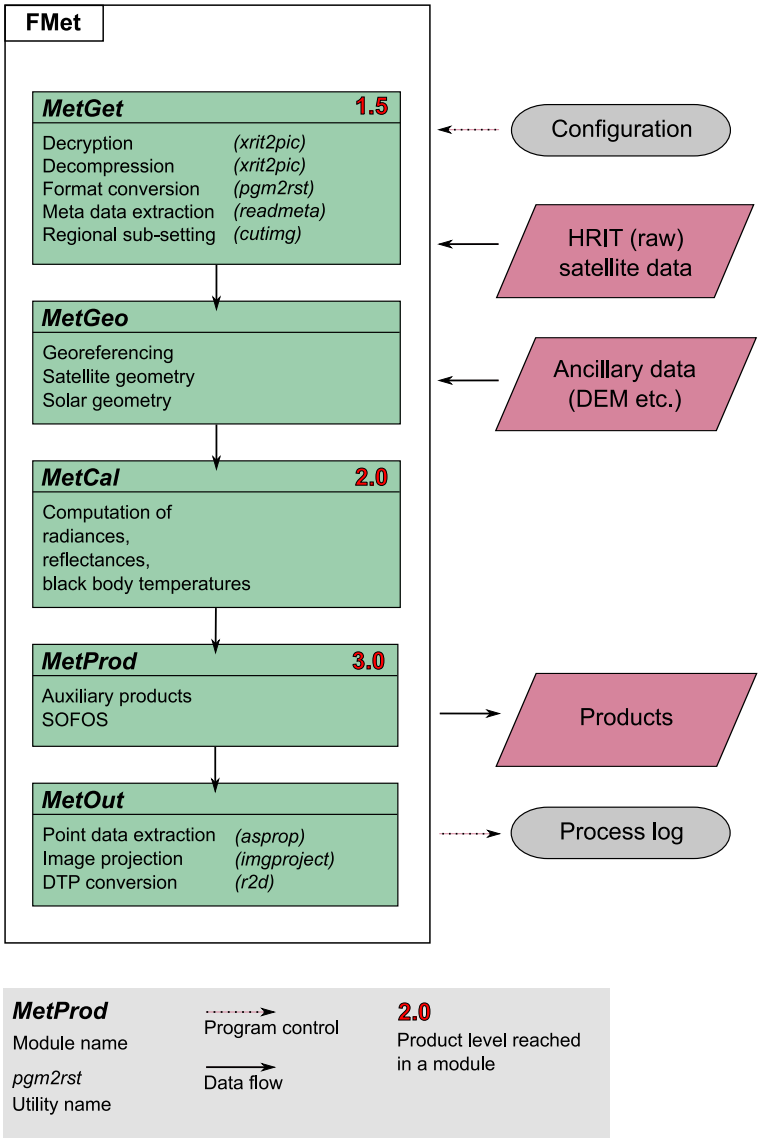

Figure 3.3: *Overview of the FMet scheme. Explanations see text.*

present study.

After the image data has been made available in this way, the *readmeta* utility extracts ancillary information from the original HRIT file headers (cf. CGMS, 1999; EUMETSAT, 2003, 2005a,b). This meta data includes information on channel radiometric calibration, geolocation and scene timing, among others. These descriptors are saved for later use.

Finally, based on user-defined settings, a region of interest is cut by *cutimg* from all channels and also from any ancillary data files provided (including a digital elevation model, see above). This region is set in the main FMet configuration file.

3.3.2 MetGeo: Geolocation and Geometry

SEVIRI images are available in a normalised geostationary projection according to CGMS (1999). This projection is defined in relation to the sub-satellite (nadir) longitude ϕ_n (3.4°W in the case of MSG). The view point (satellite) is assumed to be located perfectly above the equator and exactly at ϕ_n. The distance between viewer and earth centre is assumed to be 42164 km, the earth is approximated as an oblate rotational ellipsoid with a polar radius of 6356.5838 km and an equatorial radius of 6378.1690 km (CGMS, 1999).

A Cartesian frame (s_1, s_2, s_3) is introduced with its origin at the satellite position. s_1 points to the centre of the earth, s_3 is directed northwards. In this system, geostationary coordinates (c, r) are translated to intermediate coordinates (x, y) using offset and scaling factors provided in the HRIT data header record. The intermediate coordinates can be translated to longitude (ϕ_e) and latitude (λ_e) as follows:

$$\phi_e = \arctan\left(\frac{s_2}{s_1}\right) + \phi_n \tag{3.1}$$

$$\lambda_e = \arctan\left(\frac{1.006803 s_3}{s_{xy}}\right) \tag{3.2}$$

with ϕ_e the terrestrial longitude at location x, y and $s_{xy} = \sqrt{s_1^2 + s_2^2}$ (CGMS, 1999).

The geolocation accuracy for SEVIRI is better than 3 km at nadir and better than 0.75 km within a 16 by 16 pixel environment. The relative image-to-image collocation accuracy displays a root mean square error (RMSE) of 1.2 km (Schmetz *et al.*, 2002).

For each image coordinate (x, y), ϕ_e and λ_e are computed in this way and saved in corresponding data sets for use by succeeding programs. Likewise, satellite and solar geometry, i.e. zenith and azimuth angles are calculated.

3.3.3 MetCal: Image Calibration

Image calibration converts level 1.5 raw image counts to geophysically meaningful parameters (level 2.0 products). These are spectral radiance, black body temperature (thermal channels) and reflectance (solar channels).

For each channel i the conversion of raw image counts C_i to spectral radiance I_i is performed by

$$I_i = C_i s_i + o_i \quad [W\, m^{-2}\, sr^{-1}\, cm] \tag{3.3}$$

with scaling (s_i) and offset (o_i) factors derived from on-board blackbody calibration.

For the thermal channels, equivalent blackbody temperatures (T_i) are computed using an analytic relationship with observed radiances based on the inverted Planck function:

$$T_i = \left[C_2 \nu_{ci} / \ln\left(\frac{C_1 \nu_{ci}^3}{I_i} + 1 \right) - B_i \right] / A_i \quad [K] \tag{3.4}$$

with the radiation constants $C_1 = 2\pi hc^2$ and $C_2 = (hc)/k$, where $c\,[m\,s^{-1}]$: speed of light, $h\,[Js]$: Planck constant, and $k\,[J\,K^{-1}]$: Boltzmann constant. $\nu_{ci}\,[cm^{-1}]$ is the central wavenumber for channel i, A_i and $B_i\,[K]$ are constants derived in non-linear regression for each channel.

For the shortwave channels, reflectance r_i is computed as follows:

$$r_i = \frac{I_i}{E_i \cos(\theta_0)} \tag{3.5}$$

with θ_0 the solar zenith angle and $E_i\,[W\, m^{-2}\, cm]$ the spectrally integrated extraterrestrial irradiance for channel i. The latter was derived by polynomial interpolation of extraterrestrial solar spectral radiance data (presented in Wehrli, 1985, 1986).

3.3.4 MetProd: Operational Product Generation

Based on the level 2.0 products produced by MetGeo and MetCal, higher level (3.0) product generation is implemented in FMet. The central product naturally is the fog classification, computed by the SOFOS algorithms.

The fog detection routines are preceded by a set of supplementary algorithms that produce input required by the fog detection scheme. These

include various albedo and temperature products as well as precipitable water column. Full descriptions of the auxiliary satellite products are given in section 3.4.

The integration into FMet of all products and product components is handled dynamically; the choice of products to be computed for each scene is implemented as a freely configurable parameter. Also, additional products can be added at any time.

3.3.5 MetOut: Output Formatting

In the MetOut module products of any processing stage can optionally be passed to post-processing, e.g. for presentation. Options are:

- The *asprop* utility extracts product information for individual pixels, e.g. for inter-comparison with point data or for localised time series generation.
- For conversion of output images to common desktop publishing formats *r2d* was developed. This program supports a range of colour palettes, annotations and legend formats. Selected products are routinely converted for later use.
- With *imgproject*, the images can be transformed from the geostationary to other projections. This step is performed only after processing, because of the information loss (pixel redundancy and gaps) incurred in re-sampling.

3.4 Auxiliary Satellite Products

A number of auxiliary products are needed by some of the algorithms presented in chapter 4. Their computation is performed within the MetProd module of FMet (cf. above and figure 3.3). The procedures and considerations involved in the derivation of these partly adapted and partly enhanced products are considered in the following.

Broadband albedo. Planetary albedo is the ratio of flux density reflected to space ($F\uparrow\ [W\,m^{-2}]$) to incident solar flux density ($F_\odot\,[W\,m^{-2}]$) at a given solar zenith angle θ_0 ($\mu_0 = \cos(\theta_0)$):

$$A(\mu_0) = \frac{F\uparrow}{\mu_0 F_\odot} \tag{3.6}$$

The reflectance values computed for the individual SEVIRI channels only represent the reflectance in a particular wavelength interval (satellite band). From these narrow bands, the planetary albedo, or broadband albedo, needs to be computed. A multitude of methods for the conversion of shortwave channel reflectances to broadband albedo have been proposed for various satellite instruments (for an extensive compilation and review cf. LIANG, 2001). Most of these are either based on regression or on radiative transfer modelling.

For MSG SEVIRI, CLERBAUX *et al.* (2006) present a parameterisation derived from systematic comparisons with data from the Clouds and the Earth's Radiant Energy System (CERES) instrument. Their approach includes reflectance information from all SEVIRI shortwave channels, the solar zenith angle and the sun glint angle, as

$$A_{sw} = c_0 + c_1 a_{0.6} + c_2 a_{0.6}^2 + c_3 a_{0.8} + c_4 a_{1.6} + c_5 \theta_0 + c_6(-\psi) \quad (3.7)$$

(CLERBAUX *et al.*, 2006), where c_1 to c_6 are the regression parameters, θ_0 is the solar zenith angle and $-\psi$ the sun glint angle, with ψ the scattering angle.

The parameters are presented for five difference surfaces ('bright vegetation', 'dark vegetation', 'bright desert', 'dark desert', 'ocean'). Europe is almost entirely covered by 'bright vegetation' by their classification so that this parameterisation was uniformly implemented for broadband albedo retrieval. CLERBAUX *et al.* (2006) give a root mean square error of 4.64% for this class.

Clear sky reflectance. The clear sky reflectance product is a composite of the most recent surface reflectance values available for each picture element and channel (cf. equation 3.5). While each scene is processed, the reflectance values of all pixels flagged as clear (full description of cloud detection method in chapter 4) are transferred to the clear sky reflectance map, replacing older values stored in the product. In this way a continually updated clear sky reflectance can be made available to other routines (see chapter 4). The computation is performed for all shortwave channels and broadband albedo. A sample product for a summer scene is presented in figure 2.5.

Precipitable Water Content. A number of approaches have been proposed for the quantification of the precipitable water vapour column U. This parameter expresses the mass of atmospheric water vapour

per area above the earth surface and is needed for surface skin temperature computation (see below). It is defined as

$$U = \int_0^H \rho_a q dz \quad [g\,cm^{-2}] \tag{3.8}$$

(MATVEEV, 1984), with ρ_a $[g\,m^{-3}]$ air density and q [%] air humidity in the sub-interval dz $[m]$. H is the total height of the column.

Most published approaches for precipitable water vapour retrieval make use of the so-called 'split-window' channels at 11 and 12 μm. The difference in radiances between both channels is a function of atmospheric absorption and, to a lesser degree, differences in surface emissivity. The latter is commonly neglected and emittance assumed to be near unity. The former is of major importance, with the water vapour extinction cross section about twice as great at 12 μm (CHESTERS *et al.*, 1983).

A range of algorithms have been proposed for application on various systems. The majority are parameterisations based on radiative transfer calculations for specific instruments.

CHOUDHURY *et al.* (1995) propose

$$U = \frac{T_{10.8} - T_{12.0} + 0.14}{0.047} \quad [g\,cm^{-2}] \tag{3.9}$$

for AVHRR, with T_λ $[K]$ the blackbody temperature at wavelength $\lambda[\mu m]$. ULIVIERI (1985) use

$$U = \frac{T_{10.8} - T_{12.6}}{T_{10.8} - T_{11.9}} - A/B \quad [g\,cm^{-2}] \tag{3.10}$$

on Visible and Infrared Spin Scan Radiometer Atmospheric Sounder (VAS) data, PRINCE *et al.* (1998) put forth

$$U = 17.32\frac{T_{10.8} - T_{12.0} - 0.6831}{T_s - 291.97} + 0.5456 \quad [g\,cm^{-2}] \tag{3.11}$$

for AVHRR ($T_s[K]$ is surface temperature) and CHESTERS *et al.* (1983, 1987) compute total atmospheric precipitable water as

$$C = D + \cos\theta \ln\left(\frac{T_{12.7} - T_a}{T_{11.2} - T_a}\right) \tag{3.12}$$

$$U = \frac{-B + \sqrt{B^2 - 4AC}}{2A} \quad [g\,cm^{-2}] \tag{3.13}$$

with A, B, C and D absorption parameters specific to this channel combination and T_a $[K]$ the air temperature.

Finally, in an adaptation of the algorithm to the SEVIRI instrument the EUMETSAT Nowcasting Satellite Application Facility (SAFNWC) (INM, 2005) total precipitable water product is computed as

$$U = A + B \ln \left(\frac{T_{10.8} - T_a}{T_{12.0} - T_a} \right) \cos \theta \quad [g\, cm^{-2}] \tag{3.14}$$

Instead of air temperature (T_a), the use of $T_{13.4}$ is suggested. The parameters A and B are only disclosed to the SAFNWC users (i.e. European national meteorological services); an attempt to obtain them from the scientific team was unsuccessful.

Nonetheless, the procedure proposed in equation 3.14 was selected as it presents a specific adaption to the SEVIRI instrument. Parameters A and B were obtained by fine-tuning the equation against the corresponding Moderate Resolution Imaging Spectroradiometer (MODIS) total precipitable water product (Gao & Kaufman, 1997; King *et al.*, 1992), yielding $A = 3$ and $B = 500$. Figure 3.4 shows the distribution of precipitable water computed with the adapted SAFNWC scheme vs. MODIS MOD05 infrared method precipitable water for a scene selected at random (1130 universal time co-ordinated (UTC) on 16 August 2005). In this scene, the products show a positive correlation with r = 0.83 (n = 6554). As satellite-based precipitable water products are a field with great uncertainties (see all of the sources cited above, especially Gao & Kaufman, 1997; INM, 2005), this agreement by tendency can be accepted as an indication of satisfactory performance.

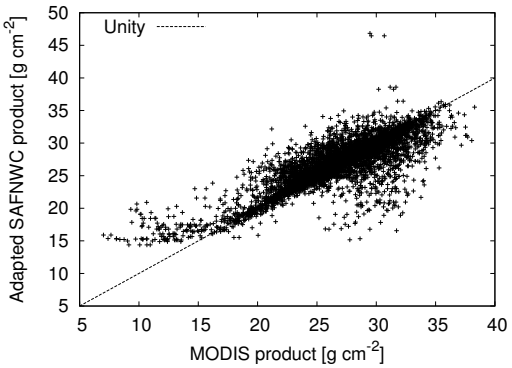

Figure 3.4: *Precipitable water computed with two different methods, 1130 UTC, 16 August 2005.*

Surface Skin Temperature. Blackbody temperatures computed on the

basis of radiances registered at the sensor represent the temperature of an ideal body with an emissivity $\epsilon = 1$ and therefore are invalid for actual matter (with smaller emissivities). Further, absorption and viewing geometry are neglected in the computation of this quantity. In contrast, skin temperature is a satellite-observed parameter meant to represent the upper few centimetres or even millimetres of the surface. It is closely related to the air temperature in this layer (Vogt *et al.*, 1997; Stephens, 1994). This parameter is needed for the algorithms to be introduced in chapter 4.

The computation of the 'true' skin temperature requires consideration of both factors, absorption and emission. A range of methods exist considering only one of them. Price (1984), Prince *et al.* (1998), Hillger & Kidder (2003) and Wan (1999) all estimate water vapour extinction; Kerr *et al.* (1992) introduce an approach to correct for surface emissivity differences. A comprehensive method comparison in presented in Vazquez *et al.* (1997).

Sobrino & Romaguera (2004) find a specific formulation for MSG SEVIRI considering both relevant parameters:

$$\begin{aligned} T_s &= T_{10.8} + (3.17 - 0.64\cos\theta)(T_{10.8} - T_{12.0}) \\ &\quad + \left(-0.05 + \frac{0.157}{\cos\theta}\right)(T_{10.8} - T_{12.0})^2 \\ &\quad + \left(65 - \frac{4}{\cos^2\theta}\right)(1-\epsilon) + \left(-11.8 + \frac{5.1}{\cos\theta}\right)U(1-\epsilon) \\ &\quad + \left(-180 + \frac{24}{\cos\theta}\right)\Delta\epsilon + \left(-4 + \frac{34}{\cos\theta}\right)U\Delta\epsilon \\ &\quad -0.6 \quad [K] \end{aligned} \tag{3.15}$$

with $\epsilon = (\epsilon_{10.8} + \epsilon_{12.0})/2$ the mean surface emissivity at both wavelengths considered and $\Delta\epsilon = \epsilon_{10.8} - \epsilon_{12.0}$ the emissivity difference. U is total precipitable water content.

This approach was chosen for implementation in this work, because it was taylored to MSG SEVIRI. The input required by the algorithm comes from various sources: The viewing zenith angle θ is computed in preprocessing as specified above. Precipitable water path U is computed using the technique described above. For surface emissivity, a new method had to be developed to approximate this parameter:

In their approach to land surface temperature computation, Kerr *et al.* (1992) estimate ground temperature using a vegetation index as

an indication of vegetation cover. The underlying assumption is that emissivity increases linearly with fractional vegetation cover. This same simple principle is now applied in a new explicit ground emissivity estimation as well:

$$\epsilon_\lambda = \epsilon_\lambda(s) + V(\epsilon_\lambda(v) - \epsilon_\lambda(s)) \tag{3.16}$$

with ϵ_λ the surface emissivity at wavelength λ, $\epsilon_\lambda(s)$ the emissivity for a bare soil surface, $\epsilon_\lambda(v)$ emissivity for a fully vegetated surface and

$$V = \frac{NDVI - NDVI(s)}{NDVI(v) - NDVI(s)} \tag{3.17}$$

a new vegetation scaling factor. The Normalised Difference Vegetation Index (NDVI) of a pixel is given by

$$NDVI = \frac{r_{0.8} - r_{0.6}}{r_{0.8} + r_{0.6}} \tag{3.18}$$

based on reflectance (r) in the near infrared ($r_{0.8}$) and red ($r_{0.6}$) parts of the spectrum. $NDVI(s)$ is the NDVI for bare soil and $NDVI(v)$ for fully vegetated surfaces.

The emissivities $\epsilon(s)$ and $\epsilon(v)$ were taken from Peres & DaCamara (2003) for 10.8 μm (0.9748 and 0.9890 respectively) and 12.0 μm (0.9761, 0.9908). $NDVI(s)$ and $NDVI(v)$ were derived empirically as minima and maxima from SEVIRI NDVI products and fixed at $NDVI(s) = 0.08$ and $NDVI(v) = 0.69$. Thus a new land surface skin temperature product could be successfully developed.

For sea surfaces, a sea surface skin temperature (SST) product is computed according to a formulation found for MSG by SAFNWC:

$$\begin{aligned} T_s(sea) &= 0.977 \cdot T_{10.8} + 21 \\ &\quad +1.127(\sec(\theta) - 1)(T_{10.8} - T_{12.0}) \\ &\quad +1.156 \quad [K] \end{aligned} \tag{3.19}$$

(Meteo-France, 2005, modified). This complements the land skin surface product over the ocean and seas.

For various applications (see chapter 4) surface temperature is of particular interest for the area under clouds. The schemes introduced above do not however offer any such information. Therefore, an interpolation had to be introduced. Interpolation is performed for the

areas under individual water cloud entities, i.e. spatially coherent and discrete water cloud 'patches' surrounded by clear pixels. The cloud entity concept is discussed in full in section 4.2. Interpolation uses the parameters latitude, longitude, elevation and NDVI derived from clear sky reflectance maps. Figure 3.5 shows the concept of skin temperature interpolation. While without this step, temperatures are only available for the areas around clouds, now the temperature below clouds can be estimated as well. This new type of data set will be of great utility for the algorithms developed in chapter 4.

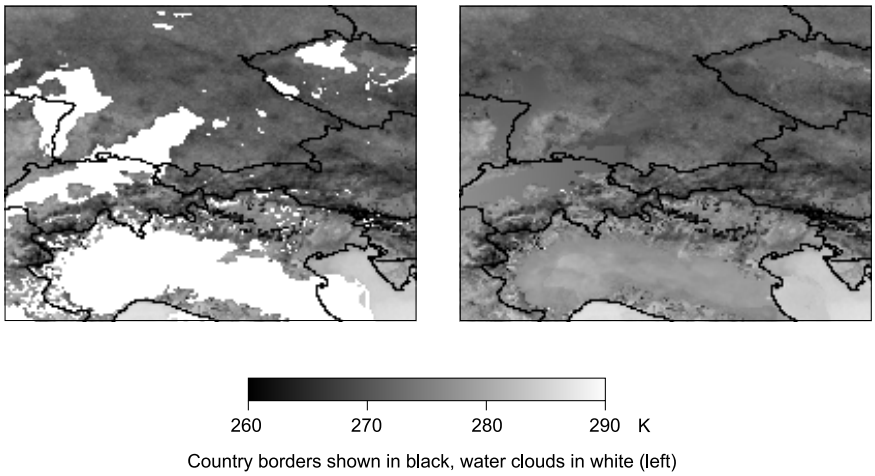

Figure 3.5: *Example for spatial skin temperature interpolation, 1030 UTC, 16 January 2005, for a region around the Alps (see border lines for orientation). The left hand panel shows the skin temperature before interpolation, the panel on the right contains interpolated temperatures.*

Chapter 4

Method Development

This chapter presents the development of the new operational fog observation scheme including theoretical and conceptual considerations with their implications on method design and implementation.

In the first section, the theoretical basis for the algorithm development is laid out. The conceptual design of the new method focuses on specific properties of fog. Before the method is introduced it is therefore necessary to consider how cloud properties manifest themselves in satellite imagery. The type of problem to be solved in remote sensing, i.e. to infer properties of an object by indirect measurements, is called an 'inverse problem'. The general nature of inverse problems is briefly discussed at the beginning of the chapter. The physical process on which remote sensing is based is radiative transfer, i.e. the changes radiation undergoes as it crosses the atmosphere. The principles of radiative transfer and their application to this study are discussed in the first section as well.

Following on the theoretical considerations, the development of the methodology is described in detail. Following the objectives laid out in chapter 2, algorithm design is presented in three parts:

1. Development of a new very low stratus delineation scheme, section 4.2
2. Adaptation and improvement of a method for cloud top height determination, section 4.3
3. Development of a new method for cloud thickness retrieval, section 4.4

As detailed before, the discrimination between ground fog and elevated fog is based on the comparison of surface elevation information from a DEM and cloud base heights computed from cloud top height and cloud thickness.

4.1 Theoretical Basis

4.1.1 The Theoretical Challenge: Inverse Problems

As stated in chapter 2, fog is to be detected based on a set of properties assumed characteristic of this meteorological phenomenon. However, no direct information on fog or even the presence or properties of any cloud is available directly from satellite imagery. Instead, remote sensing involves the solution of inverse problems. A very thorough treatment of this type of problem can be found in Shifrin & Tonna (1993). The following paragraphs briefly introduce the matter.

In a direct (or forward) problem data is mapped from real-life 'image' space f to a 'data' space d based on a known relationship $M(f)$ as

$$d = M(f) + n \tag{4.1}$$

with $M(f)$ the mapping function for f and n a noise quantity.

The inverse problem consists in trying to find the original image based on knowledge of d as

$$M(f) = d \tag{4.2}$$

Almost all measurements are based on such inversions. One example is the induction of an object's weight by reading the expansion of a string to which it is attached (Twomey, 1977b).

Following Hadamard (1923), an inverse problem is referred to as 'well-posed' given that a solution:

- Exists for any d.
- Is unique in image space.
- Is stable, i.e. the inverse mapping $d \rightarrow f$ is continuous.

In optical remote sensing, the measured quantity is radiation I in a channel i of a radiometer as described by the Fredholm equation of the first kind:

$$I_i + n_i = \int_a^b K_i(x) f(x) dx \tag{4.3}$$

(Stephens, 1994), where $f(x)$ is the sought-after distribution in the interval $a \rightarrow b$ and dx the step size; $K_i(x)$ is the kernel function yielding the relative contribution in the wavelength range of channel i, and n_i is an error (noise) in radiance measurement.

The inversion of the Fredholm equation is an example of an ill-posed problem, because its solutions are unstable and ambiguous. Stability is impaired by n_i, so that arbitrarily small changes in n_i can effect arbitrarily large changes in $f(x)$. Further, due to the combination of $K_i(x)$ and $f(x)$, values of I_i are not unique.

In a strict mathematical sense, ill-posed problems such as this cannot be solved. With application to real-world problems however, uncertainties can be minimised by:

- Reducing n, i.e. maximising accuracy in instruments.
- Selecting wavelengths suited to the problem at hand so that K functions are as sharp as possible.
- Considering instability and ambiguity in method design, based on good knowledge of the corresponding forward problem.

(Stephens, 1994).

The two most important approaches to inverse problem solution ('retrieval') in remote sensing are what Kokhanovsky (2003) refers to as the analytical (AM) and fitting (FM) methods. The former approach involves the direct analytical solution of radiative transfer equations for each case. Fitting methods in contrast model a range of cases by solving the forward function. Experimental data is then compared ('fitted') to these simulations. Inverse problem solution is further facilitated by restricting the problem. This involves either the retrieval of bulk (i.e. integrated) parameters or the explicit assumption of a parameter distribution (Shifrin & Tonna, 1993).

Throughout this work, the more accurate fitting method is applied. Some of the algorithms presented involve classifications rather than scaled property retrievals. Their solutions are more stable, as a discrete f is retrieved from a continuous d spectrum.

4.1.2 Cloud Properties and Their Effect on Radiative Transfer

The quantity measured in the data space is monochromatic radiance intensity, or brightness, I'_λ at each wavelength λ. It is expressed in units of energy per area per time per wavelength per steradian.

For the problem at hand, the corresponding image space are cloud properties, more specifically the amount and distribution of water in the cloud. In order to better understand how these properties impact on the radiation

signal recorded by the satellite sensor, the principles of radiative transfer and cloud optics will be briefly discussed in this section.

The radiance density received at the satellite (I'_λ) represents the original brightness signal of an observed object, I_λ, altered by changes dI_λ incurred on the path between the object and the sensor:

$$I'_\lambda = I_\lambda + dI_\lambda \quad [W\,m^{-2}\,sr^{-1}\,\mu m^{-1}] \tag{4.4}$$

The general radiative transfer equation explains this quantity in terms of radiation gains and losses as the distance ds is traversed:

$$dI_\lambda = (-I_\lambda + J_\lambda)(k_\lambda \rho_m ds) \quad [W\,m^{-2}\,sr^{-1}\,\mu m^{-1}] \tag{4.5}$$

ρ_m $[g\,m^{-3}]$ is the density of the medium, in the problem at hand a cloudy atmosphere; J_λ $[W\,m^{-2}\,sr^{-1}\,\mu m^{-1}]$ denotes the source function. This latter parameter quantifies radiation gained due to emission and scattering at wavelength $\lambda\,[\mu m]$ along the path $ds\,[m]$. k_λ $[m^2\,g^{-1}]$ is the mass extinction cross section for the same wavelength, a measure for radiation lost due to scattering and absorption. The process of atmospheric radiative transfer is shown in overview in figure 4.1.

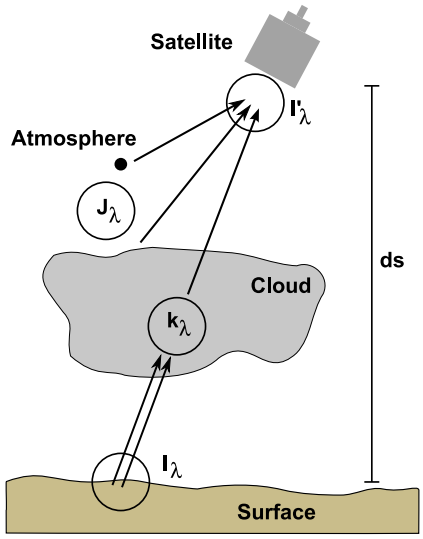

Figure 4.1: *The path of a radiation quantity I_λ through a cloudy atmosphere. As I_λ traverses a path ds, radiation is removed by absorption (k_λ) and added by scattering and emission (source function J_λ).*

The extinction of a radiative signal as it traverses a cloud is of particular importance. This part of the radiative transfer equation will thus be followed

up in the succeeding paragraphs. The product of $k_\lambda\,[m^2\,g^{-1}]$ and $\rho\,[g\,m^{-3}]$ of a medium (water in the case of clouds) yields the molecular extinction coefficient β_e defined by

$$\beta_e = \beta_s + \beta_a \quad [m^{-1}] \tag{4.6}$$

with $\beta_a\,[m^{-1}]$ the absorption and $\beta_s\,[m^{-1}]$ the scattering coefficient. The extinction therefore is a combination of radiation loss by (diffuse) scattering and molecular absorption. Extinction is directly related to visibility by Koschmieder's law:

$$V = \frac{1}{\beta_e} \ln\left(\frac{1}{\varepsilon}\right) \quad [m] \tag{4.7}$$

where ε is the contrast threshold [%]. For the commonly applied contrast threshold of 2 % this evaluates to $V = 3.912/\beta_e$ (Young, 1993).

In atmospheric remote sensing, extinction matters as an integrated value over a path $dz\,[m]$ from $z1$ to $z2$. It is called the optical path and defined by

$$\tau_{(z1,z2)} = \int_{z1}^{z2} \beta_e dz \tag{4.8}$$

(Goody, 1995)

For $z1$ a point of interest on the earth surface and $z2$ the satellite sensor, τ is called the atmospheric optical depth. For $z1$ the base of a cloud and $z2$ the cloud top, τ is referred to as cloud optical depth. For the remainder of this document, τ will be used as the cloud optical depth. In contrast to the variable extinction coefficient introduced above, τ has a direct impact on the satellite signal. τ can be related to cloud physical properties and thus is of great importance to the problem of this study. The nature of these relations will be explored in the following.

The extinction coefficient is related to the second moment of the droplet size distribution function by

$$\beta_e = \int_0^\infty Q_e \pi a^2 n(a) da \quad [m^{-1}] \tag{4.9}$$

(Lindner & Li, 2000), $a\,[\mu m]$: droplet size, $n(a)$: number of droplets of size a, da droplet size step, Q_e: extinction efficiency factor $= f(a, \lambda)$

From equations 4.8 and 4.9 follows

$$\tau = \Delta_z \int_0^\infty Q_e \pi a^2 n(a) da \tag{4.10}$$

Liou (2002). For droplet size distributions with peaks in the area of larger droplets, extinction and τ will thus increase as well.

For values of the size factor $x = 2\pi a/\lambda$ (droplet cross section in relation to wavelength) significantly larger than 1, $Q_e \cong 2$. This situation generally holds true for cloud droplets in the visible range of the spectrum (small wavelengths!), so that variations in Q_e can be neglected in equation 4.10 (Chylek, 1978; Liou, 2002).

Just like extinction and optical depth, the concentration of liquid water at a given point in a cloud, cloud liquid water content ρ_c, can be expressed as a function of the droplet size distribution, in this case using the third moment:

$$\rho_c = \frac{4\pi}{3}\rho_l \int a^3 n(a) da \quad [g\,m^{-3}] \tag{4.11}$$

(Liou, 2002; Pinnick *et al.*, 1979; Chang & Li, 2003) with ρ_l the density of liquid water.

The integration of ρ_c over the thickness of the cloud yields cloud liquid water path $W = \Delta z \overline{\rho_c} [g\,m^{-2}]$ (where $\overline{\rho_c}$ is the average liquid water content).

Knowledge of the droplet size distribution would therefore allow for the inference of cloud optical thickness and liquid water path. Unfortunately, this parameter is not known. However, the droplet size distribution is commonly approximated by the droplet effective (or equivalent) radius a_e of the given distribution, defined by

$$a_e = \int \pi a^3 n(a) da / \int \pi a^2 n(a) da \quad [\mu m] \tag{4.12}$$

In contrast to a mean radius, a_e includes the droplet cross section as a weighting factor. The amount of sunlight scattered and absorbed by a cloud mainly depends on this parameter, independent of the actual droplet size distribution present in the given cloud (Hansen & Travis, 1974).

From equations 4.10, 4.11, 4.12 and the definition of liquid water path the following relationship can be derived:

$$a_e \cong \frac{3W}{2\rho_l \tau} \quad [\mu m] \tag{4.13}$$

with ρ_l the density of liquid water $[g\,m^{-3}]$

This relationship shows how extinction and thus radiance intensity measured at the satellite sensor is influenced by the integrated water column and droplet size distribution. At constant liquid water path W smaller droplets will have a higher τ and also be more reflective; at constant a_e, increasing W will raise τ as well.

Thus it can be seen that the distribution of water in clouds significantly impacts on the radiative signal received at the satellite sensor. It is the inversion of this relationship that forms the basis of the methodology to be presented in the following chapters. The techniques applied in so doing either implicitly or explicitly address the cloud parameters introduced and discussed above.

4.2 Detection of Very Low Stratus

As shown in figure 2.4, the detection of very low stratus clouds is the first component of the fog detection scheme. The discussion of fog properties and processes in chapter 2 has shown that fog can be addresses as a very low stratiform cloud. The identification of this type of cloud is at the core of the new method introduced in this chapter. A distinction between ground fog and elevated fog follows in the succeeding sections.

To ensure a clean delineation and exclusion of all unwanted surfaces, the newly developed scheme makes use of not one but a series of tests. Each of these tests explicitly or implicitly addresses a property assumed for fog. These assumptions are (cf. chapter 2):

- Fog is a *cloud*
- in the *water* phase
- composed of *small droplets*,
- *low* above the ground and
- with a *stratiform surface*.

The tests are of an exclusive nature, i.e. any pixels failing one test will be excluded from further testing as obviously not covered by fog. In this way the scheme becomes increasingly fine-grained, with each test building on the results of all previous rules. As the properties tested for manifest themselves not only in the spectral, but also in the spatial domain (cloud altitude and surface), tests are developed in both realms. The first two items in the above list are addressed spectrally, the last two spatially, and the third item by a combination of both types of test.

Figure 4.2 gives an overview of the scheme to be introduced in the following. It shows all of the individual tests in context and highlights the exclusion component of very low stratus testing: All pixels or entities not meeting the criteria set in one of the tests are rejected as obviously not covered by fog and will not be considered in any of the following tests.

The new technique thus consists of a chain of individual tests. Most of these tests are new developments, others had to be adapted to the MSG SEVIRI system. This is indicated in figure 4.2 as well. The following sections introduce the components of the very low stratus delineation scheme, along with their physical basis and application.

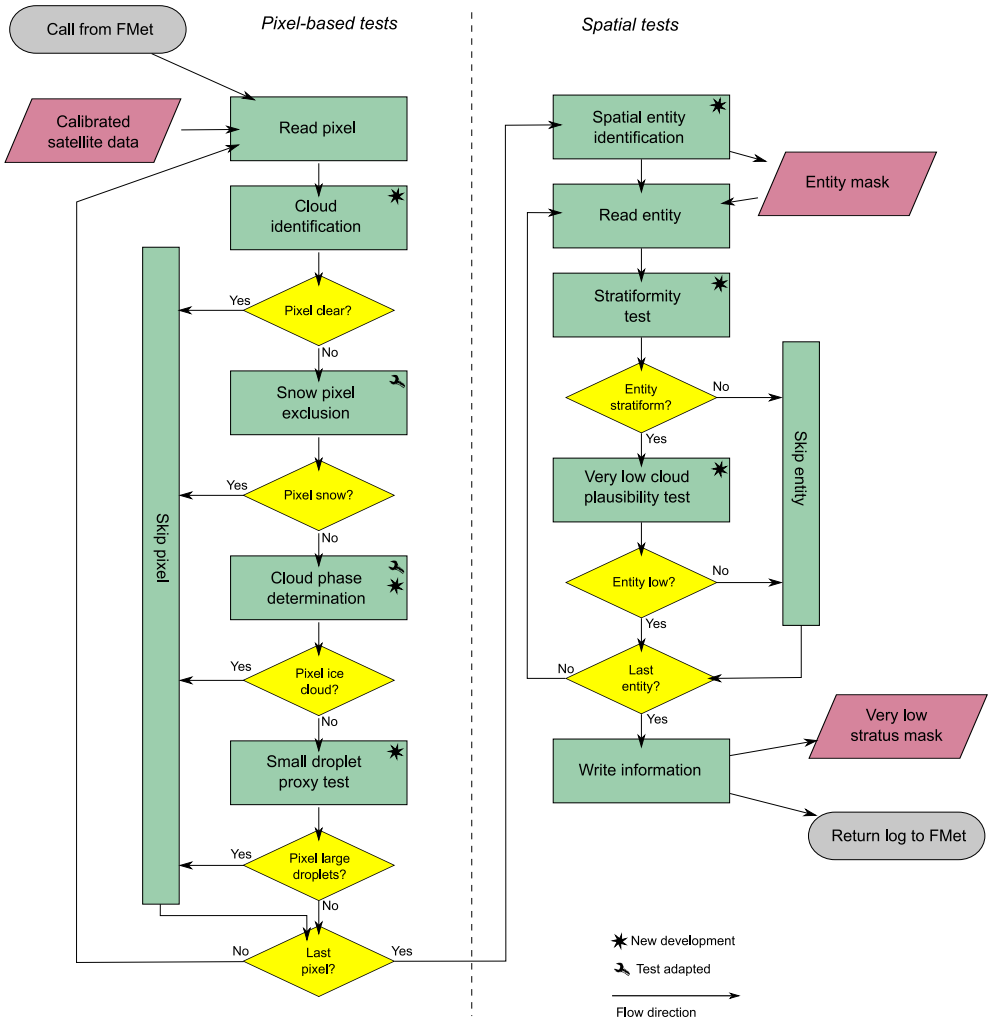

Figure 4.2: *An overview of the fog/very low stratus area delineation algorithm. After preprocessing the satellite data enters the classification scheme. After exclusion of some confirmed non-fog pixels in initial cloud masking, the remaining areas undergo a series of specific tests for fog properties. 'Not fog' indicates that a pixel or entity of pixels will no longer be considered in succeeding steps. For details see text.*

4.2.1 Cloud Identification

In a first step, a separation of clear and cloud-contaminated pixels is achieved using a newly developed algorithm. The basic assumption of this new test is that reflectivity is higher for cloudy than for clear areas. Reflectivity is indirectly assessed using observed radiances at thermal and medium infrared wavelengths. While the infrared channel centred at 10.8 μm represents thermal emission of surfaces (roughly corresponding to temperature), the 3.9 μm channel includes both a thermal and a solar component. This is due to the different electromagnetic spectra of sun and earth as shown in figure 4.3 and explained by Wien's displacement law ($\lambda_{max} \propto T^{-1}$ with λ_{max} the wavelength with maximum emission and T the temperature of a body). It can be seen that the terrestrial (thermal) signal clearly dominates at 10.8 μm, while solar and terrestrial signals combine around 3.9 μm.

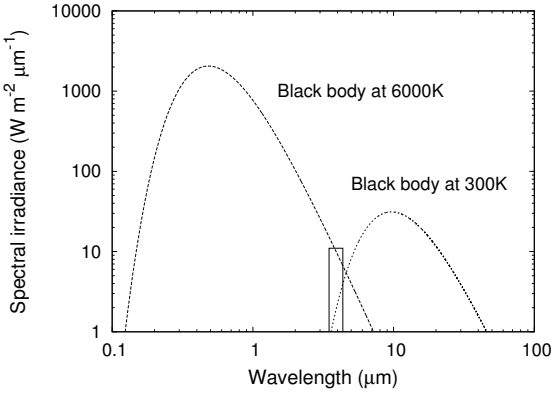

Figure 4.3: *Earth and sun electromagnetic spectra approximated by blackbodies with temperatures of 300 K (earth) and 6000 K (sun). The solid line box indicates the position of the SEVIRI 3.9 μm channel. Solar and terrestrial signals mix in this channel.*

The cloud detection algorithm introduced here takes the difference between the total signals at both channels as an indication of surface reflectivity. It is expected that the reflectivity (solar signal!) of clear ground surfaces is very small, while cloud reflection is large. In this light, the underlying assumptions of the test are:

$$I_{IR}(cloud) < I_{MIR}(cloud) \quad (4.14)$$

$$I_{IR}(clear) \approx I_{MIR}(clear) \quad (4.15)$$

with I $[W\,m^{-2}\,\mu m^{-1}\,sr^{-1}]$ the intensity in the infrared (IR) and medium

infrared (MIR) channels for cloudy (*cloud*) and clear (*clear*) areas.

Therefore, the difference $I_{IR} - I_{MIR}$ can be used to distinguish between both surfaces. For comparability, radiances for both channels are converted to blackbody temperatures, i.e. the temperature expected of a black body with this radiance (cf. chapter 3). This conversion is performed for practical reasons only; blackbody temperatures are used as a unit only.

An example of such a blackbody temperature difference image is shown in figure 4.4. For cloudy surfaces, the difference between both blackbody temperature values will generally be smaller than 0, while for clear surfaces it will be around 0, or slightly above due to a lower emissivity in the middle IR. The frequency distribution of blackbody temperature differences for the scene shown in figure 4.4 can be seen in figure 4.5 (left hand panel). Cloudy and clear peaks are indicated in the histogram. On the right hand side in the same figure a slightly different distribution is shown for another scene. Yet, the same general patterns can be found in both histograms.

The advantage of using a combination of an IR and an MIR channel for measuring reflectivity over the use of a visible channel (as in Karlsson, 1989) is that a much clearer separation of cloudy and clear pixels is possible. This is due to the uniformly low reflectivity of cloud-free surfaces in the MIR (and thus the $IR-MIR$ difference) compared to significant variations in the channels in the visible range. This fact allows for a much better separation of both surface types.

A decision on cloudiness is made as follows:

$$\Delta T(a) = T_{IR}(a) - T_{MIR}(a) \tag{4.16}$$

$$\Delta T(a) \leq v_t(C) \rightarrow a \in C \tag{4.17}$$

with $T_{IR}(a)\,[K]$ the infrared blackbody temperature at pixel a, $T_{MIR}(a)\,[K]$ the same in the medium infrared, $v_t(C)\,[K]$ a threshold value for cloudiness and C the class of cloudy pixels.

A threshold value of observed blackbody temperature difference between cloud and cloud-free areas must be determined. This threshold depends on viewing geometry, season and the atmospheric gas column. At $3.9\,\mu$m and with a large spectral width, the SEVIRI MIR channel in part overlaps with the CO_2 absorption band centred around $4.2\,\mu$m. Thus it is not possible to use a fixed threshold value.

A procedure for dynamically retrieving a proper threshold was developed. It is applied to each single slot and consists of an analysis of the histogram of the blackbody temperature differences in a scene (see figure 4.5

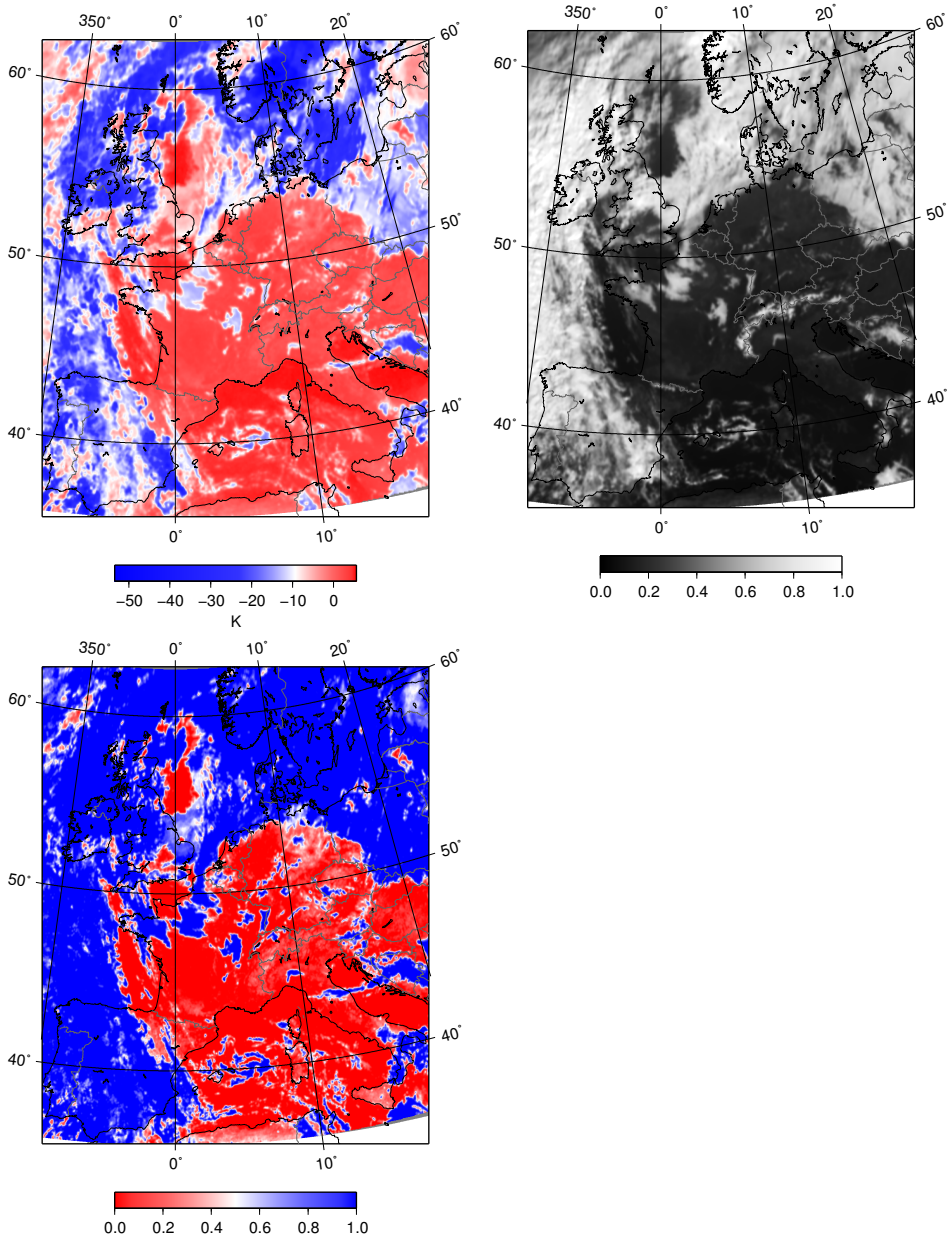

Figure 4.4: *Blackbody temperature difference $T_{10.8} - T_{3.9}$ for 1000 universal time co-ordinated (UTC), 5 November 2003 (top left). The corresponding reflectance image ($\lambda = 0.6\,\mu m$) is shown in the top right hand panel for orientation. The panel at the bottom shows the cloud confidence level computed for this scene (for details see text).*

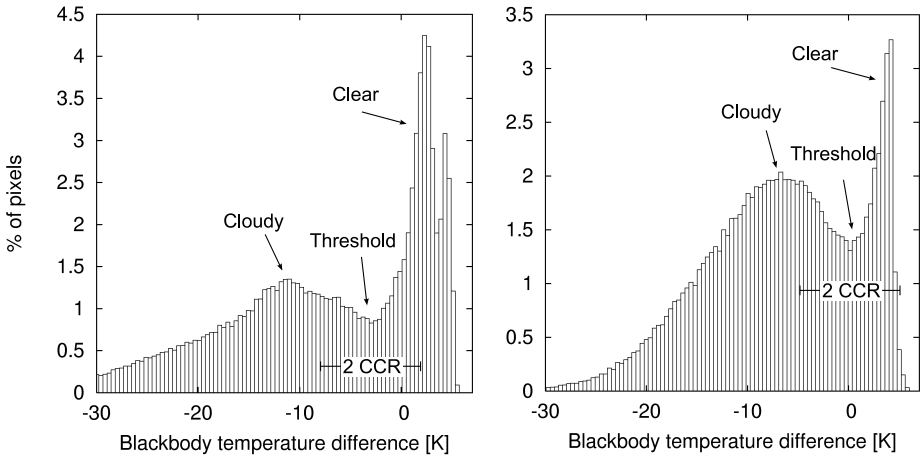

Figure 4.5: *Frequency distribution of $T_{10.8} - T_{3.9}$ for 5 November 2003, 1000 universal time co-ordinated (UTC) (left) and 18 April 2004, 1600 UTC (right). Distinct peaks of clear and cloudy pixels can be identified in the histograms (marked by arrows). At the relative minimum in between the two peaks a threshold value is identified automatically. The constant cloud confidence range (CCR, see text) is located around this threshold.*

for representative examples). The histogram is computed with a resolution of three steps per Kelvin. In this histogram the clear sky peak is identified. Moving down the data value classes from this peak, the nearest pronounced relative minimum in the histogram is detected, also accounting for local histogram slope. This minimum is then used as a threshold to separate clear from cloudy pixels in the image. The automatically detected thresholds are marked in figure 4.5. It can be seen that both thresholds are at slightly different levels within the respective distribution.

In order to account for the uncertainties involved in threshold testing, a confidence level is computed for use by later tests.

$$P_c(a) = \frac{\Delta T(a) - v_t(C) - CCR}{-2CCR} \tag{4.18}$$

with P_c the cloud confidence level, $0 \leq P_c \leq 1$ and CCR the cloud confidence range, i.e. the range between the threshold and a certain clear or a certain cloudy pixel. All values in the centre of the clear peak are to be assigned a confidence level of 0, those in the centre of the cloudy peak of 1. To accommodate the average gap between the two peaks, CCR is set to 5 K (also marked in figure 4.5). A value $\Delta T(a) = v_t(C)$ is thus assigned a P_c of 0.5. The cloud confidence level will be of use in cloud height determination

(section 4.3).

The cloud confidence range CCR has been determined by statistical evaluation of the distance between the clear and cloudy pixel peaks in 100 random scenes for 2004. This distance was found to average 11.6 K. With 5 K the cloud confidence range was set to about half this distance to approximate the average relative position of the cloud threshold.

A sample cloud confidence level image is shown in figure 4.4 alongside the corresponding blackbody temperature difference and visible images. The cloud confidence image shows a clear separation between cloudy and clear areas with confidence transition in between these areas.

4.2.2 Snow Pixel Elimination

Most of the time, the relative minimum identified as the cloud threshold represents more than zero pixels (as in figure 4.5). Thus a certain crudeness is inherent in this test. These uncertain pixels are mostly snow-covered: The reflectivity of snow in the medium infrared is lower than that of clouds but higher than for clear snow-free areas (Wiscombe & Warren, 1980). Therefore, snow is removed in the next step.

In order to clean up the clear-cloudy delineation, snow-covered pixels that have wrongly been classified as clouds need to be explicitly excluded. This is done in a snow pixel elimination test, which includes the adaptation and implementation of insights and approaches known from other platforms. Snow-testing is based on the insights that snow:

- Has a certain minimum reflectivity.
- Has a certain minimum temperature.
- Displays a lower reflectivity than clouds in the near-middle infrared (1.6 μm) combined with a slightly higher level of absorption (Wiscombe & Warren, 1980), while both behave similarly in the visible range (0.6 μm). This principle is shown in figure 4.6, where snow pixels can clearly be separated from other pixels. The reflectance differences in the near-middle infrared are mostly due to particle size (snow being much larger, Dozier, 1989).

The first two criteria are tested against predefined thresholds. These are 0.11 for 0.8 μm reflectance and 256 K as the minimum blackbody temperature at 10.8 μ. These thresholds were determined based on published snow properties (e.g. Wiscombe & Warren, 1980; Warren & Wiscombe, 1980; Dozier & Painter, 2004; Dozier, 1989) and corroborated by visual

inspection of long time series (3 months) of SEVIRI data. The third criterion is tested using the Normalised Difference Snow Index (NDSI) introduced in equation 4.19.

$$NDSI = \frac{r_{0.6} - r_{1.6}}{r_{0.6} + r_{1.6}} \tag{4.19}$$

(Dozier & Painter, 2004; Dozier, 1989), with r_λ the reflectance at wavelength $\lambda\,[\mu m]$.

NDSI testing has been found to be reliable and is used operationally on Moderate Resolution Imaging Spectroradiometer (MODIS) (Hall *et al.*, 2001). For MSG SEVIRI, simulations with the Streamer radiative transfer model (see chapter 3 for model description) yielded an NDSI cut-off level of about 0.5 for the distinction between snow-covered surfaces and clouds. The NDSI values computed for a selection of surfaces are presented in table 4.1.

Surface	NDSI
Fresh snow	0.91
Melting snow	0.96
Melting snow and vegetation	0.58
Opaque ice cloud	0.46
Opaque water cloud	0.23
Vegetation (clover)	-0.07

Table 4.1: *NDSI values modelled for various surfaces. 'Melting snow' is assumed to have larger grains than 'fresh snow'. The water cloud modelled has an optical depth of 20, droplet effective radius of 10 μm and is at an altitude of 3 km. The ice cloud is at 10 km altitude, has the same optical depth and an effective radius of 35 μm.*

Long-time visual inspection of SEVIRI data (3 months) has revealed a systematic under-estimation of the actual SEVIRI 1.6 μm radiances by the Streamer model. Consequently, actual NDSI values are smaller than those presented in table 4.1 (see equation 4.19). A more appropriate threshold value was found at 0.4. This threshold is also shown in figure 4.6. Where the NDSI exceeds the threshold and the two other criteria are met, a pixel is rejected as snow-covered.

4.2.3 Cloud Phase Determination

After the delineation of the cloud area, water clouds need to be identified. This is implemented as a three-step procedure: First, a simple cloud tem-

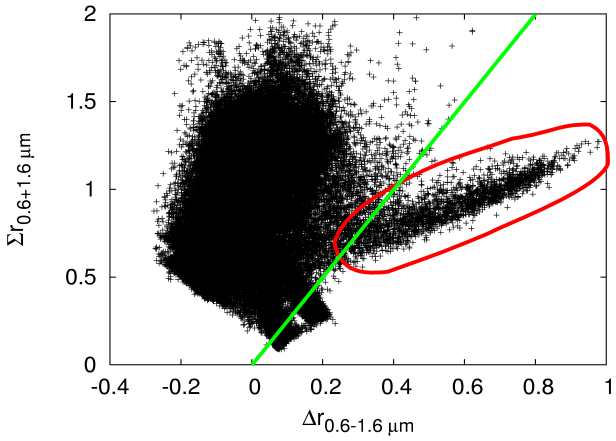

Figure 4.6: *The sum of VIS and NIR reflectances Σr vs. the difference of both reflectances Δr as used in the Normalised Difference Snow Index (NDSI). Snow-covered pixels are concentrated in the linear extension to the right edge of the chart and circled in red. They are marked by a strong reflective signal at 0.6 μm and a weak signal at 1.6 μm. The NDSI threshold is shown in green.*

perature test removes any cloud pixels too cold to be in the water phase. Then, a newly developed cloud phase test explicitly identifies areas with clouds in the water phase. In rare cases, semi-transparent thin cirrus clouds may be missed by these tests. Therefore, in a third step, two additional thin cirrus tests were adapted to MSG SEVIRI to exclude any such pixels.

First, all pixels too cold to be in the water phase are removed using a black body temperature threshold in the thermal infrared (for water clouds, $T_{10.8} > 230\,K$ Houze, 1993). While this removes the coldest ice clouds, the remaining pixels may still be covered by ice clouds warmer than this threshold.

Among the remaining pixels, water cloud identification is based on divergent absorption characteristics of water in the liquid and solid phases in different infrared regions. Figure 4.7 shows the imaginary part of the refractive index in the infrared. This parameter quantifies absorption of the given material at each wavelength and is related to the blackbody temperature of an object. Between 8 and 10 μm absorption of ice and water particles is very similar. From 10 to about 13 μm however, ice absorbs much stronger than water. Therefore, an ice cloud can be expected to have a much lower blackbody temperature in this wavelength region than a water cloud of the same thickness, while both temperatures should be about the same around 9 μm (Strabala *et al.*, 1994). The blackbody temperature difference between

both wavelengths ($T_{12.0} - T_{8.7}$) should therefore be smaller for ice clouds. This property is used in the newly developed cloud phase test.

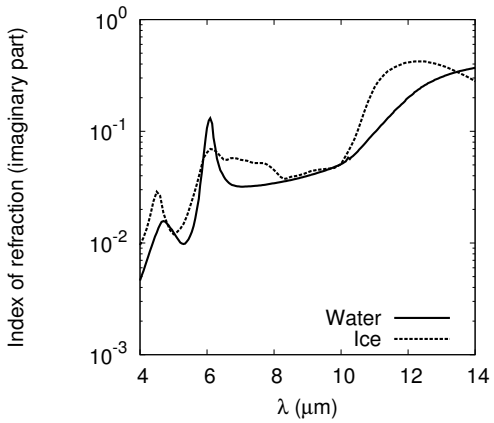

Figure 4.7: *Imaginary part of the refractive index (absorption) for liquid water and ice in part of the infrared. Data according to* Segelstein *(1981, water) and* Warren *(1984, ice).*

In radiative transfer simulations with the Streamer model (cf. chapter 3), a threshold of 0.65 K has been identified for the blackbody temperature difference between 12.0 and 8.7 μm. The computed blackbody temperature differences for various ice and water clouds are shown in figure 4.8. The resulting curves show a strong dependency on the viewing zenith angle (θ). Therefore, the threshold $v_t\,[K]$ needs to be normalised by viewing geometry as

$$v_t = \frac{0.65}{\cos\theta} \quad [K] \tag{4.20}$$

with θ the viewing zenith angle.

This dynamic threshold is also shown in figure 4.8. Where the blackbody temperature difference exceeds the threshold, a water cloud is assumed. The figure very clearly shows the separation between water and ice clouds achieved by this threshold.

Next, thin cirrus clouds are identified by two different techniques to ensure that no cirrus-covered pixels are missed. Both tests make use of the IR window channels and the different sensitivities each of the three available channels has to thin cirrus clouds:

- Cirrus is detected by means of the split-window IR channel blackbody temperature difference ($T_{10.8} - T_{12.0}$). This difference is compared to a

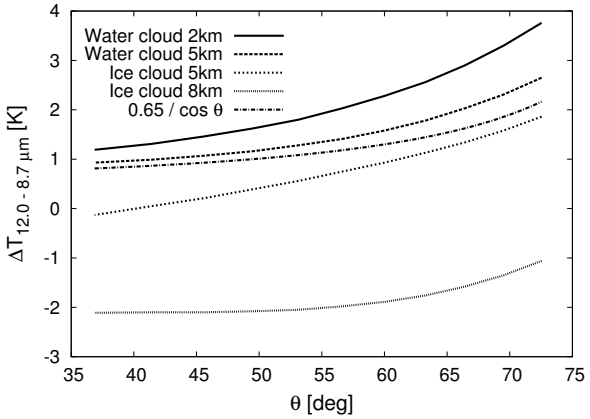

Figure 4.8: *Viewing zenith angle θ vs. blackbody temperature difference $\Delta T_{12.0-8.7\mu m}$ for clouds in the water and ice phases. Water clouds are shown at altitudes of 2 and 5 km, ice clouds at 5 and 8 km. All clouds have a thickness of 500 m and typical particle sizes (water clouds: droplet effective radius $a_e = 15\mu m$, ice clouds: crystal effective radius $a_e = 35\mu m$).*

threshold dynamically interpolated from a lookup table based on viewing zenith angle θ and blackbody temperature at 10.8 μm (Saunders & Kriebel, 1988). The physical basis for this approach are emissivity differences at both wavelengths, as described in detail in Inoue (1985). This technique was adapted from the well-validated APOLLO cloud detection scheme (Saunders & Kriebel, 1988; Kriebel *et al.*, 2003).

- The second approach uses the difference between the 8.7 and 10.8 μm blackbody temperatures ($T_{8.7} - T_{10.8}$), founded on the relatively strong cirrus signal at the former wavelength (cf. Wiegner *et al.*, 1998). Where the difference is greater than 0 K, cirrus is assumed to be present.

4.2.4 Small Droplet Proxy Test

As mentioned in chapter 2, fog clouds are generally composed of small droplets. Thus, after the removal of clear and ice clouds pixels, the presence of small droplets in a cloud is tested for (see figure 2.4. This is done implicitly using radiances in the middle infrared (3.9 μm channel) in a newly developed test. The underlying assumption relates to the specific radiative properties of fog and stratus as compared to other clouds and clear areas at this wavelength (Hunt, 1973). The small droplets usually found

in fog (usually no larger than 20 μm, ROACH, 1994) are significantly more reflective than larger droplets at this wavelength. Figure 4.9 shows this decrease of cloud middle infrared intensity with increasing cloud droplet size as computed with the Streamer radiative transfer model. Due to droplet reflectivity, the solar component of the signal received from fog areas therefore exceeds that from both land and clouds with larger droplets, so that the total signal received from fog areas exceeds that of all other surfaces.

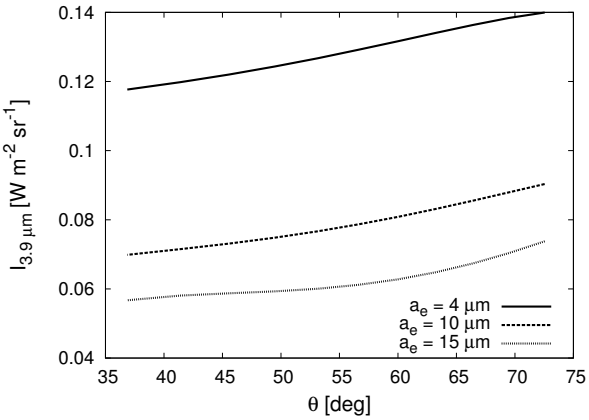

Figure 4.9: *Middle infrared intensity $I_{3.9\mu m}$ as a function of droplet radius a_e and viewing zenith angle θ for a water cloud with a thickness of 200 m.*

Clouds with larger droplets have a weaker reflection r and thus solar signal I^s_{MIR} (equation 4.21) in the middle infrared. At higher altitude, they also have a smaller thermal component I^t_{MIR} than land, putting their total signal in the MIR I_{MIR} below that of clear areas (figure 4.11). Thus, a separation of low clouds with small droplets from land and higher clouds with larger droplets appears feasible in the MIR.

$$\begin{aligned} I_{MIR} &= I^s_{MIR} + I^t_{MIR} \quad [Wm^{-2}sr^{-1}\mu m^{-1}] \\ I^s_{MIR} &= f(r) \\ I^t_{MIR} &= f(T, \epsilon) \end{aligned} \tag{4.21}$$

A sample 3.9 μm radiance image can be seen in figure 4.10. The vertical line indicates a profile, the values along which are plotted in figure 4.11. It can be clearly seen that 3.9 μ radiance is highest in the area covered by fog, lowest in the regions covered by cirrus and other medium and high clouds, and in between both levels in clear regions.

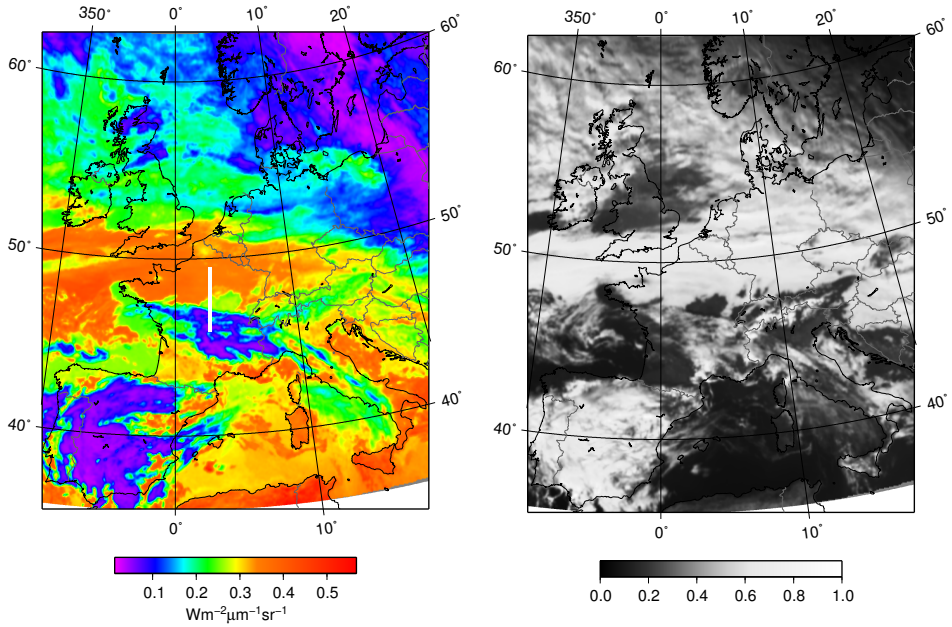

Figure 4.10: *A 3.9 µm radiance image for 5 December 2003, 1300 universal time co-ordinated (UTC) (left) and the corresponding 0.6 µm visible image (right). The vertical white bar over France (left) indicates the location of the profile shown in figure 4.11.*

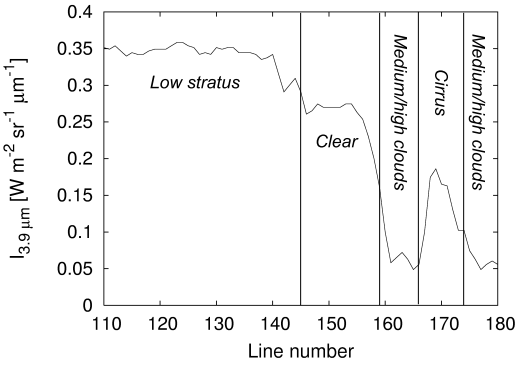

Figure 4.11: *A profile of radiances registered in the 3.9 µm channel over central France, 5 December 2003, 1300 UTC (cf. figure 4.10 for precise location). The profile extends from line 110 to line 170 of the original image (north to south) and encompasses different types of cloud cover: fog (lines 110–145), no clouds (146–159), undifferentiated medium and high water clouds (160–166, 174–180), and cirrus (167–173).*

As mentioned above, CO_2 absorption also impacts on the signal in the 3.9 μm channel. This absorption varies with the length of the slant column between the satellite sensor and the observed feature. Therefore, a latitudinal dependence can be stated: The higher the latitude, the higher the absorption by CO_2 and the smaller the signal at 3.9 μm. To account for this, the 3.9 μm radiances for cloud-free land areas are averaged over 50 image rows at a time to obtain an approximately latitudinal value of the clear sky 3.9 μm signal. Wherever a cloud-covered pixel within the same 50 rows exceeds this radiance value, it is flagged 'small droplet cloud'. Where a pixel stays below the threshold, it is rejected as not qualifying for this category.

4.2.5 Spatial Entity Identification

At this point, water clouds with small droplets have been identified. The other two properties assumed of fog are low height and a stratiform surface. Fog height and stratiformity, i.e. homogeneity of the cloud surface, are spatial parameters. Therefore, they are most adequately addressed by tests not only considering individual isolated pixels, but environments in the 2D image pane. Spatial feature analysis therefore is a central component of the fog delineation scheme (see figure 4.2). In this way a significant advantage over conventional spectral tests is gained. The spatial analysis considers all pixels not rejected as obviously non-fog by any of the preceding tests.

This part of the scheme constitutes a new development. While the immediate environment of individual pixels has been considered in older schemes (cf. literature review in chapter 2), the entity concept introduced here presents a significant advance over this type of approach. Cloud and fog patches are now looked at as units in space; to this end, all remaining cloud pixels are grouped into spatially coherent and discrete entities. An entity in this context is defined as a set of adjoined pixels belonging to the same cloud class. The latter is derived from the tests described in the previous section. Each entity is assigned a unique ID (identifying common entity number) so that it can be considered as a discrete unit in further testing. Depending on the degree of segmentation effected by the spatial distribution of cloud classes, the entity areas may vary in size. Diagonal relations between pixels (i.e. pixels bordering each other at angles other than multiples of 90 degrees) are excluded in the clustering process, because they are likely to indicate separate or fragmented entities.

Entities are identified according to:

$$(|x_a - x_b| \vee |y_a - y_b|) = 1 \wedge C_a = C_b \quad \Rightarrow \quad b \in E(a) \tag{4.22}$$

for two image data points a and b with coordinates x, y in the image pane and memberships in cloud classes C_a and C_b. $E(a)$ is the entity a belongs to. Figure 4.12 shows an example of entities identified in a particular scene. Each small droplet water cloud entity is displayed in a different colour in this image. The entities identified in this step will be used in the following tests.

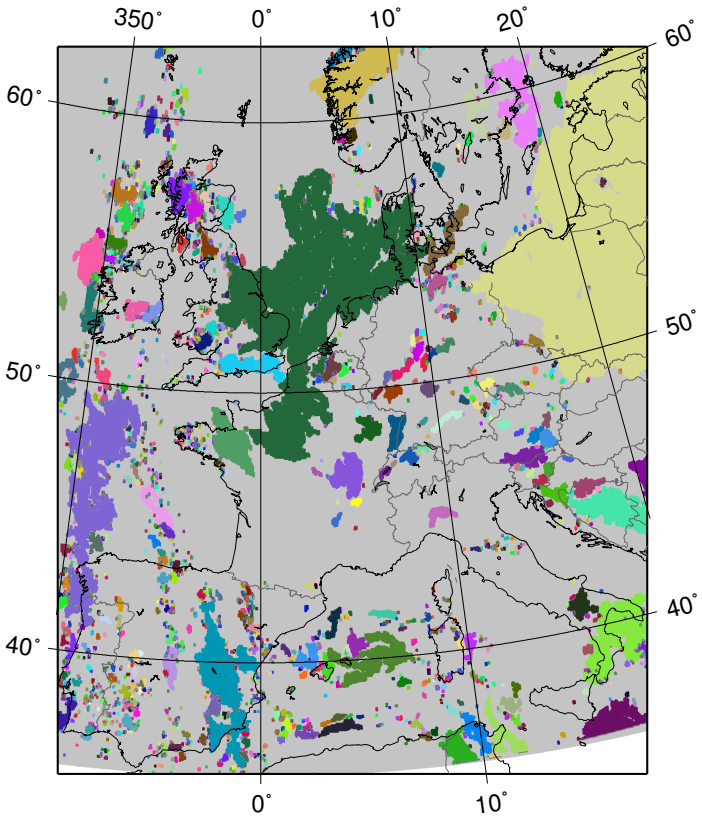

Figure 4.12: *Water cloud entities as identified in the course of very low stratus detection scheme. Each colour signifies one entity. The figure shows the scene of 1000 UTC, 5 November 2003. Each colour represents one water cloud entity (against a grey background). See figure 4.4 for orientation.*

4.2.6 Stratiformity Test

Based on the assumption that fog is a cloud trapped under an inversion (cf. chapter 2), a fairly homogeneous (or stratiform) cloud top surface height is expected. Since height information is not directly available, blackbody temperature for the infrared channel centred around 10.8 μm is taken as proxy information. As only relative height information is needed, this approach is considered appropriate.

This newly developed test is set up on the cloud entities delineated in the previous step. For each low cloud entity, the standard deviation of the black body temperature is determined in the thermal infrared channel at 10.8 μm. Where it falls below a certain threshold (2 K), the entity is identified as a stratus patch. Assuming a temperature lapse rate of 0.7 K / 100 m, a threshold of 2 K roughly corresponds to a height difference of 290 m. This threshold was determined and tuned empirically, by continuous monitoring of operational processing. In the absence of reference data, threshold identification again relied on visual inspection over a period of 3 months. It seems plausible that a cloud with a height variation of more than about 600 m will not be stratiform.

4.2.7 Very Low Cloud Plausibility Test

The purpose of the new altitude test is to determine the relative height of a cloud entity above ground and thus to reach a rough estimate whether a given cloud could potentially qualify as a very low cloud or not. A test of this kind may appear superfluous at this stage in the light of the more accurate cloud top height determination to be presented in section 4.3. The present very low cloud plausibility test is however included in the scheme to provide a preliminary (and rough) exclusion of any obvious high clouds. The clouds excluded here will not have to be considered in the succeeding processes, which effects a considerable advantage in computation time.

In the very low cloud plausibility test, the 10.8 μm blackbody temperature of every fringe pixel of a given entity is compared to that of any and all bordering clear pixels. In order to minimise the risk of underestimating cloud altitude where pixels with only partial cloud cover are compared with clear pixels, the maximum blackbody temperature difference is located along the entity margin. At the moment, this test is confined to land areas, clear pixels covered by snow (as identified above) are not considered.

Using the blackbody temperature difference, the ground elevation for both the cloudy and the clear pixel, and an assumed atmospheric temperature lapse rate (0.7 K / 100m), cloud top altitude is estimated as follows:

$$z_t = \frac{T_{cf}(10.8) - T_{cc}(10.8)}{\Gamma} - (z_{cf} - z_{cc}) \quad [m] \tag{4.23}$$

where z_t is the cloud top height, $T_{cf}(10.8)$ the 10.8 μm blackbody temperature for a cloud-free pixel, $T_{cc}(10.8)$ the same for a cloud-contaminated pixel, $\Gamma\,[K\,m^{-1}]$ the atmospheric temperature lapse rate, $z_{cf}\,[m]$ the surface elevation of the cloud-free pixel and $z_{cc}\,[m]$ that for the cloud-contaminated pixel.

If z_t falls below a threshold of 1000 m, the cloud entity is classified as a potentially very low cloud. If the cloud appears to be higher, it is no longer considered a potential fog or very low stratus entity and disregarded in further tests.

The spatial tests conclude the fog/very low stratus delineation scheme. The areas not discarded in any of the steps of the scheme (see figure 4.2) constitute the fog/very low stratus area. This group includes ground fog, elevated fog and other low stratiform clouds.A further distinction between these classes is based on the techniques presented in the following sections.

An exemplary result of the very low stratus detection scheme with the most important other classes identified in the process is shown in figure 4.13.

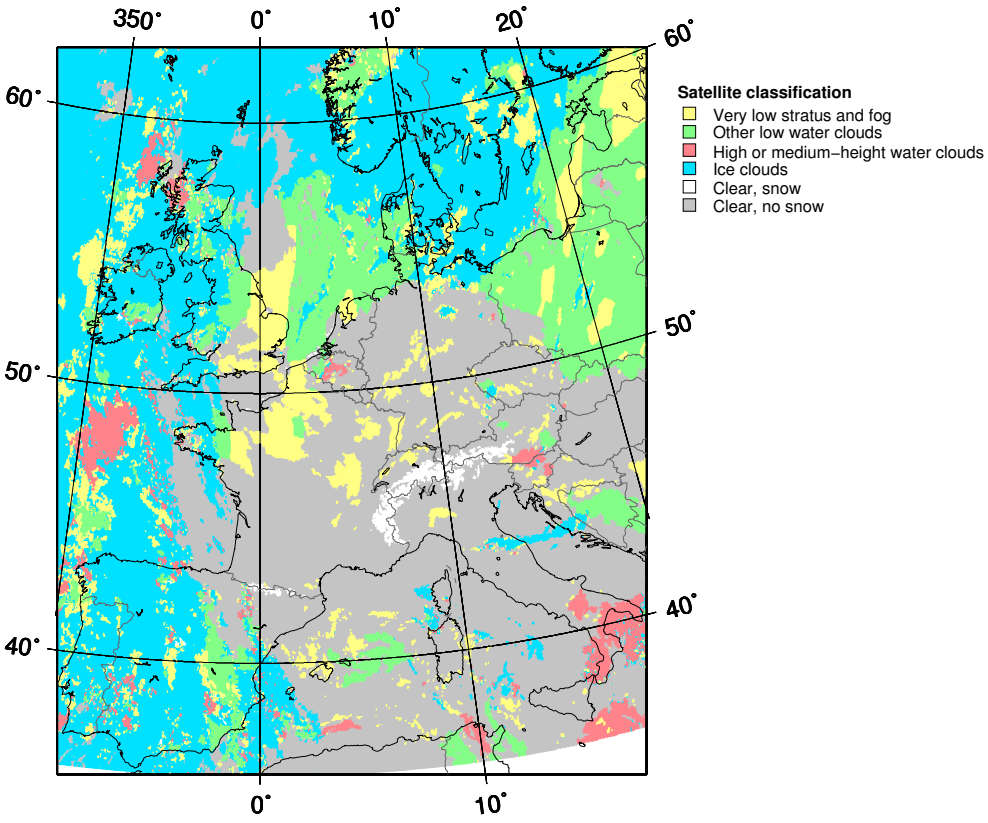

Figure 4.13: *Very low stratus/cloud classification for 5 November 2003, 1000 UTC (scene also shown in figures 4.4 and 4.12. This map shows the main cloud classes identified in the scheme described in this section.*

4.3 Cloud Top Height Determination

The determination of low stratus ground contact requires knowledge of cloud geometry as outlined in chapter 2 and summarised in equation 2.8. The retrieval of cloud top height is explained in detail in this section, while cloud geometrical thickness is covered in the next.

Since cloud top height determination is a major component of the new scheme a separate literature review for this field is warranted. This is presented first before the development of the new method is introduced on this basis.

4.3.1 Existing Approaches

A number of approaches to cloud height determination have been developed for application in different contexts. Some of these make use of multispectral measurements of atmospheric absorption, others rely on geometrical considerations.

Absorption by oxygen in the atmospheric band around 761 nm (O_2 A band, $\sim$ 758–778 nm) can be related to cloud top height when assessed in conjunction with radiances in a directly adjacent spectral band. The O_2 A band is deeper (i.e. the path of radiation through the atmosphere longer) for a low cloud than for a high cloud so that a larger portion of the cloud signal signal is removed. Cloud top height can be found by minimising the difference between a signal simulated in radiative transfer computations (RTC) and measured radiances, e.g. by use of least squares fitting (Fischer & Grassl, 1991; Koelemeijer *et al.*, 2001; Kokhanovsky *et al.*, 2006; Kokhanovsky & Rozanov, 2004; Kokhanovsky *et al.*, 2005; Kurosu *et al.*, 1998; Kuze & Chance, 1994; Rozanov & Kokhanovsky, 2004). While this method has been shown to reach a good accuracy in cloud top height retrieval (e.g. Fischer *et al.*, 1991), the required bands are unavailable on most present-day meteorological satellite systems, including MSG SEVIRI. However, Fischer *et al.* (2003) presented a feasibility study for inclusion of an O_2 A band channel on future geostationary systems (Meteosat Third Generation, MTG), so O_2 A cloud top height retrieval may become an option in 10–20 years.

The method known as CO_2 slicing is founded on similar principles. It makes use two bands $\lambda 1$ and $\lambda 2$ with one near the centre of the CO_2 absorption band around 15 μm and one at its perimeter. The bands are close enough to each other for the assumption $\epsilon_{\lambda 1} \simeq \epsilon_{\lambda 2}$ to be valid, where ϵ is cloud emissivity. The ratio of the radiances

$$\frac{I_{\lambda 1} - I_{\lambda 1}^{cf}}{I_{\lambda 2} - I_{\lambda 2}^{cl}} \tag{4.24}$$

I: measured radiances, I^{cf} for a clear pixel, can be taken as a measure of absorption in both bands and thus linked to cloud top pressure (Antonelli *et al.*, 2002). Combined with knowledge of the atmospheric temperature and transmittance profiles, cloud top pressure can be reconstructed (Fischer *et al.*, 2003; Menzel & Strabala, 1997; Frey *et al.*, 2003; Park *et al.*, 1997).

The applicability of this method is limited where the observed difference $I_\lambda - I_\lambda^{cf}$ is smaller than the instrument noise in at least one of the channels used. This problem is very frequently encountered for low cloud situations (Fischer *et al.*, 2003). Thus, this method too is inappropriate for the problem to be solved in this work.

Geometrical considerations are the basis of a number of multi-view cloud top height retrievals. When a cloudy pixel is viewed from two different angles with known relative positions of the viewing systems its height above the ground can easily be computed ('parallax adjustment'). This technique is applied on systems with more than one viewing angle (Muller *et al.*, 1999a,b; Poli *et al.*, 2000; Prata & Turner, 1997; Zong, 1998; Zong *et al.*, 2002; Seiz & Davies, 2006), but also to simultaneous observations from two or more systems, e.g. Meteosat 5 and 7 or GOES 8 and 9 (Campbell & Holmlund, 2004; Mahani *et al.*, 2000; Wylie *et al.*, 1998). SEVIRI as a single view instrument could only be used in conjunction with another system, such as Meteosat 7. However, SEVIRI's spatial sample rate is unmatched in its orbit at the moment so that a combination with a different system would incur a loss of spatial information. Once MSG 2 is operational however, multi-view retrievals of cloud top height will be an option on SEVIRI.

Simpson *et al.* (2000b,a) use cloud shadow information to infer the height of a cloud by

$$L'_s = z_t \sqrt{\tan^2\theta_0 + \tan^2\theta - (2\tan\theta_0 \tan\theta \cos\psi)} \quad [m] \tag{4.25}$$

(Simpson *et al.*, 2000b), with L'_s the observed length of the cloud shadow in the satellite image, z_t $[m]$ cloud top height, θ the viewing (satellite) zenith angle, θ_0 the solar zenith angle and ψ the relative azimuth angle between satellite and sun. While this approach is very straightforward and in theory has a very low error margin, it relies on very accurate measurements of cloud shadow length. With the relatively course spatial resolution of even

the SEVIRI HRV channel and cloud shadows at angles varying with solar geometry, this criterion cannot be fulfilled satisfactorily for low clouds.

A number of authors (Minnis *et al.*, 1992; Randriamampianina *et al.*, 2000; Reynolds & von der Haar, 1977) compare infrared temperature measured at the satellite sensor with an assumed static atmospheric lapse rate. Minnis *et al.* (1992) derived an average boundary layer lapse rate of 7.1 K per km from soundings, Randriamampianina *et al.* (2000) used European Centre for Medium Range Forecasting (ECMWF) forecast temperature profiles and Reynolds & von der Haar (1977) relied on upper air soundings.

For fog patches limited by surrounding terrain, a trend surface analysis can be performed for fog top height computation. Winiger *et al.* (1992) as well as Reudenbach & Bendix (1998) superimpose a binary fog mask onto a digital elevation model and extract the DEM values for all marginal fog pixels. These values are interpolated over latitude and longitude for the entire image pane. Interpolated height values are then assigned to all fog pixels. The main drawbacks of this approach are a) that it can only be applied to fog areas limited by terrain, and b) the uniform interpolation of surface height for all fog areas within a scene leads to a very coarse height assignment.

4.3.2 Method Design and Implementation

The above review shows that at most two methods can be sensibly applied to fog top height determination on SEVIRI imagery: DEM interpolation and fixed lapse rate application. Based on experiences reported above, DEM interpolation is expected to yield more accurate results, so that this method is to be applied with preference where relief conditions allow for it. Otherwise lapse rate computation is to be used.

A major innovation introduced in the new cloud top height retrieval method is the use of the concept of spatially discrete cloud entities introduced in the previous section: On the assumption that on the given spatial scale the stratus top surface can be assumed to be fairly homogeneous (cf. Welch & Wielicki, 1986), the height of each cloudy pixel within the entity is derived by spatial interpolation of the height values found for the entity margin pixels. This interpolation is based on latitude, longitude and corrected cloud top temperature. With the entity-based interpolation the cloud top height assignment will be much more refined than with the scene-oriented DEM interpolation technique presented above. An overview of the new cloud top height scheme is shown in figure 4.14.

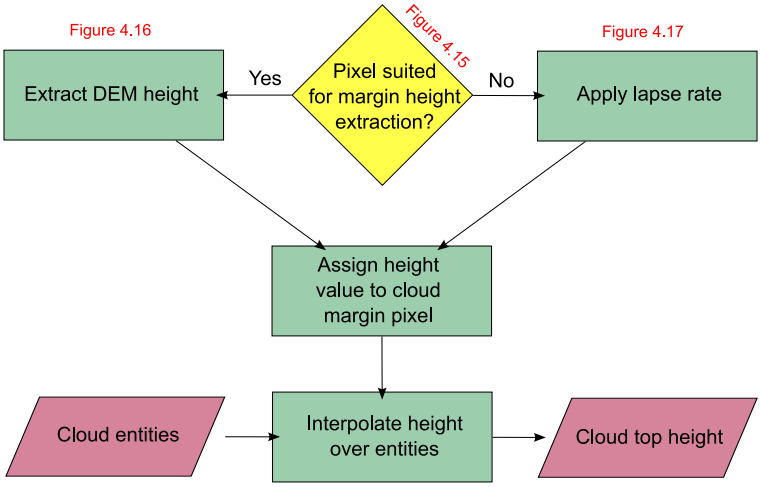

Figure 4.14: *Overview of the cloud top height scheme. For a detailed description see text.*

Accurate cloud top temperature information is a precondition for cloud top height retrieval, because parts of the scheme depend on temperature comparisons. To obtain this information, corrections for atmospheric absorption, cloud confidence and cloud transmissivity need to be performed. All these factors distort the signal recorded at the satellite sensor and their effects therefore must be removed.

The effects of atmospheric absorption are removed from the 10.8 μm blackbody temperatures based on a scheme proposed by Saunders (1988). The corrected temperature is determined as a function of $T_{10.8}$ and the viewing zenith angle. A correction factor is computed for each combination of the two and added to $T_{10.8}$.

In the partly cloudy pixels at cloud margins, cloud and surface radiances mix according to

$$I' = I_c P_c + I_s(1 - P_c) \quad [W\,m^{-2}\,sr^{-1}\,\mu m^{-1}] \tag{4.26}$$

with I' the intensity observed at the sensor, I_c $[W\,m^{-2}\,sr^{-1}\,\mu m^{-1}]$ cloud intensity, I_s $[W m^{-2} sr^{-1} \mu m^{-1}]$ surface intensity and P_c cloud confidence in the given pixel and wavelength.

P_c has been computed as a cloud confidence level in section 4.2, so that for marginal pixels, I_c can be computed as

$$I_c = \frac{I' - I_s(1 - P_c)}{P_c} \quad [W\,m^{-2}\,sr^{-1}\,\mu m^{-1}] \tag{4.27}$$

For non-opaque clouds emission of the surface below the cloud layer constitutes part of the registered radiances:

$$I' = I_s t_c + B(T_c)(1 - t_c) \quad [W\,m^{-2}\,sr^{-1}\,\mu m^{-1}] \tag{4.28}$$

with $t_c = e^{-\tau/\mu_0}$ cloud transmissivity and $B(T_c)$ $[W\,m^{-2}\,sr^{-1}\,\mu m^{-1}]$ the brightness of a blackbody at the temperature of the cloud. Transmissivity correction aims to remove I_s. The corrected cloud top temperature is computed following NAKAJIMA & NAKAJIMA (1995) and STEPHENS (1994). For detailed descriptions of the methods see the sources cited.

As stated above, ideally an interpolation of fog marginal elevation as extracted from a DEM should serve to derive cloud top height. In some cases however, fog is not limited by terrain, so that this method will fail.

A decision on whether or not DEM height extraction is possible for a given fog marginal pixel requires knowledge of its spatial situation. This information is contained in a combination of the spatially discrete cloud entities introduced above (section 4.2) and a digital elevation model.

It is assumed that the marginal pixels of each entity are only partly covered by cloud and thus represent the area where cloud patch and terrain meet. This is implicit in the design of the cloud detection scheme outlined above and corroborated by the cloud confidence level value saved for each pixel (equation 4.18). In order to be considered for margin height extraction, a cloud entity margin pixel must satisfy two criteria:

1. The surface relief at the location of the given pixel must be sufficient. This criterion is to ensure that the partly cloudy marginal pixel is not located in flat terrain. This criterion is shown on the left hand side of figure 4.15.

   In to verify this, a digital elevation model projected to MSG geometry and with a nadir resolution of 1 km is collocated with the low stratus classification. To every 1 pixel in the low stratus classification, a region of 3 by 3 pixels corresponds in the DEM. Relief (Δz) is determined from this 3 by 3 pixel area, with

   $$\Delta z(c, r) = z_{max}(c, r) - z_{min}(c, r) \tag{4.29}$$

   where $z_{max}(c, r)$ is the maximum elevation and $z_{min}(c, r)$ the minimum elevation within the marginal pixel at coordinates (c, r).

   A pixel value is included in interpolation where $\Delta z \geq 50\,m$. Visual inspection of a relief map at the given resolution shows that a good

separation of the mountainous and low-land regions of Europe can be achieved in this way.

2. The surface elevation of the adjacent clear area must be larger than under the cloud layer. While the previous test excludes flat terrain, the cloud layer may for example be located above a valley with no terrain limitation on the downslope. The direction of the relief must therefore be tested as shown on the right hand side of figure 4.15.

   To test this criterion, the surface elevation of the clear pixels directly adjacent to the cloud entity margin pixel is considered. At least one of these values must exceed the surface elevation underneath the cloud.

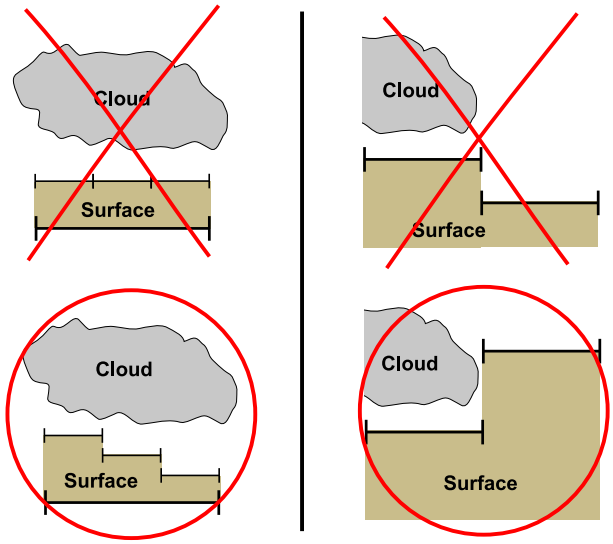

Figure 4.15: *Criteria for DEM selection. This figure shows two criteria that must be met by cloud entity margin pixels limited by terrain. A certain minimum relief needs to be present (left), and terrain must be rising from the cloud area (right).*

For a marginal pixel selected in this way, the value of the corresponding digital elevation model pixel is taken as the height value. Figure 4.16 shows the concept of this height extraction.

Where a pixel has been found unsuited for direct DEM height extraction, an environmental temperature lapse rate needs to be applied. Cloud top height $z_t(c,r)$ for each pixel with coordinates (c,r) is found according to

$$z_t(c,r) = z_s(c,r) + \frac{T_t(c,r) - T_s(c,r)}{\Gamma} \quad [m] \tag{4.30}$$

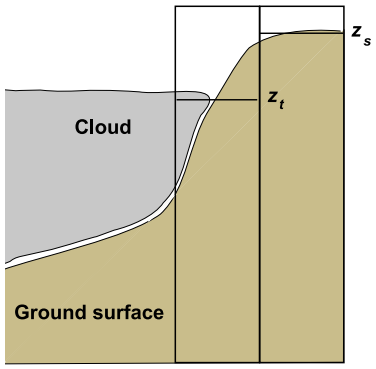

Figure 4.16: *The concept of the margin height extraction scheme. The value of the DEM pixel at the cloud margin is taken as the cloud top height z_t. Vertical lines indicate pixel borders.*

$T_t(c,r)[K]$ is the temperature of the cloud top, $T_s(c,r)[K]$ that of the surface and $\Gamma\ [Km^{-1}]$ the environmental temperature lapse rate (also see concept sketch in figure 4.17).

The height $z_t(c,r)$ obtained in equation 4.30 will be distorted if the marginal pixel considered is only partly cloud covered. In order to maximise the accuracy obtained in equation 4.30, $T_t(c,r)$ and $z_s(c,r)$ are therefore taken from the nearest cloudy pixel satisfying

$$P_c(c,r) \geq \overline{P_c(e)} - \frac{\sigma(P_c(e))}{2} \tag{4.31}$$

with $P_c(c,r)$ the cloud confidence level for each pixel at (c,r), $\overline{P_c(e)}$ the mean cloud confidence level of the given entity, and $\sigma(P_c(e))$ its standard deviation.

For radiation fog, it is assumed that after sunrise the inversion has been lifted from the ground and the environmental temperature lapse rate within the fog layer has been destabilised. For fog situations not related to surface cooling, this condition can be assumed in all cases. In this light average Γ can be presumed to be negative (i.e. decreasing temperature with increasing height). Indeed, Minnis *et al.* (1992) report an average lapse rate of -0.0071 K m^{-1} for the boundary layer and Holets & Swanson (1981) also measured rates near the moist adiabatic lapse in a fog layer.

However, while the fog top is closely associated with the inversion base genetically (cf. chapter 2), its precise height varies in time. Normally it is not precisely at the base of the inversion but slightly above it (Roach, 1995;

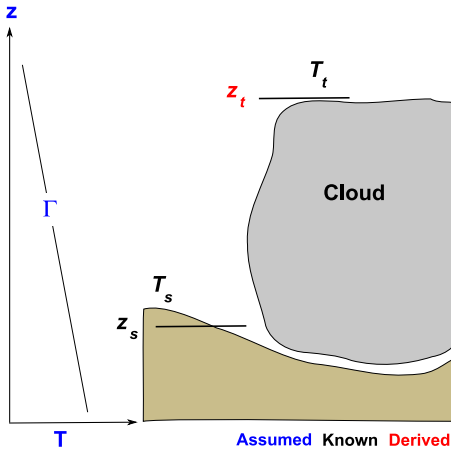

Figure 4.17: *The concept of the height determination scheme using an environmental lapse rate. z_t and z_s cloud and ground elevation respectively, T_t and T_s are the cloud and surface temperatures, Γ is the environmental temperature lapse rate. Assumed quantities are presented in blue, known figures in black and the derived quantity in red.*

Findlater, 1985; Bendix, 2004). This fact is relevant when considering the cloud top (cf. lapse rate correction in Reudenbach & Bendix, 1998).

In order to better estimate the integrated lapse rate from the ground to the cloud top for a range of situations, temperature and height differences were evaluated for margin pixels with DEM-derived height assignment. Based on these considerations and computations in 30 scenes, an average integrated environmental lapse rate of -0.0054 $\mathrm{K\,m^{-1}}$ was identified for all situations. This figure is applied in the cloud top height interpolation scheme for those entities failing the interpolation test.

As a rough assessment of method plausibility, the computed cloud top heights were compared with series of radiosonde measurements. Figure 4.18 shows a selection of temperature and humidity radio soundings for 1200 universal time co-ordinated (UTC), 16 January 2005 throughout the study region. While radiosonde measurements offer no precise data on cloud top height, a possible range for this parameter can be read from vertical temperature and humidity profiles. The inversion base is found where temperature begins increasing with height. The cloud base is located somewhere near this point, and generally linked with decreasing levels of relative humidity. The satellite-derived cloud top heights shown in figure 4.18 generally fall within this range around a temperature inversion base. The cloud top height retrieval results are therefore accepted as plausible.

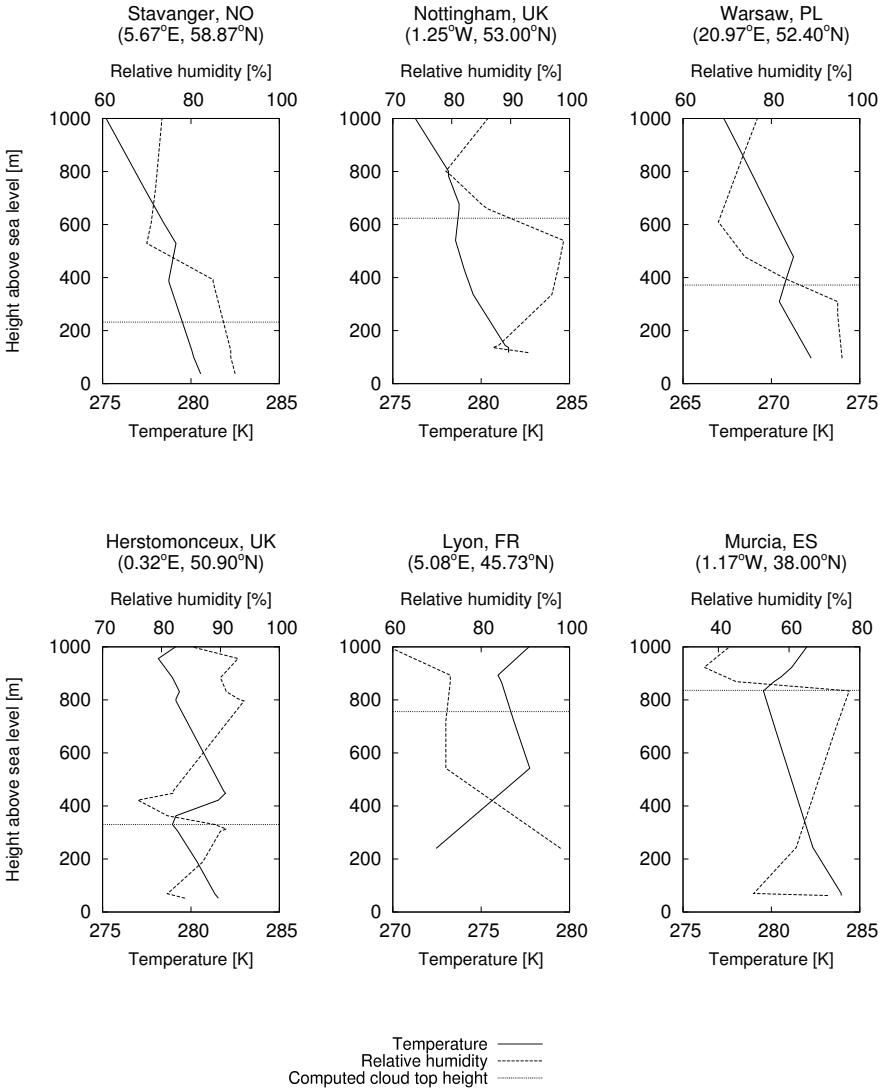

Figure 4.18: *Radio soundings of temperature and humidity for 1200 UTC, 16 January 2005, with cloud top heights computed from satellite imagery.*

4.4 Cloud Geometrical Thickness

The retrieval of cloud thickness completes the newly developed methodology (see figure 2.4). Together with cloud height information computed according to the method introduced in the previous section, cloud thickness can be used to distinguish between ground fog and elevated fog (see figure 2.3).

Cloud thickness can be addressed in a variety of ways, according to the focus of a study. Therefore, this section sets out with a consideration of cloud thickness concepts and their manifestation in satellite-measured radiances. Then, previous approaches to the problem of cloud thickness retrieval are presented. They are discussed in the light of cloud thickness concepts with a clear identification of shortcomings. Based on these insights, the development of the new method is then described in detail.

4.4.1 Physical Basis

Concepts of Cloud Thickness

The thickness of a cloud can be defined either in a geometrical or in an optical sense. Geometrically, cloud thickness Δ_z is the difference of cloud boundary heights, i.e.

$$\Delta_z = z_t - z_b \quad [m] \tag{4.32}$$

with $z_t\,[m]$ cloud top and $z_b\,[m]$ cloud base height. The cloud boundaries can be physically defined as those points in the vertical profile where cloud liquid water content ρ_c reaches 0.

Cloud extent defined in this way is related to optical cloud delimitation in that it is the path along which cloud optical properties are integrated. Cloud optical thickness (or depth, τ) has already been introduced in section 4.1.2. It is the integration of extinction over cloud geometrical thickness.

Based on equations 4.9 and 4.10, optical depth and cloud geometrical thickness can be related as follows:

$$\Delta_z = \tau / \overline{\beta_e} \quad [m] \tag{4.33}$$

This means that τ and Δ_z are only linked via the average extinction coefficient ($\overline{\beta_e}\,[m^{-1}]$). Depending on the vertical stratification of β_e, a cloud with a fixed vertical extent is ambiguous concerning τ. The same ambiguity applies to liquid water path $W\,[g\,m^{-2}]$, related to Δ_z via average liquid water content $\overline{\rho_c}\,[g\,m^{-3}]$ by

$$\Delta_z = W/\overline{\rho_c} \quad [m] \tag{4.34}$$

In section 4.1.2 it has been shown that W and τ directly explain the satellite signal. β_e and ρ_c however do not affect the signal and cannot be retrieved. Due to the relationships revealed in equations 4.33 and 4.34, cloud geometrical thickness therefore cannot be deduced directly from the intensities received at the satellite sensor.

Although geometrical information thus is not the only determinant of W and τ, knowledge of these bulk parameters would nonetheless allow for insights into the vertical buildup of a cloud. As they are directly linked to radiation received at the satellite sensor (cf. section 4.1.2), the retrieval of some such integrated cloud parameters from satellite data is possible. In the following, an overview of parameters and retrieval techniques is given.

Integrated Cloud Parameters and Their Retrieval

The transport of radiation through a cloud has been briefly discussed in section 4.1.2. Solar reflectance at visible and near to middle infrared wavelengths is determined by cloud optical depth and droplet effective radius and thus also linked to liquid water path.

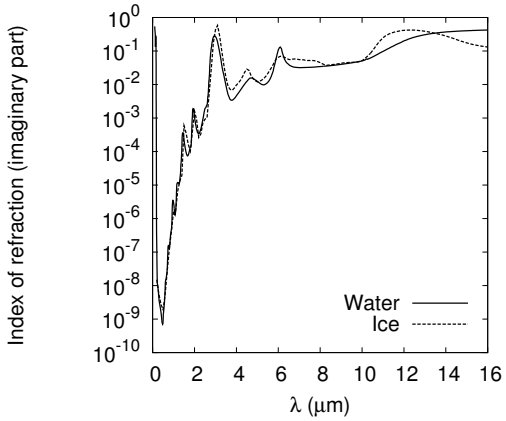

Figure 4.19: *Imaginary part of the refractive index (absorption) for liquid water and ice. Data according to* Segelstein *(1981, water) and* Warren *(1984, ice).*

At visible wavelengths (up to about 1.2 μm) no radiation is absorbed and cloud reflectance is entirely governed by cloud optical depth. At near and midwave infrared wavelengths, the absorption increases sharply. The absorption component of the interaction of matter with radiation is called

the imaginary part of the refractive index. This is depicted in figure 4.19 for the relevant wavelength region. Thus, the signal is impacted on by particle size: Absorption increases with droplet size, reducing the overall signal. However, the level of absorption also depends on the optical depth of a cloud at these wavelengths, up to the asymptotic limit, beyond which only droplet size matters. This limit is reached earlier at longer MIR wavelengths with increasing absorption efficiency. Figure 4.20 highlights the dependence of VIS and MIR reflectances on both parameters.

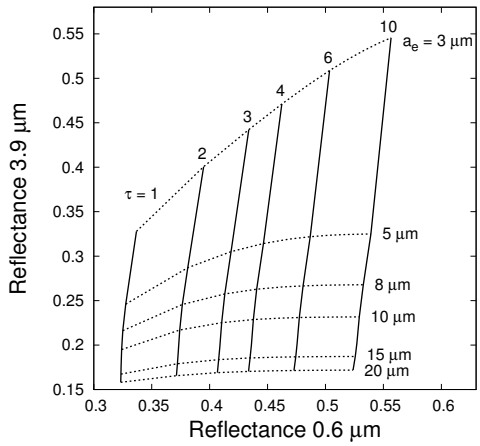

Figure 4.20: *The dependence of middle infrared (3.9 µm) and visible range (0.6 µm) reflectances on cloud optical depth (τ) and droplet effective radius (a_e). 3.9 µm reflectance increases with decreasing droplet sizes, and 0.6 µm reflectance mostly rises with cloud optical depth.*

This principle can be exploited in satellite remote sensing to retrieve cloud optical depth and droplet effective radius, and thus liquid water path (equation 4.13). A number of these solar reflectance methods have been developed and presented (e.g. Twomey & Cocks, 1982, 1989; King, 1987; Nakajima & King, 1990; Nakajima *et al.*, 1991).

For this study, the approach developed by Nakajima & Nakajima (1995) and expanded by Kawamoto *et al.* (2001) was chosen. This technique is well-suited for application in a study dealing with fog, as it uses the 3.9 µm band as the absorbing channel and thus allows for the retrieval of thin clouds. The method inverts tabulated reflectance and angle values computed with the RSTAR-5b radiative transfer code (Nakajima & Tanaka, 1986). In an iterative procedure the observed radiances are fitted to the exact values contained in these lookup tables (LUTs). While computationally slightly more expensive than other schemes, the algorithm has been shown

to yield very accurate results (Nakajima & Nakajima, 1995; Nauss *et al.*, 2005).

The scheme was originally developed for NOAA AVHRR; a look-up table (LUT) adapted to MSG SEVIRI was computed by Nauss *et al.* (2004). The entire procedure has been implemented in the MetProd module of the processing framework (see chapter 3), so that the parameters a_e, τ and W are available for use in the fog detection scheme.

4.4.2 Approaches to Cloud Geometry Retrieval

Bulk cloud optical properties are very well represented by droplet effective radius and optical depth, regardless of the details of the droplet size distribution and vertical stratification (Hu & Stamnes, 1993). Nonetheless, as shown above, the consideration of cloud geometry requires some knowledge of, or at least assumptions on, the vertical cloud profile or at least its average composition. A number of approaches attempting just this have been put forth. These will be reviewed in the following paragraphs along with short assessments of their strengths and weaknesses.

Simple Parameterisations

The simplest kind of approach to cloud thickness computation relies on parameterisations of one or more parameters related to thickness. These methods usually yield only very rough approximations.

Ellrod (2002) applies a threshold to the difference of GOES infrared brightness temperatures between clear and cloudy pixels to identify cloud base heights <1000 ft ($\approx$ 300 m). This approach relies on the assumptions that a) a low temperature difference indicates low cloud top height, and b) all clouds identified are of sufficient thickness for their bases to reach 1000 ft. While the first of these assumptions will be roughly accurate in most situations, the second condition is not solid enough for application in the context of the present study, where more precise cloud geometry information is needed.

A range of schemes implicitly or explicitly relate cloud optical bulk parameters to cloud geometrical thickness. The brightness temperature difference between 10.8 and 3.9 μm can be linked to cloud optical depth (as shown in figure 2.1). Based on this relationship, and assuming a constant vertical stratification, the brightness temperature difference is used by Ellrod (1995) to estimate fog geometrical thickness from GOES imagery. This method provides only very rough approximations to cloud thickness, as it

only considers optical depth (by proxy). The lack of information on cloud buildup significantly impacts on the accuracy of this method.

Some authors present methods to estimate the average liquid water content $\overline{\rho_c}$ of a cloud. Together with a computed liquid water path value, cloud thickness can then be found according to equation 4.34. Stephens (1979), Hess *et al.* (1998) and Korolev *et al.* (2001) present such liquid water content values for a range of different cloud types (0.05 to 0.30 gm^{-3} for stratus); Nakajima & Nakajima (1995) also use a fixed value (0.154 gm^{-3}) for stratus cloud thickness retrieval. Hutchison (2002) uses values of 0.20 to 0.45 gm^{-3} but remarks that these are only applicable to thin homogeneous clouds. The obvious problem of this type of method is the wide range of possible values of $\overline{\rho_c}$. In the examples cited alone, a variation by a factor of 9 is found between the smallest and largest estimates.

Other authors relate $\overline{\rho_c}$ to temperature (Gultepe & Isaac, 1997; Liou, 2002) and droplet effective radius (McFarlane *et al.*, 1995; Martin *et al.*, 1994). Although these approximations may be useful for local application, vertical variation within a cloud is only insufficiently represented so that $\overline{\rho_c}$ found in this way is no sound basis for cloud thickness determination.

Adiabatic Approximations

Several authors try to compensate the lack of vertical cloud information by assuming an adiabatic cloud profile. In these situations liquid water content is expected to increase monotonically with height over cloud base. The adiabatic assumption gives the liquid water mixing ratio m_l (mass of liquid water per mass of dry air) at a height z within the cloud as

$$m_l(z) = m_v(z_b) - m_v(z) \quad [g\,kg^{-1}] \tag{4.35}$$

with $m_v\,[g\,kg^{-1}]$ the water vapour mixing ratio and $z_b\,[m]$ cloud base height. A parcel of moist air rising from underneath the cloud reaches saturation at the cloud base z_b. On its way up within the cloud, no moisture is removed from or added to the parcel.

For clouds with such an adiabatic profile, Brenguier *et al.* (2000) state a relationship of liquid water path W with the square of cloud thickness, based on considerations presented by Boers & Mitchell (1994):

$$W \propto (\Delta_z)^2 \tag{4.36}$$

This implies that for adiabatic clouds, thickness can be approximated using liquid water path. In absence of liquid water path information, Minnis *et al.* (1992) use cloud optical thickness as a proxy value and fit its

distribution to observed cloud thickness data. By least-squares regression they obtain

$$\Delta_z = -45.6 + 84.3\tau^{0.5} \quad [m] \tag{4.37}$$

For the marine stratocumulus clouds this parameterisation is based on, Minnis *et al.* (1992) obtain a correlation coefficient of 0.64 and a root mean square error (RMSE) of 61.6 m for classification skill. Based on the same data set, Heidinger & Stephens (2000) fit cloud thickness as

$$\Delta_z = 45\tau^{2/3} \quad [m] \tag{4.38}$$

While these parameterisations have a certain validity for approximating cloud systems closely resembling the ones they were fitted to, their transferability has to be questioned (as shown in Bendix *et al.*, 2005). The main problem with these approaches using only optical depth as a predictor is their ambiguity. A low optical thickness is interpreted as a low geometrical thickness, while it may as well indicate a low droplet sizes (e.g. in a thick cloud with little pollution). As shown in equation 4.13, the relationship between optical depth and liquid water path is via droplet effective radius. The use of τ alone as a proxy for W therefore has to be questioned.

Other authors therefore further explore the adiabatic cloud model with respect to liquid water content and liquid water path. In an adiabatic cloud, (adiabatic) liquid water concentration ρ_c^{ad} and height z above cloud base z_b are related linearly:

$$\rho_c^{ad}(z) = C_w(z - z_b) \quad [g\,m^{-3}] \tag{4.39}$$

(Brenguier *et al.*, 2000). $C_w\,[g\,m^{-3}\,m^{-1}]$ is the moist adiabatic condensate coefficient and describes the rate of change of liquid water with height. Its value depends on temperature and pressure. At sea level, it ranges from 1 * 10^{-3} to 2.5 * 10^{-3} for temperatures from 0 to 40°C. In the lower atmosphere (at high pressure levels) the variation of C_w with height is limited so that for thin low-level clouds it can be assumed to be almost constant (Brenguier, 1991). In these conditions, the adiabatic cloud liquid water path is given by

$$W^{ad} = \frac{C_w \Delta_z^2}{2} \quad [g\,m^{-2}] \tag{4.40}$$

(Brenguier *et al.*, 2000)

On the assumption that a liquid water path retrieved from satellite data as presented above represents an adiabatic cloud, Δ_z can be computed using this relationship. Iwabuchi & Hayasaka (2003) apply this insight to the

retrieval of boundary layer cloud geometrical thickness. An evaluation by Bendix *et al.* (2005) however has shown this technique to perform very poorly for low stratiform clouds. This implies that the adiabatic assumption is incorrect for this type of cloud.

Some of the parameterisations presented above are shown in figure 4.21 as a function of cloud optical depth. It is apparent that the parameterisations by Minnis *et al.* (1992) and Heidinger & Stephens (2000) are insensitive to changes in droplet effective radius. Their values roughly correspond to the Brenguier approximation with an effective radius of 10 μm (not shown for visual clarity). The simple parameterisations with a fixed liquid water content show the largest deviation with effective radius at large optical depths.

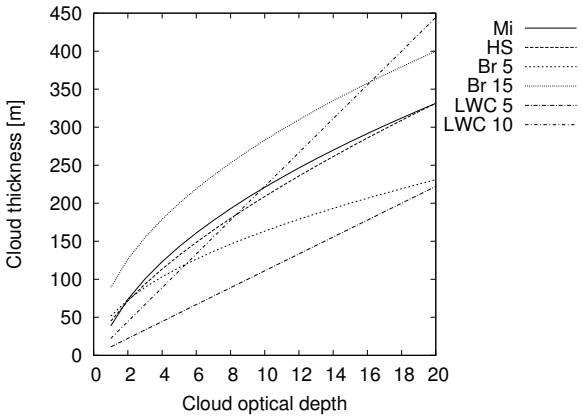

Figure 4.21: *Geometrical thickness retrieved using a range of approaches presented in the text. Mi:* Minnis et al. *(1992), HS:* Heidinger & Stephens *(2000), Br:* Brenguier et al. *(2000) using a cloud base temperature of 273 K and the droplet effective radius indicated (5 and 15), LWC: using a fixed liquid water content of 0.25 gm^{-3} and the droplet effective radius indicated.*

Pseudosounding

A third strand of approaches designed to retrieve cloud geometrical thickness makes use of the asymptotic absorption limits in the middle infrared. In this range, photon absorption increases with wavelength. This means that a radiation originating from a cloud is more likely to be absorbed at longer MIR wavelengths, so that the information contained in satellite-received radiation represents increasingly shallow layers at cloud top (Platnick, 2000).

Satellite-based retrievals of cloud optical properties generally foot on a homogeneous plane-parallel cloud (vertically uniform plane-parallel) model. This concept assumes a cloud with no vertical (and horizontal) variation. Ideally, the microphysical parameters retrieved at different MIR wavelengths should therefore be identical. In a real cloud droplet effective radius varies with height though. Therefore, given the differences in MIR penetration depths, conclusions regarding the vertical profile of the cloud are possible (Bendix *et al.*, 2005). This technique is referred to as 'pseudosounding'.

Unfortunately, properties observed at different MIR wavelengths represent the cloud at different optical rather than geometrical depths (Chang & Li, 2003). Therefore, no information on cloud geometrical thickness can be derived from multiple-wavelength MIR measurements alone.

The only way to resolve a geometrical cloud profile from different MIR optical penetration depths is by fitting the distribution to an assumed vertical cloud profile. This is done by various authors using adding-and-doubling radiative transfer models (e.g. Chang & Li, 2002a,b, 2003; Platnick, 2000; Schüller *et al.*, 2005). Adding-doubling models consist of various vertically integrated layers. Simulations are performed for each layer, and integrated cloud parameters are computed from the ensemble of layers. The vertical profiles modelled by the cited authors mostly use adiabatic assumptions.

While this type of technique is very well rooted in cloud radiative physics and may be expected to produce results of good accuracy, its applicability to fog thickness retrieval using MSG SEVIRI is limited by the channels available on this system:

The SEVIRI instrument has middle infrared bands at 1.6 and 3.9 μm. At the less absorbing band at 1.6 μm, radiation penetrates much deeper into the cloud, so that in principle, profile information could be retrieved. However, for optical depths smaller than about 15, the cloud will be fully penetrated at 1.6 μm and thus no significant vertical signature will be found (Platnick, 2000). This inhibits a useful retrieval of droplet effective radius at this wavelength for thin clouds. Pseudosounding of cloud thickness therefore is not possible on MSG SEVIRI.

4.4.3 Vertical Stratification of Fog and Very Low Stratiform Clouds

While the more sophisticated approaches presented above generally assume linear profiles of cloud microphysical parameters, the buildup of real clouds is more complex. The adiabatic increase in liquid water content with height is a rare exception; most clouds have distinctly sub-adiabatic profiles, i.e.

water content increases more slowly. Indeed, data presented by BRENGUIER *et al.* (2003) clearly shows that an adiabatic profile of ρ_c systematically overestimates the real liquid water path. The development of a more realistic cloud thickness retrieval technique therefore requires a closer consideration of vertical water distribution in fog.

As a measure of departure from the adiabatic situation, BETTS (1982) introduced the in-cloud mixing parameter

$$\beta = \frac{dp_s}{dp} \tag{4.41}$$

(BETTS, 1982, 1985), with p_s the saturation pressure (i.e. the point where a parcel just reaches saturation) at pressure level p. For a well-mixed layer, the saturation point is constant, yielding $\beta = 0$ for adiabatic situations (saturation is reached at cloud base). For sub-adiabatic clouds, β typically takes values $0 \leq \beta < 1$. A departure from $\beta = 0$ impacts on liquid water concentration:

$$m_l(z) = (1 - \beta) m_l^{ad}(z) \quad [g\,kg^{-1}] \tag{4.42}$$

(BOERS & MITCHELL, 1994). $m_l(z)$ is the liquid water mixing ratio at height z, and $m_l^{ad}(z)$ [g moisture / kg dry air] the adiabatic liquid water mixing ratio at the same level. Thus, for small β, water mixing ratio remains close to adiabatic; when β approaches 1, liquid water falls to 0.

In a number of studies, average mixing parameters between 0.3 and 0.4 have been identified for boundary layer stratocumulus clouds, and slightly lower values for stratus (BOERS & BETTS, 1988; BOERS & MITCHELL, 1994; BETTS & BOERS, 1990; BOERS *et al.*, 1991; SLINGO *et al.*, 1982).

For the purpose of cloud geometrical thickness determination in the context of the present study, the processes in vertical cloud development deserve closer consideration. In particular, the processes of cloud formation and development need to be reconsidered in this light.

Generally, droplets in stratiform clouds form by condensation rather than by coalescence. This also holds true for radiation fog. Therefore, turbulent mixing is of minor importance in fog formation. The formation of radiation fog presents a special situation since it occurs at the ground surface. Nonetheless, the dominant processes effecting liquid water distribution within a boundary layer stratiform cloud are very similar.

As a special case, radiation fog development will be considered in the following paragraphs. Where applicable, parallels to other very low stratus clouds will be shown. The formation and development of radiation fog involves a fine balance of radiative cooling and turbulent mixing of air. It can

be split into three main processes, each with a distinctive impact on water distribution within the cloud. These processes are presented in overview in figure 4.22. Development stages in this figure are labelled in agreement with the following paragraphs.

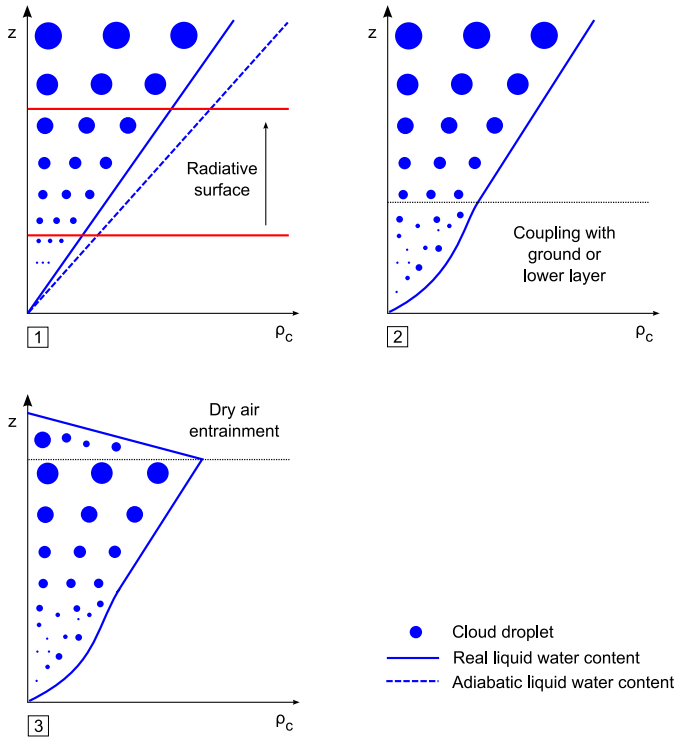

Figure 4.22: *Processes in fog and very low stratus development. For a detailed description see text; development stages are numbered like the corresponding paragraphs.*

1. In the initial phases of the radiation fog life cycle, radiative cooling takes place at the ground surface. At this stage, slight turbulence is needed to spread the cooling effect to and within the air near the ground. As the dew temperature is reached in this layer, condensation sets in. Initially, the condensate is deposited on the ground as dew, due to the prevailing turbulence. The further development of fog in this situation depends on comparatively calm conditions, i.e. the initial turbulence must subside so the water loss due to dew settling ceases (Brown & Roach, 1976; Roach, 1995). Only very slight turbulence (up to $0.5\,\mathrm{m\,s^{-1}}$) still occurs at this stage (Gerber, 1981). Radiative cooling then leads to thickening and stabilisation of the fog layer as

the cooling surface moves upwards.

Liquid water content in the cloud rises with height in the fog layer (Pruppacher & Klett, 1997). Because there is little vertical motion within the cloud, the droplet number concentration remains almost constant with height. Increasing liquid water content manifests itself in increasing droplet size (Brenguier *et al.*, 2000; Chang & Li, 2002b).

The liquid water profile at this stage is sub-adiabatic by tendency, as shown in the left hand pane of figure 4.22.

2. At ground level, heat conduction from the soil continues after the radiatively cooled surface has shifted upwards, resulting in heat and moisture convection into the lower fog layers (Roach, 1995). Mixing thus sets in again at the fog base.

   For all boundary layer clouds, with or without ground contact, layer coupling, i.e. exchange between layers, is generally better (i.e. β smaller) in the presence of strong and low inversions (Durand & Bourcy, 2001). Also, a good coupling of the lowermost cloud layer to the air layer near the surface (where not in contact with the ground) reduces local in-cloud β to values near 0. Water supply from below the cloud is steady and mixing conditions near the cloud base are close to adiabatic. Meyer & Rao (1999) use $\beta = 0.1$ for this region.

   This influence of the ground or the layer below the cloud is shown in the second pane of figure 4.22.

3. With growing thickness, mixing slowly sets in again. Radiative cooling of the upper fog layers leads to convective turbulence within the fog (Caughey *et al.*, 1982). This process has two main effects: On the one hand the resulting upwards movements of moisture within the cloud enhance the increase of water content with height (Oliver *et al.*, 1978; Manton, 1983; Walker, 2003).

   On the other hand, water content near the cloud top is depleted due to dry air entrainment (Roach, 1995). The cloud top layer is quickly decoupled from the lower layers; the monotonical rise in liquid water content thus stops just below the cloud top. Dry air from the surroundings is mixed into the cloud leading to a quick decline in droplet size and water content (Boers & Mitchell, 1994; Driedonks & Duynkerke, 1989; Roach *et al.*, 1982; Brown & Roach, 1976; Hoffmann & Roth, 1989). This point is usually reached at about 80–90 % of cloud height (Wieprecht *et al.*, 2005).

For very low stratus clouds other than radiation fog, cloud development obviously does not start at the ground, so that initial cloud formation follows a different pattern. However, the parallels in cloud development and thus stratification are extensive. As in radiation fog, turbulence is of minor importance or largely absent in the formation process. Coupling with the layer below the cloud and cloud top entrainment take place in elevated very low stratus clouds as well, so that the resulting cloud profile is very similar to the one described above and depicted in figure 4.22.

The idealised profile described in the above paragraphs is closely matched by observations of fog and very low stratus. Detailed descriptions of the processes and corresponding measurements in fog and very low stratus are also given in a large number of studies (e.g. Caughey *et al.*, 1982; Hayasaka *et al.*, 1995; Genio & Wolf, 2000; Best, 1951; Hess *et al.*, 1998; Miles *et al.*, 2000; Heintzenberg *et al.*, 1998; Fitzjarrald & Lala, 1989; Platnick, 2000).

4.4.4 Development and Implementation of a Cloud Water Model

As shown above, the typical boundary layer cloud profile is far from the adiabatic or other linear ideals assumed in the cloud thickness retrieval approaches presented above. Therefore, the development of a new method for the determination of cloud base height with a specific focus on boundary layer stratiform clouds needed to be developed.

The new method was designed to closely follow the cloud profile and process considerations presented above. To this end, a numerical model of cloud liquid water change with height within a given cloud layer was developed.

Figure 4.23 gives an overview of the new scheme. Liquid water path and cloud top height are known for a given pixel (their retrieval has been discussed above). Using the new model, cloud water distribution is simulated for clouds with the known cloud top height and assumed cloud base heights. This procedure is repeated iteratively until liquid water path of the modelled cloud agrees with the liquid water path retrieved from satellite imagery. The corresponding cloud base height is accepted as the valid assumption for the given pixel.

The main challenge in model development is to accurately quantify the deviation from the adiabatic profile, i.e. the mixing parameter β. A number of values for β have been reported by various authors (see above). However, in the light of the very low stratus development processes discussed above,

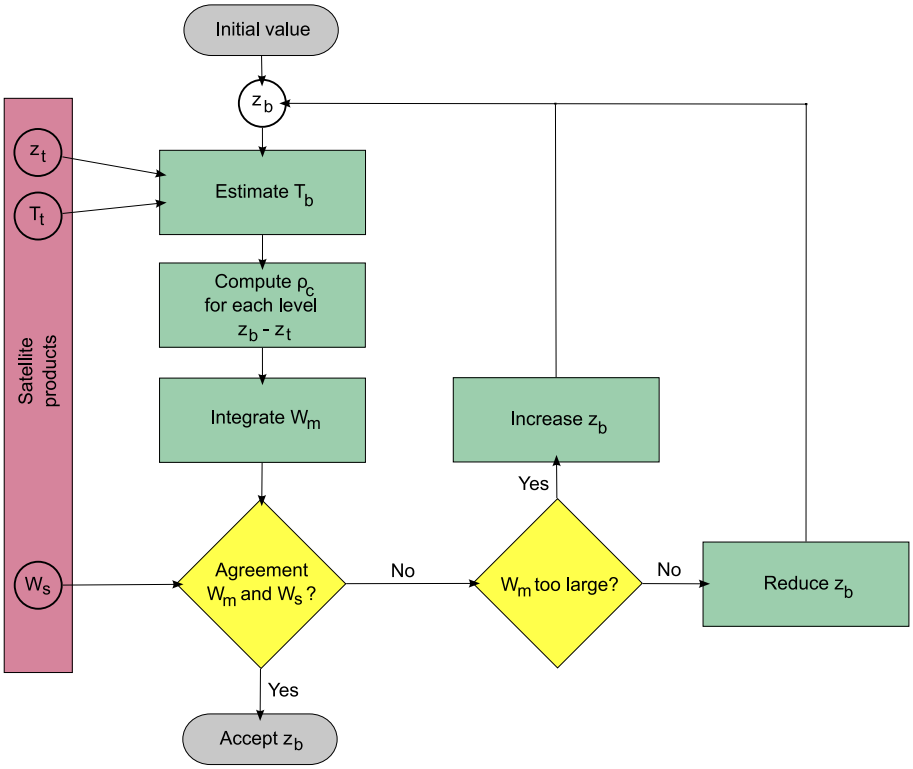

Figure 4.23: *Overview of the cloud base height retrieval scheme. See text for an explanation of variables and procedure.*

a more detailed consideration of the cloud profile is warranted. Therefore, in the newly developed model, the cloud is considered as consisting of three layers with different values of β. For each cloud layer from an assumed cloud base to the known cloud top, the adiabatic liquid water content is computed and then modified according to β assumed for the layer:

$$\rho_c(z) = (1 - \beta)\rho_a m_l(z) \quad [g\,m^{-3}] \tag{4.43}$$

with ρ_a the density of air and $m_l(z)$ $[g\,kg^{-1}]$ liquid water mixing ratio at height z (equation 4.35). $m_l(z)$ is a function of pressure and temperature at z.

The parameterisation of β for each layer closely follows the discussion of cloud processes presented above. The cloud is segmented into three layers, cloud top (entrainment), cloud base (coupling with ground or surface layer) and the region in between. The concepts introduced in the following paragraphs are visualised in figure 4.24.

- In the central region of the cloud (between the base and top layers), a fixed value of β is applied. It has been stated above that coupling of cloud layers is greater the closer a cloud is to the ground. β is therefore scaled from 0 to 0.3 according to cloud top height above ground, with

  $$\beta = \frac{0.3 z_t}{1000} \tag{4.44}$$

  In this way, a cloud with top height $z_t = 1000\,m$ will be assigned a β of 0.3, a cloud with $z_t = 500\,m$ 0.15. This figure is then fixed for the central cloud region.

- On the assumption that moisture is fed into the cloud from below (see above), β must be smaller in the lower part of the cloud and gradually increase towards the central region. Within the lowermost 75 m of the cloud β_l (β of the lowermost layer) is scaled linearly from 0 to β of the central region, increasing upwards. This marks the transition from an almost adiabatic increase in ρ_c to a layer with worse coupling.

- Near cloud top, dry air entrainment quickly reduces ρ_c to zero. To account for this in the model, where the uppermost 50 m are reached (Wieprecht *et al.*, 2005), liquid water linearly drops to 0 up to the cloud top.

This configuration was derived by cloud profile and process descriptions in a multitude of papers (see previous section). The sensitivity of the thresh-

olds will be explored below (figure 4.27) for one profile observation. The concept is shown in overview in figure 4.24.

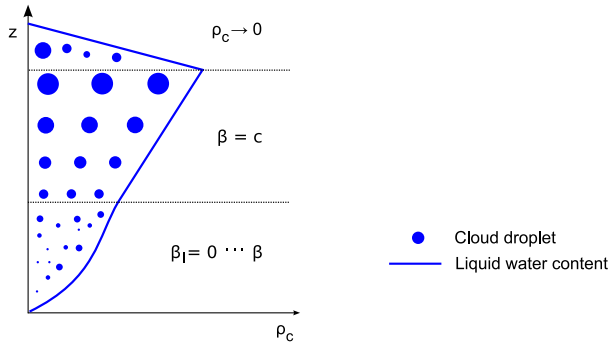

Figure 4.24: *The cloud profile parameterisation used for cloud liquid water path computation. The figure shows the development of mixing ratio β and liquid water content ρ_c with height in the cloud. Cloud layers are the same as those shown in figure 4.22. For a detailed description see text.*

The integration of ρ_c over the thickness of the cloud yields modelled liquid water path W_m. This bulk parameter is also known from satellite retrievals (W_s), so that model and measured parameters can be compared. This is done in an iterative procedure in which cloud base is shifted until the best match is found. In a first step, cloud bases at 300 m below ground and just below the known cloud top are assumed. They are iteratively raised and lowered to close in on the measured liquid water path (see figure 4.23).

Since the satellite-derived quantity of W_s is retrieved at a wavelength of 3.9 μm with a small photon penetration depth into the cloud (see above), its value is not representative of the entire cloud. Platnick (2000) quantified the relationship between observed and retrieved W_s for several cloud optical depths. These relationships are used to correct satellite W_s before fitting the model.

While above cloud base height was generally defined as the point where cloud liquid water content drops to 0, the definition of fog requires a certain level of extinction, i.e. a visibility less than 1000 m. Therefore, visibility is computed for each level as well. Visibility is derived from extinction by Koschmieder's law for a contrast threshold of 2 % according to equation 4.7. Extinction is given by

$$\beta_e = \frac{3\rho_c}{2a_e\rho_l} \quad [m^{-1}] \tag{4.45}$$

with ρ_l the density of liquid water [g m^{-3}]. Droplet effective radius a_e [μm]

for each level is computed on the assumptions that a_e retrieved at 3.9 μm is the cloud top value, cloud base a_e is at 1 μm and the intermediate values are scaled linearly in between.

The lowest height with visibility <1000 m within the fitted profile is identified as the base of the fog layer.

The modelled cloud base height very much depends on the validity of all the assumptions and parameterisations. In order to express this uncertainty, a ground fog confidence level is computed. Technically, ground fog is likely to occur when the computed cloud base is at or below the surface elevation in a given location. This elevation is taken from a digital elevation model. Ground fog confidence levels are scaled on an interval from 0 to 1. A confidence level of 1 is assigned to situations where half of the simulated cloud or more lies below the ground surface, i.e. $z_t - z_b \geq 2(z_t - z_s)$ where z_t is the cloud top height, z_b cloud base height and z_s surface elevation. A confidence level of 0 is given to situations where at least one cloud thickness remains between cloud base and the ground, i.e. $z_t - z_s \geq 2(z_t - z_b)$. The computation of the ground fog confidence level P_g for any given z_b follows

$$P_g = 0.5 - 0.72 \ln \left(\frac{z_t - z_s}{z_t - z_b} \right) \tag{4.46}$$

A sensitivity study of the model expectedly reveals a strong dependency of simulated cloud thickness on liquid water path and cloud top temperature. This relationship is shown in figure 4.25. The thickness of warm clouds changes almost linearly with liquid water path; the effect of small temperature changes is more enhanced at lower cloud top temperature levels. Generally, at constant thickness a warm cloud will have a higher liquid water path than a cold cloud. This is very much in accordance with physical expectations (also see chapter 2).

In order to assess model plausibility, a few profiles of microphysical properties in stratus layers have been extracted from the literature and compared with model output. They are presented in figures 4.26, 4.28 and 4.29. The best fit modelled profile is shown in each figure, along with an adiabatic profile and a horizontal line indicating cloud base height computed from equation 4.40 ('Brenguier approach').

Figure 4.26 shows the liquid water content of a low stratiform cloud reported by Slingo & Schrecker (1982). The modelled profile very well approximates the cloud dimensions, while an adiabatic profile and the Brenguier parameterisation both overestimate cloud base height. This is a typical example of a sub-adiabatic low stratus cloud profile as discussed above. Ground fog confidence is at $P_g = 0.00$. This means that the new scheme

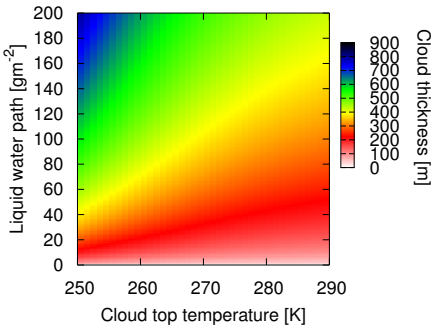

Figure 4.25: *Dependence of simulated cloud thickness on liquid water path and cloud top temperature, at a constant cloud top height of 500 m above ground. Discussion see text.*

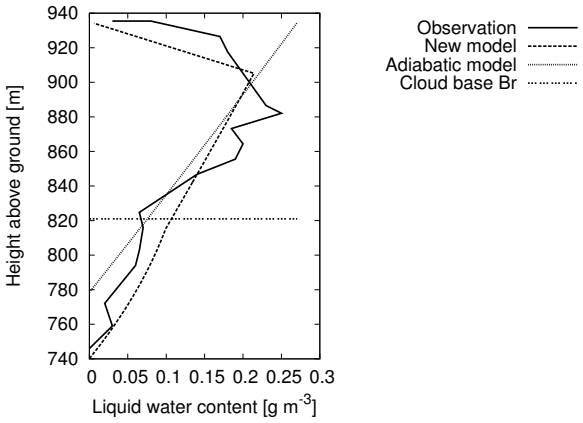

Figure 4.26: *A low stratus cloud profile observed by* Slingo et al. *(1982), with a cloud base of 745 m. The profile is shown together with liquid water content modelled using an adiabatic model, the new sub-adiabatic model, and cloud base height retrieved based on the parameterisation by Brenguier (equation 4.40, 'Cloud base Br'). For a listing of measurements and modelled values see 4.2.*

classified this cloud as not touching the ground at maximum confidence.

This profile was also used to explore the sensitivity of cloud base prediction accuracy to the thresholds of β and cloud base and top transition. Figure 4.27 shows the deviation of the modelled profile from the measured cloud thickness as a function of the chosen value of β, the height of the cloud base transition zone and the cloud top zone. It can be seen that with increasing β cloud base height is underestimated. This is because at a larger β, the same liquid water path fills a thicker cloud. Increasing the height of the cloud base transition zone, i.e. the zone in which β_l is scaled from 0 to β generally effects an overestimation of cloud base height. When the height of the cloud top transition zone, i.e. the zone where cloud liquid water content drops to 0, is increased, cloud base height is underestimated by tendency. Overall, these figures show that the thresholds deduced from literature review ($\beta = 0.3$, cloud base transition = 75 m, cloud top transition = 50 m) very appropriately approximate the profile considered.

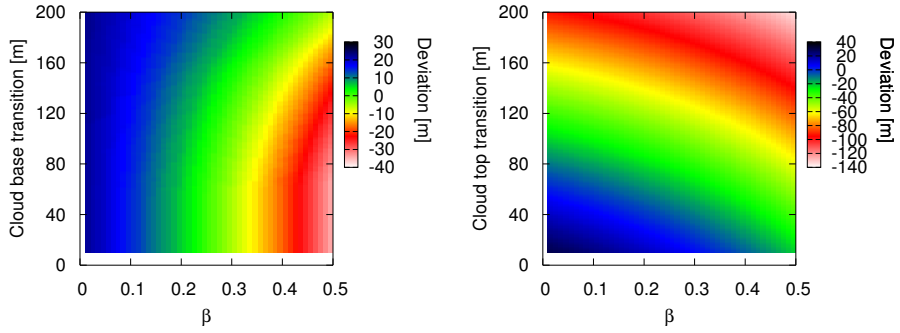

Figure 4.27: *Deviation of the computed cloud base height from observed cloud base height in metres as a function of β, cloud base transition and cloud top transition. For a constant β, increasing height of the cloud base transition zone leads to increasing overestimation of cloud base (left hand panel). The dependence on β is very strong. Increasing the height of the cloud top transition zone leads to enhanced underestimation of cloud base.*

The only description of a ground fog profile found in the literature is given in Pinnick *et al.* (1978). Unfortunately, these authors only measured the profile up to a height of 155 m above ground, while their measurements clearly indicate that the cloud top is not yet reached at this height (liquid water content $\gg 0$). The remaining part of the profile is thus estimated as shown in figure 4.28. The Brenguier parameterisation underestimates cloud thickness and thus does not identify it as a cloud with ground contact. On the other hand, both models overestimate the profile, even the adiabatic

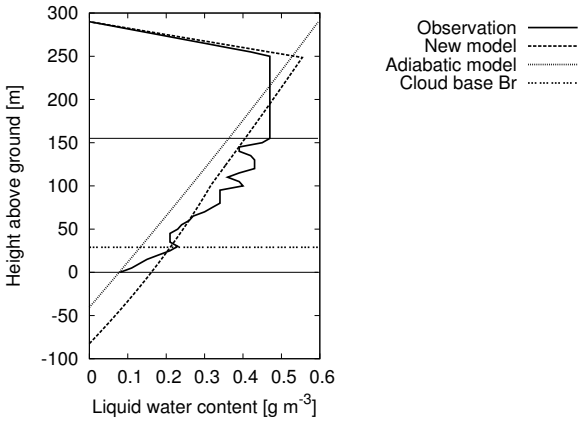

Figure 4.28: *A ground fog profile taken from* PINNICK et al. *(1978). For explanations cf. figure 4.26. The thin horizontal lines indicate the upper and lower limits of the original data. For a listing of measurements and modelled values see 4.2.*

model. This is due to the fact that there is no real cloud base. In order to understand the model thickness overestimation it needs to be considered that the fog profile starts with a liquid water content of almost $0.1\,\mathrm{gm}^{-3}$ at the surface, which is only possible in situations with cloud ground contact. The models however assume a cloud base water content of 0, so that naturally the modelled cloud base must be below the surface. For this example the overestimation of the thickness is not a problem as ground contact is properly detected. A sound ground fog confidence of $P_g = 0.70$ is computed for this profile based on equation 4.46.

A more critical situation arises when this fog layer is lifted from the ground. The process of fog 'lifting' involves a significant depletion of cloud liquid water content. Beginning in the lowermost part of the fog, radiative cooling ceases and heat flux from the ground serves to evaporate fog droplets (ROACH, 1995). An example of such a situation of a fog layer lifted to a small height above ground is shown in figure 4.29. This data again is extracted from PINNICK *et al.* (1978). Again, there is no data above 155 m; it was assumed that liquid water content above this height linearly drops to 0 within a further 30 m. In agreement with the prediction stated above, this lifted profile is clearly sub-adiabatic and thus adequately approximated by the model. Ground fog confidence is at $P_g = 0.23$. The adiabatic model and parameterisation on the other hand overestimate cloud thickness.

The results of all three profiles discussed are summarised in table 4.2. Based on these profiles and the considerations presented in conjunction with them, it can be presumed that the sub-adiabatic profile assumption used in

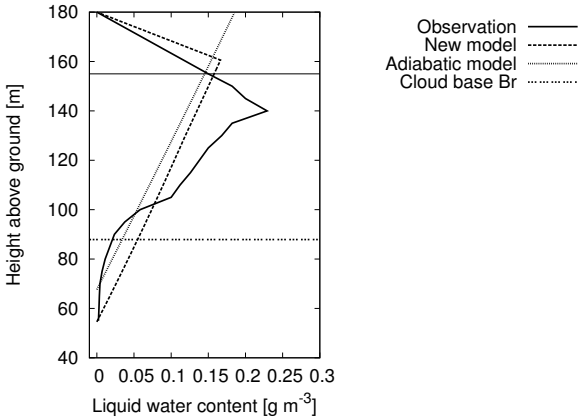

Figure 4.29: *A profile of uplifted fog as reported by* PINNICK et al. *(1978) with a cloud base height of 57.5 m. Explanations in figure 4.26. The thin horizontal line indicates the upper limit of the original data. For a listing of measurements and modelled values see 4.2.*

Profile (fig.)	W [gm^{-3}]	Cloud base observed [m]	Deviation new model [m]	Deviation adiabatic [m]	Deviation Brenguier [m]	Ground fog confidence
4.26	22.0	745	-4	-24	+76	0.00
4.28	99.0	0	-92.5	-60.5	+29	0.70
4.29	10.8	57.5	-1	+12	+30.5	0.23

Table 4.2: *Comparison of cloud base heights for the profiles presented in figures 4.26, 4.28 and 4.29 by different methods.*

the new model is valid for ground fog, low stratus clouds and lifted fog layers. The thickness of ground fog patches may be overestimated; however, this is not critical, as ground contact of the layer will be predicted accurately nonetheless in these situations. Based on the profile analysis discussed her, overall performance of the new model is expected to present a marked improvement over adiabatic assumptions.

In combination, the methods presented in this and the previous sections of this chapter make up the Satellite-based Operational Fog Observation Scheme (SOFOS). They are applied consecutively: First, low stratus areas are delineated, then cloud top height is determined for these, and finally, cloud base height is computed using the technique introduced in this chapter. In this way, fog and ground fog areas can be identified. The entire scheme is composed of predominantly new methods and tests combined in a unique and novel way to the end of fog detection.

Chapter 5

Validation and Appraisal

5.1 Validation Approach

In order to appraise the performance of the scheme, an extensive validation study was conducted. The central aim of this exercise was to reach an assessment whether the newly developed fog detection scheme is applicable in operational processing. The validation study consists of two types of evaluations:

- A comprehensive statistical evaluation of algorithm output for a set of scenes. Performance of both, very low cloud detection and ground fog delineation are explored separately.
- Analysis of selected scenes, highlighting strengths and weaknesses of the scheme and thus contributing to the explanation of the comprehensive results.

First, data selection and methodology are discussed, followed by a presentation of validation study results and a concluding appraisal.

5.1.1 Aims and Data Selection

The general target of a validation study is to assess the validity of a technique, i.e. its agreement with reality. In the particular case of an operational satellite-based product with spatially relevant results the following requirements must be met by a reference data set used in validation:

- Validity/reliability. A reference data set needs to be of trusted and operational quality.

- Good spatial coverage. Ideally, the entire study area should be covered with reference data evenly distributed.
- Appropriate temporal resolution. In order to track change over time, reference data should be available at a frequency of one hour or better.

As stated in the motivation for this work (chapter 1), no appropriate spatial data is available on fog distribution. Therefore, point data, i.e. from meteorological stations, needs to be used as a reference.

Ideally, full cloud geometry, with the parameters cloud top height and cloud base height (ceiling), and visibility at ground level should be available. Cloud top height however is rarely observed at ground stations, although the synergy effects to be gained from such measurements are great (Cermak *et al.*, 2006).

Standard measurements available from meteorological stations in Europe include ceiling and visibility. Data sets are available as station reports from individual national weather services, as used in Cermak & Bendix (2006). The main advantage of these is their excellent spatial coverage and good temporal resolution (1 h or less). However, as this data is not openly available, a comprehensive validation study for the area covered in this work would require numerous individual data contracts with many individual national weather services.

Station measurements of ceiling and visibility are also available globally in the processed forms of SYNOP (surface SYNOPtic observations) and METeorological Aerodrome Report (METAR). While the former are reported at time intervals of either three or six hours (depending on the station), METAR are available at least hourly. Therefore, METAR data were chosen as the reference data in this study. A description of the data is given in chapter 3, along with a map of METAR stations used for validation (figure 3.2). A total of 583 stations are included in the reference data set used.

The validation data set of satellite products needs to meet a few requirements in order to allow a reasonable interpretation. The ideal satellite product data set:

- Features a great range of atmospheric and cloud situations, allowing for a thorough assessment of the algorithm's skill in separating low cloud from higher cloud layers.
- Includes numerous different low cloud situations, so that the accuracy of ground fog detection can be tested.
- Covers all daytime hours.

It is highly unlikely that all three conditions will be met in a random set of satellite scenes, unless an extremely large sample is selected. Therefore, the validation data was chosen based on visual inspection. The sole criteria in the selection process were the requirements given above.

The satellite product data set chosen for validation consists of 1030 scenes. They cover 24 days in three periods in September (20–22), October (07–21) and November (05–10) 2005. Within the test data set, all available scenes were considered without prior selection. With 1030 scenes this data set is very extensive, covers a great range of meteorological situations and is thus very well suited for quantitative interpretation.

For each data point in the reference data set a corresponding value was extracted from the satellite product based on the ground station coordinates. To make sure only daytime pixels were used, the solar zenith angle was checked for each data point. Where it was larger than 80° (corresponding to a solar elevation of $< 10\,^{\circ}$), the pixel was skipped. Statistics were then computed for all remaining data points.

The satellite fog mask product was tested against presence of very low clouds (ground fog plus elevated fog) and presence of ground fog. Very low cloud presence was identified by means of cloud base height data. For ground fog presence, visibility information from the reference data set was used. Where visibility is below 1000 m, a ground fog situation is assumed.

5.1.2 Sources of Uncertainty

While the best available data set was chosen as validation reference (see above), still a number of potential and inevitable draw-backs need to be considered when evaluating this data validation in particular, and any type of satellite - ground-measurement intercomparison in general.

Sub-pixel effects. Ground-based point measurements do not necessarily represent the state of parameters over the entire pixel as recorded by the satellite sensor, so the measured effects may not be detectable in the pixel as a whole. In the case of MSG SEVIRI the nominal size of a pixel at sub-satellite point (0°N, 3.4°W) is 3 by 3 km, yielding an even larger area per pixel for Europe. Sub-pixel effects are of particular importance at the margins of a fog patch. Moreover, a meteorological station may be located at the intersection of two pixels, making it nearly impossible to attribute its data to either one. Therefore some cases of low cloud cover reported locally at a ground station may not be representative of a wider area and thus not picked up by the satellite sensor.

Collocation. While on the whole the geo-location of Meteosat 8 is stable, slight changes may occur in individual scenes. In operational processing, manual filtering of these scenes is impossible. One therefore has to consider that features may be found in a pixel other than the expected one in some instances. On top of this, the observation angle is of importance: In the study area, the satellite zenith angle ranges between about 45 and 65°. While this is no great problem for very thin fog layers with a top height close to sea level, it becomes increasingly problematic at higher elevations: The atmospheric column observed vertically from the ground does not match the slant column seen from the satellite at a given zenith angle. This results in the observation of different features at a seemingly collocated pixel.

Timing. One MSG SEVIRI hemispherical scan takes 15 minutes, from south to north. Therefore the nominal time (end of the scan cycle) assigned to each scene is not the actual scan time at a given location somewhere within that scene. For this reason the features observed on the ground may not always match those seen in a supposedly corresponding satellite image. This holds true especially for dissipating fog. Also, the METAR data is not recorded simultaneously at all stations. Reports may occur at any minute of the hour. For comparison with the satellite products all METARs collected within the 15 minute interval corresponding to a nominal SEVIRI scan cycle are compared to the products of the same.

Cloud overlap. The reference data set contains information on the lowermost cloud layer, while the satellite product describes the uppermost. The satellite product is therefore likely to miss any low cloud situations hidden below higher-level clouds, and well represented in the validation data set. This potential problem is explored in detail below.

Reference data availability/coverage. While the land masses in the study area are well covered by METAR stations, no reference data is available over the Atlantic Ocean and North sea (figure 3.2). However, the Mediterranean Sea and the English Channel are represented by some island stations.

Reference data accuracy. Lastly, the quality of the ground-based measurements is very variable. In many cases the parameters visibility and cloud height are not derived from measurements (transmissometers, ceilometers) but estimated by a human observer. In the latter

case the data are only classified roughly and depend on the highly subjective assessment of a person (WMO, 1996). Nonetheless METAR data represents the international standard of ground-based measurements and has been used successfully in similar validation studies (e.g. Fowler *et al.*, 2004).

All these factors present limitations on the quantitative interpretability of the validation study results. However, they are mostly system-inherent to the validation of a satellite product and cannot be eliminated or abated. Moreover, as long as these limitations are kept in mind when interpreting the statistical results of the validation study, a thorough and useful exploration of product strengths and weakness is possible.

5.1.3 Intercomparison Methodology

The *skill* of a forecast or classification is defined as the improvement over an uninformed random prediction (Briggs & Ruppert, 2004). The quantitative skill assessment for such dichotomous classifications is a common task in the analysis of spatial products. In the climatology and meteorology domains, the use of contingency-table-based statistics has a long tradition and is still widely recognised as the most appropriate approach to product validation. A wide number of scalar indicators have been proposed, applied and evaluated (e.g. Baldwin & Kain, 2004; Brooks & Doswell, 1996; Doswell *et al.*, 1990; Marzban, 1998; Murphy, 1993; Stephenson, 2000; Thornes & Stephenson, 2001; Wilson & Burrows, 2004; Wright & Thomas, 1998; Zhang & Casey, 2000). Out of these, a range of indicators were chosen based on their specific information content and successful application in similar studies. They will be briefly introduced in the following paragraphs.

The basis of all indicators is a 2 by 2 contingency table showing agreement and disagreement in the dichotomous classification to be tested and reference data set (table 5.1). In this table, A gives the number of correctly predicted instances of the property (hits), B false alarms (property predicted but not present), C misses (property present but not predicted) and D correct negatives. The sum of all columns and rows $A + B + C + D = n$ is the total size of the sample.

For each comparison data set a table of this kind is computed. The statistical indicators are calculated based on the values A to D, as detailed in table 5.2. The following paragraphs briefly highlight the focus and interpretation of each indicator.

	Observation Yes	Observation No
Prediction Yes	A	B
Prediction No	C	D

Table 5.1: *Contingency table. A: Correctly identified situations (hits), B: False alarms, C: Misses, D: Correct negatives.*

Accuracy (Acc). This is a very simple indicator of the overall prediction quality, calculated as the ratio of correct predictions and the sample size. While generally a value of 1 indicates optimum accuracy, nothing is said about the relative importance of correct identifications (A) and correct negatives (D). This can be misleading in cases with either a very low or a very high frequency of the sought property.

Bias Score (BS). The bias establishes an indirect relation between false alarms (B) and misses (C) and can be interpreted as a measure of overestimation ($BS > 1$) or underestimation ($BS < 1$) of the property in question.

Hit Rate (HR). Also referred to as 'probability of detection', the hit rate quantifies the skill of a method in correctly predicting the presence of a property. It expresses the portion of hits in all positive observations, i.e. the fraction of properly detected situations.

Probability of False Detection (PFD). In analogy to the hit rate, the probability of false detection expresses the portion of false alarms in all negative observations.

False Alarm Rate (FAR). The false alarm rate gives the portion of false alarms in all positive predictions. This indicator is sensibly interpreted together with the hit rate.

Threat Score (TS). The threat score (also: 'critical success index') considers hits, false alarms and misses and is interpreted as an indication of overall classification correctness. It is the total fraction of the correctly identified situations in all predictions and observations. This measure is very robust regarding sample distribution. In joint interpretation with hit and false alarm rates, a good characterisation of classification skill can be reached.

Hanssen–Kuipers Discriminant (HKD). This parameter combines all four fields of the contingency table. In essence, it is the difference

between hit rate and probability of false detection and thus aims to express overall prediction skill.

Each of these indicators has its particular strengths and weaknesses, so that for each validation test all values will be given and interpreted as appropriate. While this compilation of course does not comprise the full range of statistical indicators available (see above), it is fully appropriate in the light of the present study. A very good characterisation of the classification results can be obtained by applying a combination of the mentioned tests.

Name	Equation	Range	Best
Accuracy	$Acc = \frac{A+D}{n}$	$0 \cdots 1$	1
Bias Score	$BS = \frac{A+B}{A+C}$	$0 \cdots \infty$	1
Hit Rate	$HR = \frac{A}{A+C}$	$0 \cdots 1$	1
False Alarm Rate	$FAR = \frac{B}{A+B}$	$0 \cdots 1$	0
Probability of False Detection	$PFD = \frac{B}{B+D}$	$0 \cdots 1$	0
Threat Score	$TS = \frac{A}{A+B+C}$	$0 \cdots 1$	1
Hanssen–Kuipers Discriminant	$HKD = \frac{A}{A+C} - \frac{B}{B+D}$	$-1 \cdots 1$	1

Table 5.2: *Statistical indicators used in this study, with computation, theoretical range of values and best value (for a maximum skill prediction).*

In order to compensate for the collocation issues outlined above, all indices were computed not only for individual pixels, but also for a 3 by 3 pixel environment. This approach was based on the assumption that the sought-after ground station might be represented in one of the pixels neighbouring the one identified as the theoretical location. Each 3 by 3 pixel environment was therefore tested for the presence of the feature found in the corresponding ground station data. Where any one of the pixels agreed with the reference measurement, it was taken to be the sought-after location. Since this approach is somewhat biased, both, the pixel-based and the 3 by 3 approaches are represented in the following.

5.2 Validation Study

In the following, the results of the validation study will be presented and interpreted. After a short description of the satellite product data set, low cloud presence statistics are analysed; then, the same is done for ground fog. Both main parts start with a discussion of summary statistics and then analyse these in detail, using example scenes where appropriate.

5.2.1 Product Data Set

The share of low cloud and fog situations in a satellite scene depends on the meteorological situation encountered and may vary widely. This is expressed in a cloud classification derived from the cloud tests described in section 4.2. Table 5.3 summarises the classification results for the validation period. The variability of the scenes is very well represented in these figures. Total cloud cover as well as the frequencies of cloud types vary widely, so that a great range of very dissimilar cloud situations are indeed covered by the validation data set. The average scene has a cloud cover of slightly more than half the pixels, 2 fifths of which are ice clouds. The water clouds are split into medium and high clouds (1 quarter) and low clouds, with roughly a third of the latter low stratus. Of the low stratiform clouds, about one quarter have ground contact (ground fog).

Class	Min	Max	Mean	Standard Deviation
Clear	2.94	97.49	44.68	15.91
– Snow	0.00	2.24	0.26	0.21
Ice cloud	0.00	61.72	23.62	10.73
Medium/high water cloud	0.36	34.47	6.85	4.45
Low water cloud	0.00	56.87	24.84	9.24
– Low stratus cloud	0.00	56.64	7.73	4.59
– Ground fog	0.00	8.73	2.01	1.81

Table 5.3: *Shares of individual (cloud) classes in percent of the total area of the 1030 scenes considered. Indented classes are included in the count of the previous non-indented class.*

In figures 5.1 and 5.2 the relative frequencies of very low clouds (ground plus elevated fog) and ground fog respectively are given over the validation study period. No particular pattern can be observed in the distributions; the data set displays a great variation on the temporal axis.

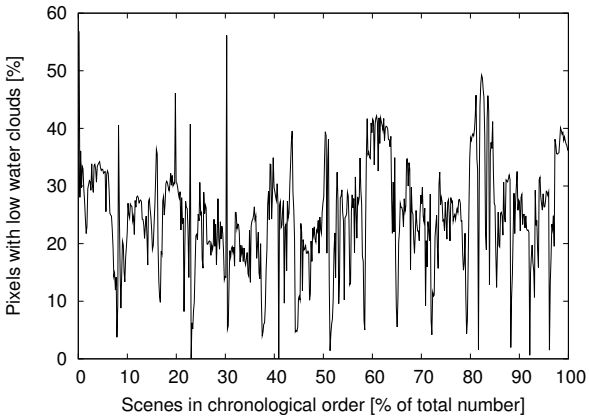

Figure 5.1: *Share of low water cloud pixels in each scene, from the first to the last scene in the data set (abscissa in % of total scenes used, chronological order).*

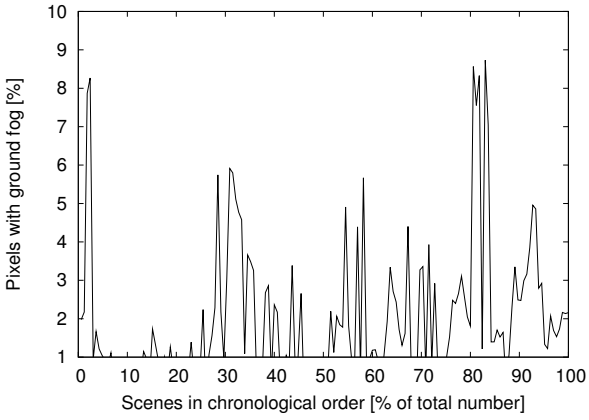

Figure 5.2: *Share of ground fog pixels in each scene, from the first to the last scene in the data set (abscissa in % of total scenes used, chronological order).*

5.2.2 Very Low Cloud/Ground Fog Plus Elevated Fog

Table 5.4 summarises the results of the statistical appraisal of very low cloud detection based on the validation methodology discussed above. Figures for both the single-pixel and the 3 by 3 pixel environment approaches are presented. The accuracy figures reveal that 56% of situations were correctly classified in the former and 71% in the latter case. At 15% the differences between both approaches are therefore evident. Both methods however agree in that by tendency the number of very low cloud situations is underestimated by the algorithm, as shown by bias scores of 0.67 and 0.77. Underestimation is marked for the single-pixel approach (BS = 0.67) and smaller, but still considerable for 3 by 3 pixels. The combination of hit rate and false alarm rate corroborates this conclusion: 52 and 68% of situations are properly detected. Therefore, even in the 3 by 3 pixel comparison, slightly more than 30% of very low cloud situations go undetected. At the same time, the number of very low cloud situations falsely reported by the algorithm for this approach is low at 12% (22% for single-pixel comparison). The probability of false detection is somewhat higher than the FAR, resulting in Hanssen–Kuipers figures of 0.17 and 0.46 for the approaches respectively. At 0.62 the threat score computed for the 3 by 3 pixel case shows that overall, good skill can be expected from the algorithm. In this as in all other figures a marked difference between the single-pixel and more suitable 3 by 3 pixel approaches is evident.

Indicator	1 pixel	3 x 3 pixels
Acc	0.56	0.71
BS	0.67	0.77
HR	0.52	0.68
FAR	0.22	0.12
PFD	0.36	0.22
TS	0.46	0.62
HK	0.17	0.46

Table 5.4: *Statistical summary of the very low cloud validation study for the single-pixel approach and the 3 by 3 pixel environment (for details see text).*

Figure 5.3 differentiates the threat score by station over the validation study period (3 by 3 pixel approach). No clear regional bias towards better performance in any particular part of Europe can be observed. Very good skill is found in marine regions, continental plains and the peri-alpine areas

alike. Interestingly, stations close together sometimes display noticeable discrepancies in skill. Mildenhall (52.4°N, 0.6°E) and Lakenheath (52.4°N, 0.5°E, about 10 km further west) for instance have very different threat scores (0.20 and 0.82 respectively, overlapping in figure 5.3). This may possibly be an indication of poor station data quality in some cases. As stated above already, this is a factor to be considered in the interpretation of the statistics.

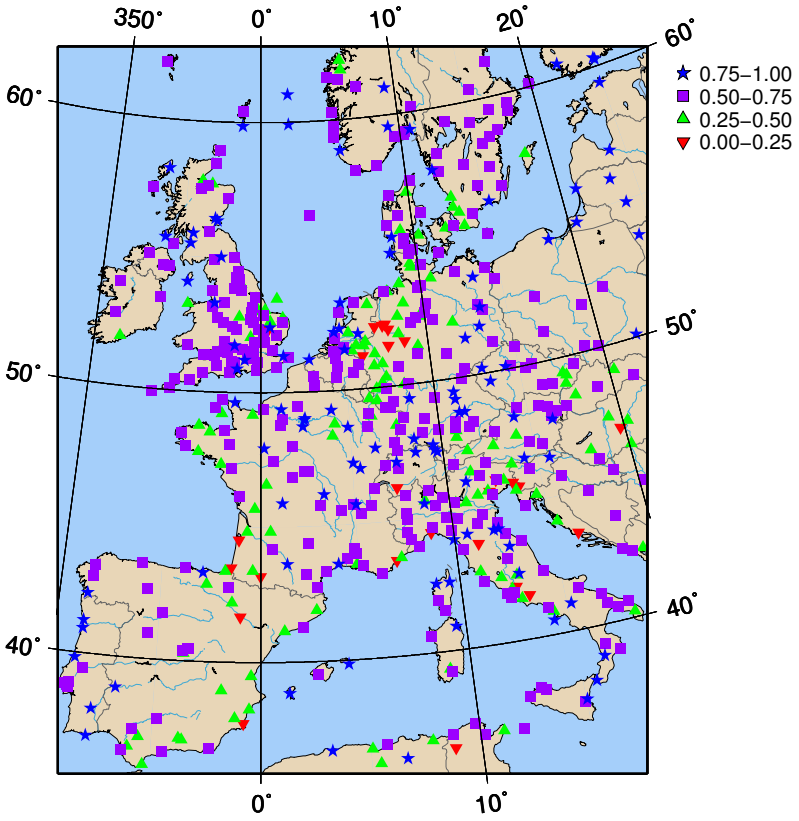

Figure 5.3: *Threat scores by station for the validation study period (3 by 3 pixel approach). For discussion see text.*

As mentioned above, the hit rate is very likely kept low artificially by cloud overlap; some low cloud situations observed from the ground cannot be detected from the satellite perspective, because they are 'hidden' under higher-level clouds. In addition, high-reaching frontal clouds (cumulus, cumulonimbus) frequently have low ceiling heights as well; Although their tops are in higher levels of the troposphere, they would thus be (incorrectly) indicated as low clouds in the reference data. Indeed, as shown in table 5.3, on average about 30% of the total scene area, corresponding to more than

50% of the cloud area, was classified as some high or medium level cloud (ice or water).

The 1030 UTC scene of 8 November 2005 is a good example of such a situation. The central and south-eastern parts of the scene are dominated by a high pressure area centred on the Czech Republic and reaching to Spain and the Ukraine. Radiation fog patches are present in several countries, including France, Germany, Italy and Switzerland. In the north-western part of the scene, a low pressure area with its centre to the north of the British isles influences the weather. A cold-frontal cloud band stretches from northern Portugal to Finland. Figure 5.4 shows the satellite classification (simplified into high and low cloud classes) in conjunction with the corresponding METAR observations (classified into low cloud, high cloud and clear cases). The thermal infrared image shown in figure 5.5 very clearly underlines the presence of the cold (high) cloud band. A great number of 'low cloud' METAR observations are located within this band. Assuming that these measurements are correct, high-reaching clouds are obviously the source of this disagreement between satellite and reference data assessment.

The hit rate for this particular scene is 66% (FAR = 9%, TS = 62%, 3 by 3 pixel approach), which is close to the overall value of all scenes . If one were to leave aside all situations with high-level clouds identified in the satellite product, the hit rate would rise to 93% (FAR = 9%, TS = 85%) for this scene. In the case shown here, and presumably many more, the 'true' scheme performance therefore is much better than suggested by the previous hit rate figure of 66%.

In order to estimate the potential scale of cloud overlap and high-reaching clouds for the entire validation data set, the validation presented in table 5.4 has been recomputed. In this re-computation low cloud situations found in the reference data set but matched with high-level clouds in the product were not considered. Of course this will also exclude misclassifications of cloud height; the new figures are therefore only meant as a rough indication of the potential scale of this technical problem. The hit rate is increased markedly now, to 71% for the single-pixel approach and 85% for the 3 by 3 pixel environments. This indicates that the combination reference low – product high does indeed account for many of the previously undetected low cloud situations.

The analysis of the low cloud situations still missed after the exclusion of overlapping cloud layers reveals a great portion of situations with little cloud cover at the station. METAR data contains cloud cover information sorted into 5 classes: 'none', 'few clouds' (corresponding to 1 or 2 okta = eights), 'scattered clouds' (3 or 4 okta), 'broken clouds' (5 to 7 okta), and 'overcast'

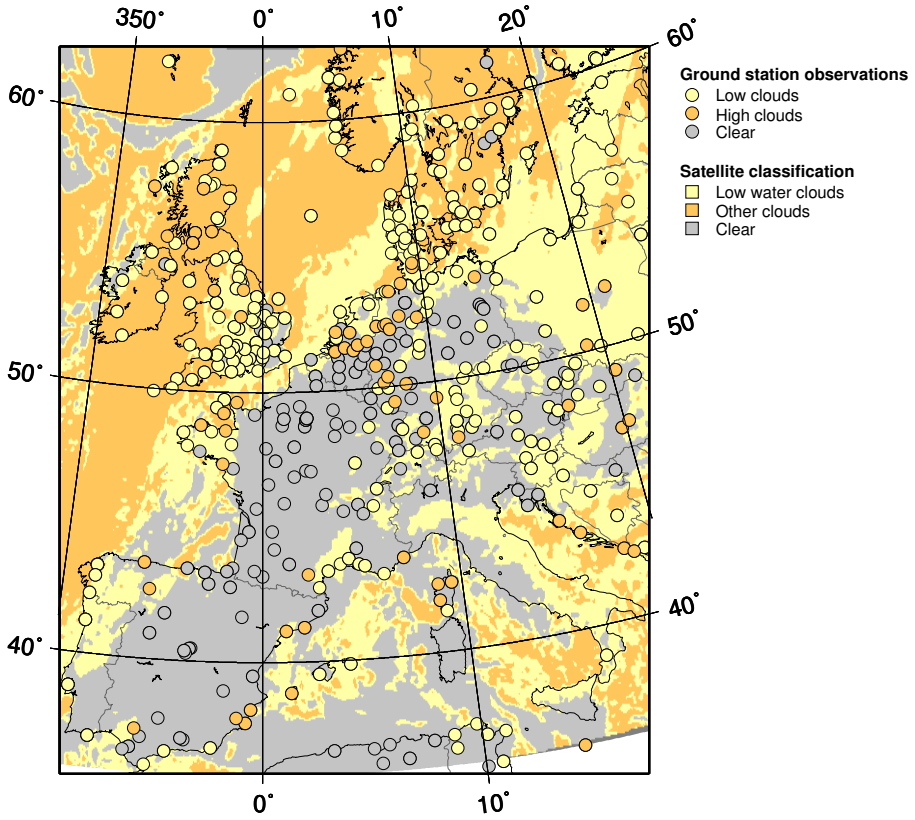

Figure 5.4: *Simplified satellite cloud classification and corresponding METAR observations, 1030 UTC, 8 November 2005. The corresponding infrared image is shown in figure 5.5 for orientation.*

(8 okta). Figure 5.6 shows that the greatest portion of the low missed cloud situations falls into the categories with 4 okta (1/2) or less cloud cover. Given the large sample distance of MSG over Europe, it appears very likely that few or scattered low clouds will not be visible at the pixel level, i.e. the observations are only of local relevance and thus not represented in the signal recorded by the satellite sensor.

A typical example of such a situation is presented in the scene of 0900 UTC, 22 September 2005 (figures 5.7 and 5.8). This scene is dominated by a high pressure area centred on the southern Baltic area and covering most of continental Europe. A very persistent low stratus field extends across the Baltic Sea and further south-eastwards. Radiation fog formed overnight in many valleys throughout continental Europe. By 0900 UTC many of these patches have cleared already, others remain at least partially. Figure 5.7 gives an overview of the cloud cover situation along with a simplified satellite classifi-

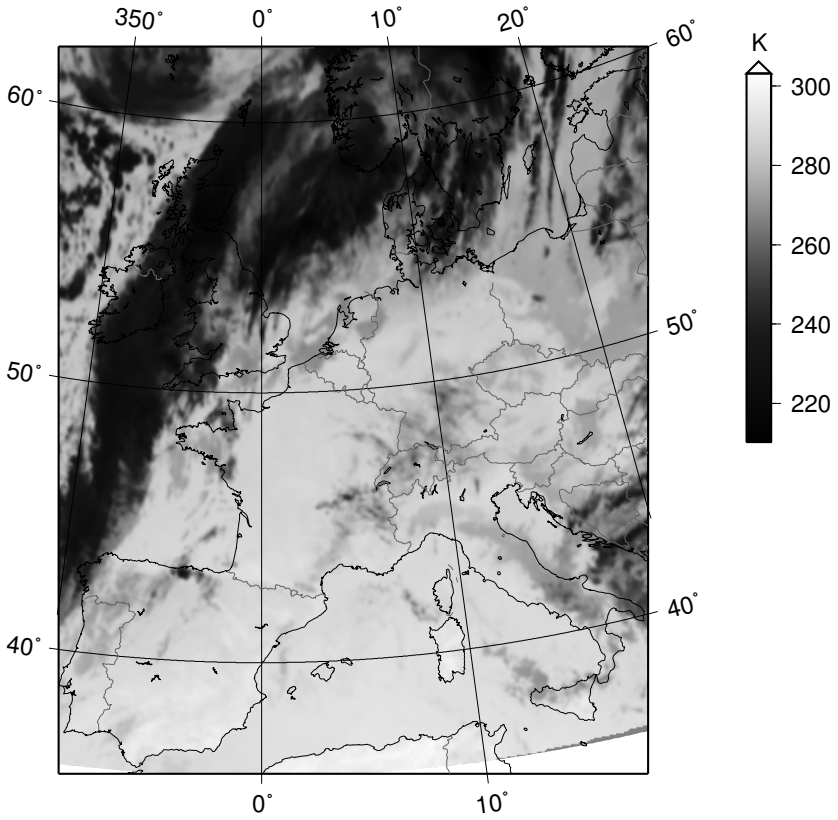

Figure 5.5: *10.8 µm channel blackbody temperature image, as a complement to figure 5.4.*

cation. Cloud cover data in the areas not classified as cloudy by the satellite algorithm almost uniformly indicates 'few' clouds, with isolated occurrences of 'scattered' clouds. Many misses occur in southern Germany – these are very likely fog patches in their final dissipation stages. None of the missed cloud situations here or elsewhere can be detected by visual inspection of the corresponding reflectance image, the cloud cover very obviously is too locally confined to be representative at the spatial resolution of MSG SEVIRI. The hit rate for this scene is at 70%, which again is close to the overall value for all scenes. After the removal of cloud overlap situations as performed above, the hit rate for this scene would be 83%. If in addition all misses with cloud cover of 4 okta or less were removed, 99% of low cloud cases would be detected accurately.

In order to quantitatively assess this for the entire data set, the hit rate for all scenes has been recomputed not only excluding overlap (as above), but also all missed low cloud situations with few or scattered clouds (half

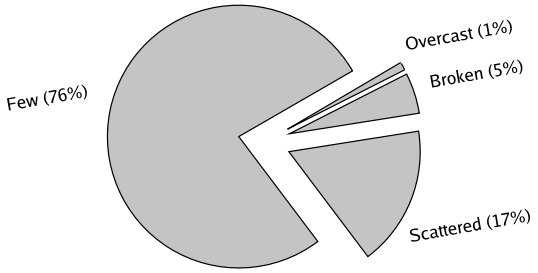

Figure 5.6: *Distribution of missed low cloud situations by cloud cover classes. 'Few' corresponds to 1–2 okta (eigths), 'Scattered' to 3–4 okta, 'Broken' to 5–7 okta, and 'Overcast' to 8 okta.*

of the sky or less covered by clouds). Now, the hit rate would rise to 95% (single-pixel) and 98% (3 by 3 pixel environment). This underlines the initial conjecture that the missed low cloud situations are mostly too small and locally confined (non-representative) to be detected by the satellite sensor.

5.2.3 Ground Fog

The presence of ground fog was tested against visibility measurements in the reference data set, with ground fog defined as a situation with a visibility of up to 1000 m (cf. chapter 2). On the satellite side, all predictions with a ground fog confidence level P_g of 0.5 or greater were considered ground fog (see section 4.4). As cloud geometry computation is only implemented for clouds previously identified as very low stratus (see chapter 4), the validation statistics consequently only include these cases.

Table 5.5 summarises the statistical results. Again, the 3 by 3 pixel environment displays a much better skill. The accuracy of both approaches is at the maximum of 1.00, mostly due to the numerous correct negatives (D in table 5.1, correctly identified non-ground-fog situations). The bias score points to a slight overestimation of ground fog situations for the single-pixel approach. However, the combination of hit and false alarm rates reveals a significant under-detection coupled with high levels of false alarms. This is also expressed in the low threat score of 0.26.

The poor skill obtained in the single-pixel approach can probably be attributed to small-scale variations in surface elevation. The ground fog confidence level is obtained by comparing computed cloud base height with a surface elevation value extracted from a digital elevation model at the spatial resolution of SEVIRI. However, the averaged elevation value for each of these pixels is unlikely to agree with the actual station elevation, leading

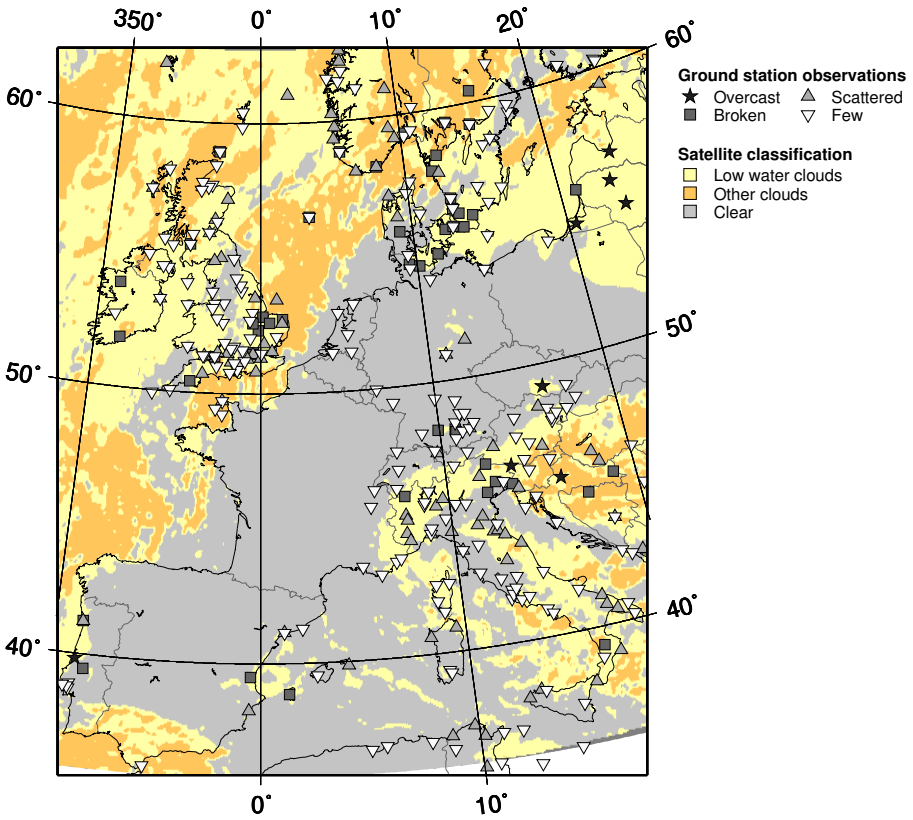

Figure 5.7: *Cloud cover observed at METAR stations compared with the satellite classification, 0900 UTC, 22 September 2005. Reflectance measured in the 0.6 µm channel is given for orientation in figure 5.8.*

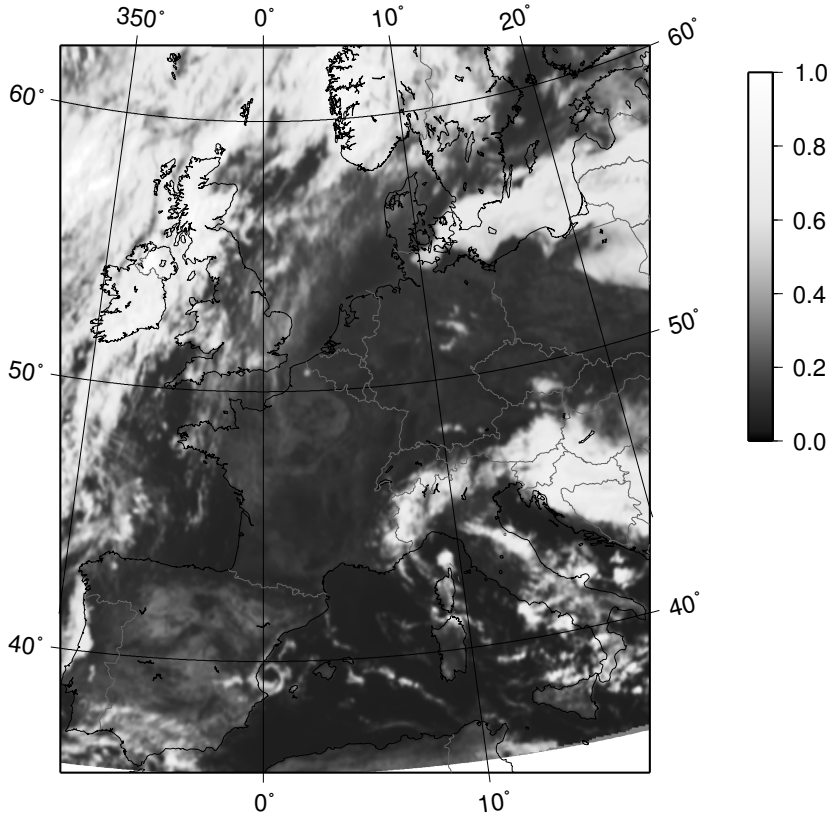

Figure 5.8: *Reflectance measured in the 0.6 µm channel, 0900 UTC, 22 September 2005. The corresponding cloud classification is shown in figure 5.7.*

to misestimations of ground fog presence.

Accordingly, the 3 by 3 pixel approach yields much better results. At constant accuracy, the threat score now more than doubles (0.58), the hit rate reaches a satisfactory 74% and the false alarm rate drops to 27%.

Indicator	1 pixel	3 x 3 pixels
Acc	1.00	1.00
BS	1.53	1.02
HR	0.52	0.74
FAR	0.66	0.27
PFD	0.00	0.00
TS	0.26	0.58
HK	0.52	0.74

Table 5.5: *Statistical summary of the ground fog validation study for the single-pixel approach and the 3 by 3 pixel environment (see text), using elevation data from a digital elevation model at satellite spatial resolution. Results based on a ground fog confidence level of 0.5.*

In the light of these findings, a more appropriate approach to ground–satellite intercomparisons may be the use of individual station elevation data instead of the averaged satellite-scale digital elevation model. In this approach, the ground fog confidence level is computed using satellite-derived cloud base height and the surface elevation of the respective METAR station. The statistical indicators were thus recomputed using these station-specific confidence levels, again with a cut-off level of $P_g = 0.5$. The results are presented in table 5.6.

Indicator	1 pixel	3 x 3 pixels
Acc	1.00	1.00
BS	2.03	1.11
HR	0.56	0.81
FAR	0.72	0.27
PFD	0.00	0.00
TS	0.23	0.62
HK	0.56	0.81

Table 5.6: *Statistical summary of the ground fog validation study for the single-pixel approach and the 3 by 3 pixel environment (see text), using real elevation data for each ground station. Results based on a ground fog confidence level of 0.5.*

The most obvious change is a increase in the hit rate in both, the single-pixel and 3 by 3 pixel approaches. The overall quality of the former changes only very little as indicated by threat score and Hanssen–Kuippers discriminant. This is due to an increased false alarm ratio. For the 3 by 3 pixel environment, results have improved however. At a constant false alarm rate the hit rate has risen by seven points to 81%.

A portion of the false alarms may possibly be explained by the wind speed near the ground: Where this parameter is too large, fog cannot persist directly at the ground surface, although it may still be present at very low elevations. The average wind speed reported by METAR stations for the correctly identified ground fog situations is 1.5 m/s, with a standard deviation of 1.3. For false alarms, i.e. situations incorrectly classified as ground fog, average wind speed reaches 3.2 m/s, more than one standard deviation in excess of mean ground fog wind speed. It thus seems plausible that local variations in wind conditions very near the ground may indeed alter the visibility conditions at the surface. The small changes produced by this process are not detected by the satellite sensor, leading to false alarms.

The probability of false detection figure remains at 0, owing to the large number of correct negatives. This leads to an increase in the Hanssen–Kuipers discriminant to 81%. The overall threat score now reaches 0.62 showing that good skill can be expected from the ground fog detection scheme.

The distribution of threat scores in the study region is shown in figure 5.9. Only stations with ground fog reports in the validation study period are shown. As in the very low cloud validation (figure 5.3), no clear regional pattern can be detected, indicating that the skill level is approximately even throughout the study area. Some of the smaller threat scores are at or near river courses, and thus possibly in varied relief. But the data does not allow for any definite conclusions in this regard.

In the validation statistics presented above, a cut-off ground fog confidence level of 0.5 was used. The reason behind this choice is that 0.5 is defined as the level where cloud base height and surface elevation match. In order to assess the changes incurred by varying this threshold, statistics were also computed for other cut-off levels. The variation of hit and false alarm rates with changes in threshold was explored in more detail. The receiver operating characteristic (ROC) curve is a common form of presentation for such analyses of probabilistic classifications (Wilson & Burrows, 2004; Marzban, 2004). In a normal ROC, hit rate and probability of false detection are plotted on the axes. Since the large number of correct negatives in combination with the 3 by 3 pixel approach keeps PFD values very low how-

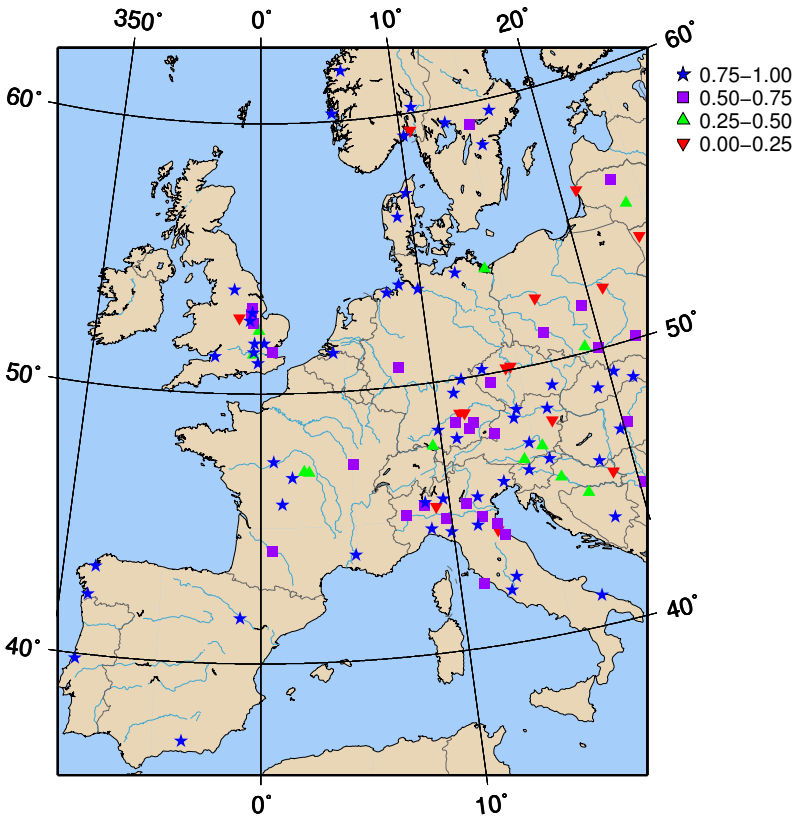

Figure 5.9: *Threat scores by station for the validation study period (3 by 3 pixel approach) for ground fog presence. Only stations with ground fog reports in the validation study period are shown. For discussion see text.*

ever, a pseudo-ROC presentation using FAR was chosen here. Figure 5.10 shows the variation in hit rate and false alarm rate for a range of ground fog confidence levels.

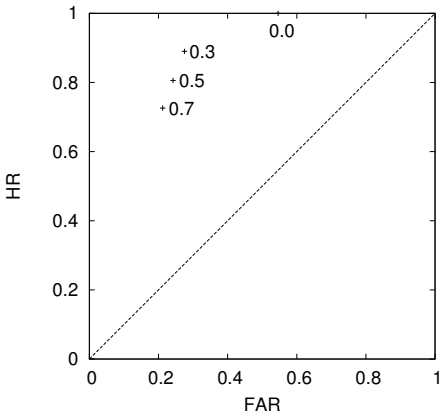

Figure 5.10: *The skill of the fog detection algorithm at different ground fog confidence levels (indicated by the numbers next to the data points). Skill is plotted as a function of false alarm rate (FAR) and hit rate (HR). Numerical labels are fog confidence levels. The diagonal line represents a hypothetical forecast with no skill.*

Generally, proximity to the upper left hand corner of the plot indicates increasing skill of a classification. The positions of points in the plot very clearly show that scheme performance with varying probability levels is a trade-off between hit and false alarm rates, as one increases with the other. In this case, the classification remains well above the zero skill line for all probability levels plotted (as shown in the plot), indicating that the ground fog classification scheme is of reliable quality. The application of a ground fog probability cutoff level of 0.5 appears appropriate in this context.

5.3 Validation Summary

The validation study has provided insights into the strengths and weaknesses of the newly developed fog detection scheme. Separated into comparisons for the detection of very low cloud and fog, and ground fog delineation, statistical evidence for algorithm skill has been presented. The study results suggest throughout that the intercomparison of product and reference data on a 3 by 3 pixel matrix is more appropriate than a single-pixel approach.

Of the very low cloud situations present in the reference data set, about 70 to 85% are detected by the new scheme. The undetected occurrences can

largely be explained by cloud overlap, high-reaching clouds and sub-pixel cloudiness. The false alarm rate is low at 12%.

Ground fog delineation was also achieved to a satisfactory degree, with a hit rate of 81% and a threat score of 0.62. The skill of the new scheme is considerably better than a naive forecast despite misclassifications in some situations.

A number of uncertainties concerning data comparability and quality make a strictly quantitative interpretation of the results difficult. Nonetheless, the study has clearly highlighted the skill of the new scheme. The applicability of the new method in an operational framework can therefore be assumed, for both very low cloud detection and ground fog delineation.

Chapter 6

Summary and Outlook

6.1 Summary

Knowledge of fog spatio-temporal distribution is of great value in the fields of climatology, traffic safety and air quality monitoring. So far, no adequate method existed for the detection and monitoring of fog at high temporal and spatial resolutions. Meteorological station measurements lack the spatial coverage and interpolation proves impractical. Satellite retrievals used to be available only on polar orbiting platforms due to spectral constraints, with poor temporal resolutions. Further, objective daytime satellite-based fog detection was an unsolved problem with operational algorithms only available for nighttime.

The central aim of the present study therefore was to develop a novel method for the operational detection of daytime fog based on geostationary satellite data, the Satellite-based Operational Fog Observation Scheme (SOFOS).

With the advent of Meteosat Second Generation (MSG) Spinning-Enhanced Visible and Infrared Imager (SEVIRI) in 2003, a geostationary satellite system with significantly improved spectral and spatial resolutions has become available. The main thesis of this study was that operational daytime fog detection is possible using data of this system. The approach taken to explore this conjecture rests upon three hypotheses:

1. Fog can be detected by implicitly and explicitly addressing its physical and spatial features.

2. Ground fog detection can be based on cloud geometry information, i.e. a computation of cloud thickness and cloud height.

3. The above criteria are sufficiently stable to allow for automated, objective fog detection in any unknown data set.

The exploration of these hypotheses required the development and assembly of an entirely new methodology composed of a wide range of novel and innovative algorithms and approaches. The successful development and implementation of this new technique consisted of three components:

1. A new method for the delineation of very low stratus clouds was developed. This technique is based on the assumption that both ground and elevated fog manifest themselves as very low stratiform clouds. A series of spectral and spatial tests was developed to identify various fog properties and thus reach a separation of fog and very low stratus from conflicting surfaces such as clear areas and non-fog clouds. The spectral tests provide a rough separation of cloudy and clear surfaces, as well as exclusion of some obvious non-fog cloud types. These spectral tests are largely new developments, while some had to be adapted to the specific requirements of the SEVIRI system. In the second part of the scheme, a newly devised innovative approach based on spatially coherent and discrete entities of cloud-covered pixels is used to identify very low and stratiform cloud areas.

2. The detection of ground fog was addressed with the development of a novel technique for the determination of very low stratus geometry. Ground fog is assumed to be present where the base of a given cloud is at the ground surface. As cloud base height cannot be retrieved directly, but results from the difference of cloud top height and cloud geometrical thickness, techniques for the retrieval of the latter two parameters were developed and implemented. Cloud top height is computed using a considerably enhanced version of a cloud margin height interpolation technique. For cloud thickness retrieval, a new cloud profile model was developed. It is based on a microphysical cloud model simulating liquid water distribution within a stratiform boundary layer cloud with given height and temperature constraints. The relation of cloud top height, computed cloud base height and surface elevation is used to derive a ground fog confidence level as a predictor of ground fog occurrence in each location.

3. An operational framework for the near-real-time processing of Meteosat SEVIRI data and product generation, FMet, was developed. This framework serves four purposes:

- To handle incoming raw satellite data and convert it into a form usable by the product algorithms. This includes image calibration, geometry computation and regional sub-setting.
- To provide a range of newly developed and specially adapted auxiliary products required by the subsequent fog detection algorithms. The most important among these are the clear sky reflectance, precipitable water content and surface temperature products.
- To serve as a framework within which product algorithms are implemented.
- To handle post-processing, i.e. archiving, format conversion and projection.

FMet was newly developed along these lines and implemented on standard PCs.

The fog detection scheme was tested in an extensive validation study using Meteorological Aerodrome Reports (METARs) as reference data. The detection of very low clouds and ground fog were assessed separately and both products were shown to be very stable and reliable. The validation study area includes most of western and central Europe with land and sea areas and thus spans a wide range of very different conditions for fog formation. As no significant regional differences could be observed in algorithm performance and since the latter does not depend on any region-specific assumptions, the transferability of the new scheme to other areas may be safely assumed.

The validation study shows that the initial hypotheses could not be falsified and should be accepted: The detection of fog is possible by means of the new technique, which incorporates the delineation of very low stratiform clouds and cloud geometry considerations into an operational framework. A solid, objective and reliable approach is thus found to overcome the deficits of previously existing methods, both satellite-based and other.

The operational near-real-time observation of fog in a spatially adequate perspective has thus become possible for the first time, opening up many new perspectives. Possible applications include

- The near-real-time monitoring of fog development in space, with implications on short-term traffic safety decision.
- The improvement of fog forecasts and air quality monitoring.

- Statistical evaluation of low stratus frequency and dynamics as a basis for the quantification of climatological effects.

To all of these applications, the new scheme provides invaluable information not available before from any source.

6.2 Outlook

As an outlook and a demonstration of the potential of SOFOS, the scheme's applicability in the climatological domain will be briefly highlighted in the following. Climatological studies were cited as one motivation for the present research in the introduction (chapter 1). While the short time series of MSG SEVIRI data available so far does not allow for climatologically significant deductions, the potential of such data aggregations and statistical evaluations can nonetheless be highlighted on this basis.

So far satellite-based fog climatologies had to rely on data from polar orbiting satellite systems (e.g. Bendix, 2001a,b, 2002). Therefore, no more than one or two satellite overpasses were available per day. With the new method based on MSG SEVIRI data, a much more complete picture of fog occurrence can be drawn. The number of fog days or hours can be used instead of a relative frequency. Also, while previous approaches included the preselection of appropriate satellite scenes, the new algorithm is operational and thus can be applied automatically, even to scenes contaminated by other clouds and with no fog occurrence at all.

In order to briefly highlight the potential of the new scheme for climatological applications, results have been aggregated for some sample time series. Figure 6.1 shows the number of days with observations of very low stratus at daytime for 2004. Following the international definition of a *fog day* (WMO, 1992), all days with the occurrence of very low stratus at any time were considered in the aggregation. The products computed for all relevant 12823 daytime scenes were used, corresponding to a 15 minute interval over all 366 days of the year.

The general distribution pattern of elevated fog and very low stratus clouds shows good agreement with the expected situation. Marine low stratus frequency in the Atlantic and North Sea regions is very high and easily explained by the high moisture availability. The Mediterranean on the other hand displays much lower frequencies. This is due to the higher temperatures in this area. Southern Europe on the whole had a smaller number of daytime very low stratus situations in 2004 for that same reason. Fog frequently clears very early. As this composite image represents daytime

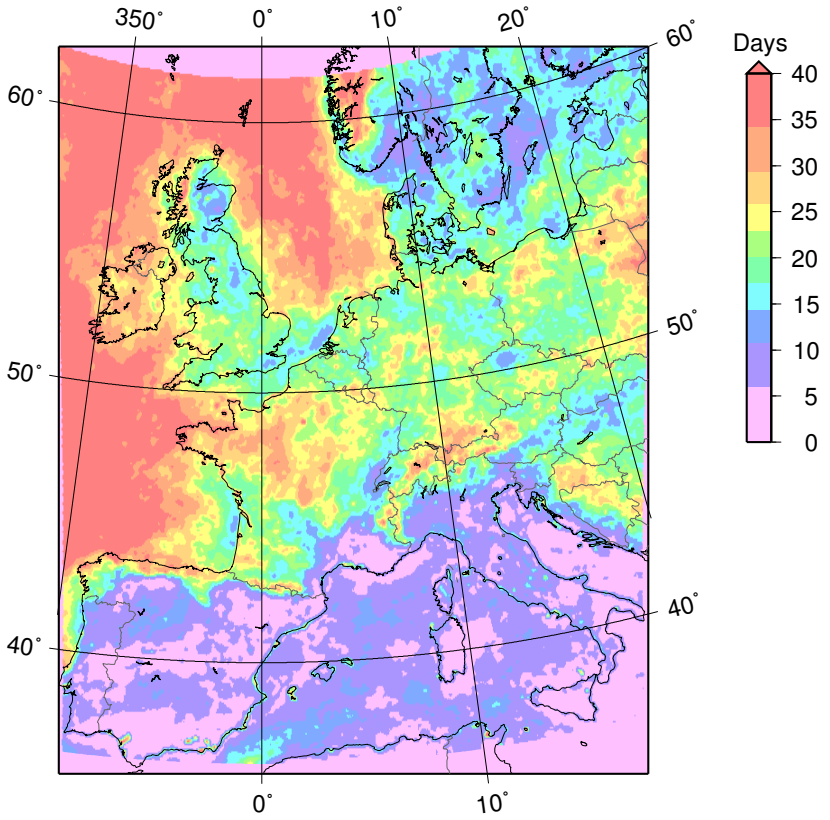

Figure 6.1: *Number of days with daytime very low stratus cover in 2004, based on 12823 scenes (366 days).*

situations only, the relative importance of radiation fog is reduced. The importance of advective fog situations increases with elevation, as the relative cloud height decreases. Therefore, mountain ranges (most prominently the Alps) feature higher frequencies of very low stratus than valleys.

Another implication of using daytime scenes is that a high number of fog situations in advanced stages is observed. One instance of this can be seen in the Upper Rhine Valley between the Vosges Mountains and the Black Forest, where a higher frequency is observed in the eastern half (German side). This is probably representative of radiation fog dissipation, where remaining cloud patches drift with the prevailing western winds. The straight line along the northern edge is an artifact produced by the entity-based components.

As another example, figure 6.2 shows the number of daytime ground fog hours detected in December 2004, based on all 1665 relevant scenes of this month. The aggregation of meteorological properties by hours is quite customary in climatological evaluations (e.g. for sunshine hours). With

the new fog detection scheme, this kind of satellite application has become possible for the first time.

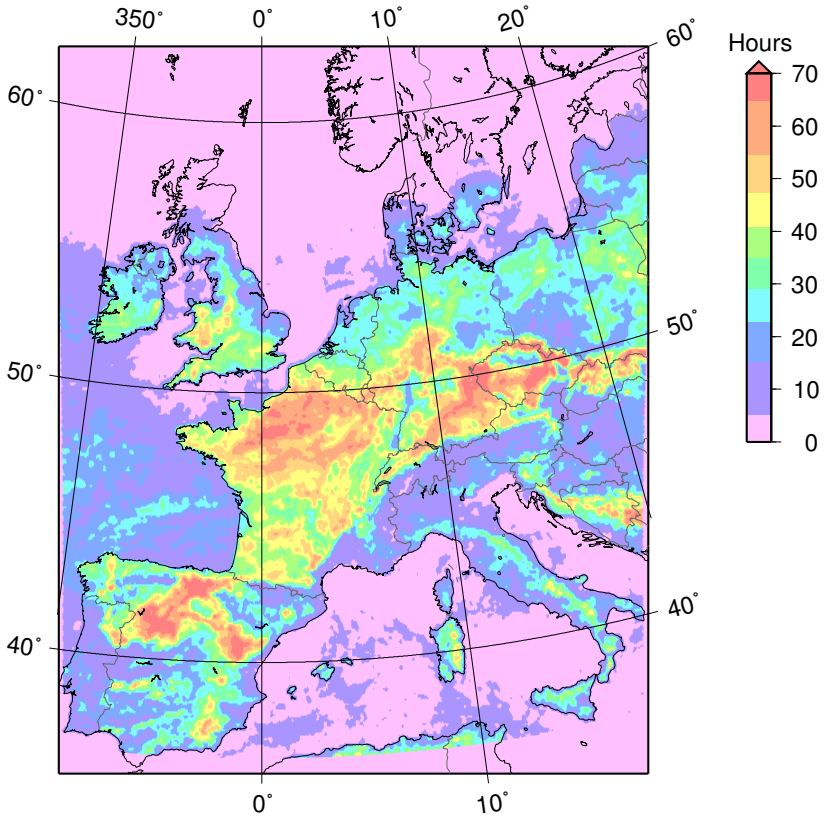

Figure 6.2: *Hours with daytime ground fog in the study area, December 2004, based on 1665 scenes (31 days).*

Although data for only one month is considered here, some very plausible patterns can be observed in figure 6.2. According to this map, in December 2004 ground fog occurrence was high in the fog-prone regions of northern France, the mountainous and elevated areas of Spain, Germany and the Czech Republic, along the Carpatians and in the Swiss Mittelland. Regions at lower elevations, such as the Netherlands, northern Germany and the Polish plains had a lower number of ground fog hours.

Along the coasts, especially the Atlantic coast of France, low stratus frequently turns to ground fog as it drifts onto varied terrain, as in the Bretagne. This process is clearly visible in the map; the transition is very obvious in the low-relief areas of the Netherlands and northern Germany. The very rare occurrence of ground fog in the northern part of the map (5 hours or less) is due to a seasonal limitation: in December, solar elevations in

the north are low and the daytime fog detection algorithm (with a minimum solar zenith angle of 80°) is not applicable for prolonged periods of the day.

Figure 6.3 is a clipping from figure 6.2 and highlights the general patterns for an area focused on Germany and neighbouring countries. Again, the most important ground fog areas in December 2004 were the mountainous regions, most prominently the Swabian and Frankish Alb, Fichtel Hills, Upper Palatinate Forest, Ore Mountains and Giant Mountains. Northern Germany experienced much less daytime ground fog in this month, as did the large basins and valleys of the Rhine and Main rivers. The Swiss Mittelland, well-known for frequent fog occurrence, displays a high number of daytime ground fog hours in December 2004 as well.

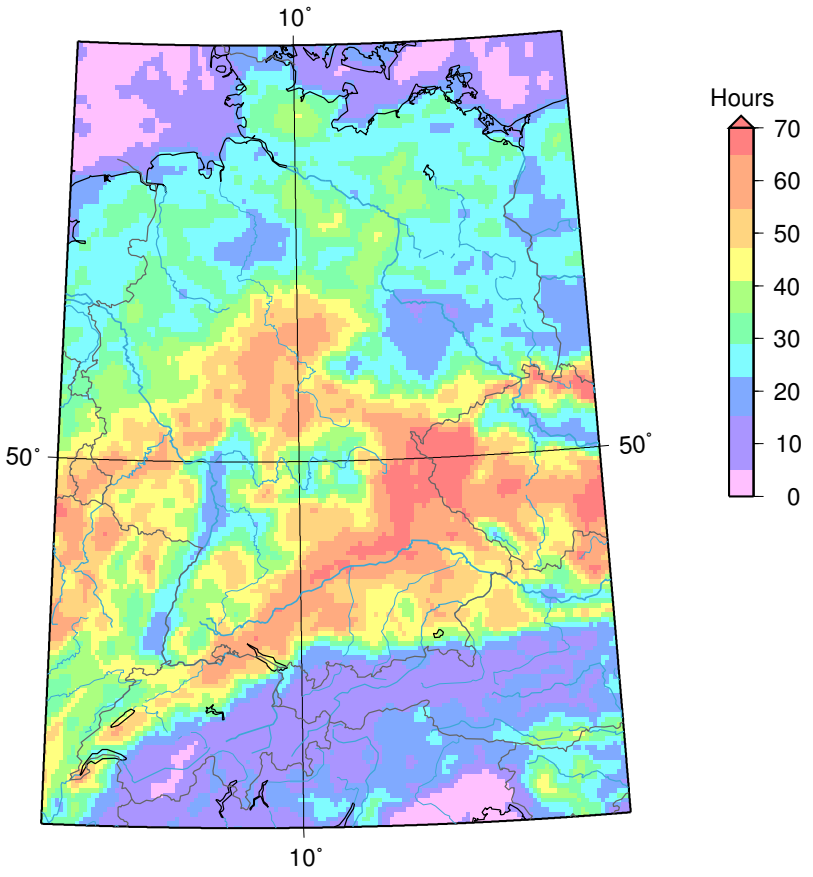

Figure 6.3: *Hours with daytime ground fog in and around Germany, December 2004, based on 1665 scenes (31 days).*

In the previous chapter, the applicability and reliability of the new scheme, and the feasibility of objective and automated satellite-based fog

detection have been shown. The maps presented in this chapter give an outlook on the potential of the new technique for climatological studies. Using the scheme introduced in this study, valuable climatological information not available from any other source can now easily be obtained.

Since SOFOS foots on spectral channels also available on many polar orbiting systems, such as TERRA/AQUA MODIS, the transfer of the new technique to other platforms will be easy to achieve. On top of the temporal potential the methodology unfolds on MSG SEVIRI, a portage of this kind will provide case studies at even higher spatial resolutions (1 km for MODIS). This perspective further expands the range of potential applications for SOFOS and will be of significant use in areas not covered by MSG SEVIRI.

Zusammenfassung

Informationen über die raum-zeitliche Verteilung von Nebel sind von großem Nutzen für Klimatologie, Verkehrssicherheit und Lufthygiene. Bislang existierte jedoch keine Methode zur räumlich und zeitlich hochaufgelösten Erfassung und Beobachtung von Nebelflächen. Wetterstationsmessungen liefern nicht die notwendige räumliche Auflösung, und ihre Interpolation hat sich als nicht praktikabel erwiesen. Satellitengestützte Verfahren waren bislang aufgrund spektraler Einschränkungen nur auf Polarorbiter-Systemen verfügbar und damit nur in schlechter zeitlicher Auflösung. Weiterhin war die objektive satellitengestützte Nebelerkennung tagsüber ein ungelöstes Problem. Operationell einsetzbare Techniken existierten nur für die Nacht.

Das zentrale Ziel der vorliegenden Studie war daher die Entwicklung einer neuen Methode zur operationellen Erkennung von Nebel am Tag, basierend auf geostationären Satellitendaten. Diese neu entwickelte Methode trägt den Namen *Satellite-based Operational Fog Observation Scheme* (SOFOS).

Seit 2003 steht mit Meteosat Second Generation (MSG) Spinning-Enhanced Visible and Infrared Imager (SEVIRI) ein geostationäres System mit deutlich verbesserter spektraler und räumlicher Auflösung zur Verfügung. Die Hauptthese dieser Arbeit war, dass die operationelle Nebelerkennung am Tag auf Grundlage dieses Systems möglich ist. Der zur Untersuchung dieser These gewählte Ansatz beruht auf drei Hypothesen:

1. Es ist möglich, Nebel durch implizite wie explizite Identifikation physikalischer und räumlicher Nebeleigenschaften abzugrenzen.

2. Die Erkennung von Bodennebel kann auf Basis geometrischer Wolkenparameter erfolgen, also durch die Ermittlung von Wolkendicke und Wolkenhöhe und den Vergleich dieser mit einem Geländemodell.

3. Die oben genannten Kriterien sind als Grundlage für die automatisierte, objektive Nebelerkennung in jedem beliebigen unbekannten Datensatz ausreichend belastbar.

Die Untersuchung dieser Hypothesen erforderte die Entwicklung einer völlig neuen Methodik, bestehend aus einer großen Vielfalt neuer und innovativer Algorithmen und Ansätze. Die erfolgreiche Entwicklung und Umsetzung dieser Technik bestand aus drei Schritten:

1. Eine neue Methode zur Abgrenzung sehr niedriger Stratuswolken wurde entwickelt. Diese Technik basiert auf der Annahme, dass sowohl Bodennebel als auch angehobener Nebel als sehr niedrige Stratuswolken angesprochen werden können. Eine Reihe von spektralen und räumlichen Einzeltests wurde entwickelt, um verschiedene Nebeleigenschaften zu identifizieren und so eine Abgrenzung von Nebel und sehr niedrigem Stratus von konkurrierenden Oberflächen wie wolkenfreien Regionen und anderen Wolken zu erreichen. Die spektralen Tests werden eingesetzt, um eine grobe Trennung von bewölkten und wolkenfreien Flächen zu erzielen, sowie um einige Wolkentypen, die nicht Nebel sein können, explizit auszuschließen. Diese spektralen Tests sind zum Großteil Neuentwicklungen, andere mussten an die speziellen Anforderungen des SEVIRI-Systems angepasst werden. Im zweiten Teil des Verfahrens werden mithilfe eines neu entwickelten, innovativen Ansatzes auf Basis räumlich zusammenhängender und diskreter Wolkenentitäten sehr niedrige und stratiforme Wolkenbereiche identifiziert.

2. Die Erkennung von Bodennebel wird mithilfe einer neu entwickelten Methode zur Bestimmung der Geometrie sehr niedriger Stratuswolken vorgenommen. Wenn die Basis einer Wolke lokal mit der Geländehöhe übereinstimmt wird Bodennebel angenommen. Die Wolkenbasishöhe kann nicht direkt ermittelt werden, sie ergibt sich jedoch aus der Differenz von Wolkenobergrenzhöhe und Wolkendicke. Daher wurden Techniken zur Bestimmung dieser beiden Größen entwickelt und umgesetzt. Die Wolkenobergrenzhöhe wird mithilfe einer deutlich verbesserten Version einer Wolkenrandhöhen-Interpolationsmethode bestimmt. Zur Bestimmung der Wolkendicke wurde ein neues Wolkenprofilmodell entwickelt. Dieses basiert auf einem mikrophysikalischen Wolkenmodell, in dem unter Berücksichtigung von Wolkenhöhe und -temperatur die Flüssigwasserverteilung innerhalb einer stratiformen Grenzschichtwolke simuliert wird. Die Beziehungzwischen Wolkenobergrenzhöhe, berechneter Wolkenbasishöhe und Geländehöhe wird zur Ermittlung eines Bodennebel-Konfidenzindikators herangezogen. Mit diesem Indikator wird eine Aussage über die Wahrscheinlichkeit von Bodennebel getroffen.

3. Als operationeller Rahmen für die Nah-Echtzeit-Prozessierung der Meteosat-SEVIRI-Daten und die Produktberechnung wurde das FMet-Programm (Framework for Meteosat data processing) entwickelt. Dieses dient vier verschiedenen Zwecken:

   - ankommende Satelliten-Rohdaten zu verarbeiten und sie in eine von den nachfolgenden Algorithmen verwertbare Form zu überführen. Dies beinhaltet Bildkalibrierung, Geometrieberechnung und regionale Zuschnitte.
   - den nachfolgenden Nebelalgorithmen eine Reihe von neu entwickelten und angepassten Hilfsprodukten zur Verfügung zu stellen. Die wichtigsten dieser Produkte sind Hintergrundreflexion, Niederschlagsverfügbares Wasser und Oberflächentemperatur.
   - einen Rahmen für die Implementierung der Nebelerkennungsalgorithmen zur Verfügung zu stellen.
   - der Nachprozessierung der Produkte inklusive Archivierung, Formatumwandlung und Projekten.

   FMet wurde diesen Anforderungen gemäß entwickelt und auf Standard-PCs implementiert.

Das Nebelerkennungsverfahren wurde in einer umfangreichen Studie mithilfe von METAR-Daten (Meteorological Aerodrome Reports) validiert. Die Erkennung von sehr niedrigen Wolken und Bodennebel wurde einzeln untersucht. Beide Produkte erwiesen sich als ausgesprochen stabil und zuverlässig. Die in der Validierungsstudie betrachtete Region umfasst West- und Mitteleuropa mit Land- und Seeflächen und repräsentiert somit eine große Vielfalt sehr verschiedener Nebelbildungsbedingungen. Da hier keine wesentlichen regionalen Unterschiede in der Algorithmuszuverlässigkeit festgestellt werden konnten und da die Methode auch nicht auf regional spezifischen Annahmen fußt, kann die Übertragbarkeit des neuen Verfahrens auf andere Regionen angenommen werden.

Auf Basis der Validierungsstudie konnten die Anfangshypothesen nicht falsifiziert werden und sollten somit angenommen werden: Nebelerkennung ist mit dem neuen Verfahren möglich, das die Abgrenzung von sehr niedrigen stratiformen Wolken und Wolkengeometrieinformationen in einem operationellen Rahmen zusammenfasst. Es ist somit ein neuer objektiver und verlässlicher Ansatz gefunden, um die Defizite vorheriger Methoden, sowohl auf Satelliten- als auch auf anderer Basis, zu überwinden.

Die operationelle Nebelerkennung in Nah-Echtzeit ist damit in einer räumlich angemessenen Dimension erstmals möglich geworden. Damit eröffnen sich viele neue Perspektiven. Potentielle Anwendungen beinhalten:

- die Beobachtung der räumlichen Nebelentwicklung in Nah-Echtzeit, mit positiven Auswirkungen auf kurzfristige Entscheidungen zur Verbesserung der Verkehrssicherheit.
- die Verbesserung von Luftqualitätsmonitoring und Nebelvorhersagen.
- statistische Auswertung der Häufigkeit und Dynamik von niedrigen Stratuswolken als Grundlage für die Quantifizierung klimatologischer Effekte.

Für all diese Anwendungen stellt das neue Verfahren Informationen von außerordentlichem Wert bereit, die zuvor aus keiner anderen Quelle verfügbar waren.

Bibliography

Ahn, M.-H., E.-H. Sohn & B.-J. Hwang (2003), A new algorithm for sea fog/stratus detection using GMS-5 data, *Advances in Atmospheric Sciences*, *20*: 899–913.

Alblas, R. (2006), Xrit2pic software manual, *Tech. rep.*.

Allam, R. (1987), The detection of fog from satellites, in *Proceedings of a Workshop on Satellite and Radar Imagery Interpretation*, 495–505.

Aminou, D. M. A. (2002), MSG's SEVIRI instrument, *ESA Bulletin*, *111*: 15–17.

Aminou, D. M. A., A. Ottenbacher, B. Jacquet & A. Kassighian (1999), Meteosat Second Generation: On-ground calibration, characterisation and sensitivity analysis of SEVIRI imaging radiometer, *Tech. rep.*, European Space Agency.

Andre, P., C. A. Silva, E. Balocco, J.-J. Boreux, V. Cavallo, M. Colomb, J. Dore, J. Dufour, J. Hannay, K. Hirech, N. Kelly, P. Lacote & L. Mealares (2004), The main results of a European research project: "Improvement of transport safety by control of fog production in a chamber" ("FOG"), in *Proceedings of the Third International Conference on Fog, Fog Collection and Dew*, C60.

Antonelli, P., S. A. Ackerman, W. P. Menzel, A. Huang, B. A. Baum & W. L. Smith (2002), Retrieval of cloud top height, effective emissivity, and particle size, from aircraft high spectral resolution infrared measurements, *Remote Sensing of Clouds and the Atmosphere VI*, *4539*: 50–61.

Baker, M. B. (1997), Cloud microphysics and climate, *Science*, *276*: 1072–1078.

Baldwin, M. E. & J. S. Kain (2004), Examining the sensitivity of various performance measures, in *Proceedings of the 17th Conference on Probability and Statistics in the Atmospheric Sciences*, 2.9.1 – 2.9.8, American Meteorological Society, Seattle, Washington, USA.

Bendix, J. (1995), A case study on the determination of fog optical depth and liquid water path using AVHRR data and relations to fog liquid water content and horizontal visibility, *International Journal of Remote Sensing*, *16*: 515–530.

Bendix, J. (1998), *Ein neuer Methodenverbund zur Erfassung der klimatologisch-lufthygienischen Situation von Nordrhein-Westfalen*, vol. 98 of *Bonner Geographische Abhandlungen*.

Bendix, J. (2001a), A 10-years fog climatology of Germany and the alpine region based on satellite data - preliminary results, in *Proceedings of the 2nd International Conference on fog and fog collection*, 357–360, St. John's, Canada.

Bendix, J. (2001b), A fog climatology of Germany and the alpine region based on AVHRR data, in *Proceedings of the 2001 EUMETSAT Meteorological Satellite Data Users' Conference*, 414–419, Antalya, Turkey.

Bendix, J. (2002), A satellite-based climatology of fog and low-level stratus in Germany and adjacent areas, *Atmospheric Research*, *64*: 3–18.

Bendix, J. (2004), *Geländeklimatologie*, Bornträger, Stuttgart, Germany.

Bendix, J. & M. Bachmann (1991), Ein operationell einsetzbares Verfahren zur Nebelerkennung auf der Basis von AVHRR-Daten der NOAA-Satelliten, *Meteorologische Rundschau*, *43*: 169–178.

Bendix, J., C. Reudenbach & R. Rollenbeck (2003), The Marburg Satellite Station, in *Proceedings of the 2002 EUMETSAT Meteorological Satellite Data Users' Conference*, 139–146, EUMETSAT, Dublin, Ireland.

Bendix, J., B. Thies, J. Cermak & T. Nauss (2005), Ground fog detection from space based on MODIS daytime data - a feasibility study, *Weather and Forecasting*, *20*: 989–1005.

Best, A. C. (1951), Drop-size distribution in cloud and fog, *Quarterly Journal of the Royal Meteorological Society*, *77*: 418–426.

Betts, A. K. (1982), Cloud thermodynamic models in saturation point coordinates, *Journal of the Atmospheric Sciences*, *39*: 2182–2191.

Betts, A. K. (1985), Mixing line analysis of clouds and cloudy boundary layers, *Journal of the Atmospheric Sciences*, *42*: 2751–2763.

Betts, A. K. & R. Boers (1990), A cloudiness transition in a marine boundary layer, *Journal of the Atmospheric Sciences*, *47*: 1480–1497.

Billing, H., I. Haupt, E. Hilt & D. Koslowsky (1980), Wolkenklassifikation aufgrund von Satellitendaten, *Annalen der Meteorologie*, *15*: 145–146.

Boers, R. & A. K. Betts (1988), Saturation point structure of marine stratocumulus clouds, *Journal of the Atmospheric Sciences*, *45*: 1156–1175.

Boers, R., S. H. Melfi & S. P. Palm (1991), Cold-air outbreak during GALE: Lidar observations and modeling of boundary layer dynamics, *Monthly Weather Review*, *119*: 1132–1150.

Boers, R. & R. M. Mitchell (1994), Absorption feedback in stratocumulus clouds – influence on cloud top albedo, *Tellus*, *A46*: 229–241.

Bott, A., U. Sievers & W. Zdunkowski (1990), A radiation fog model with a detailed treatment of the interaction between radiative transfer and fog microphysics, *Journal of the Atmospheric Sciences*, *47*: 2153–2166.

Brenguier, J.-L. (1991), Parameterization of the condensation process: A theoretical approach, *Journal of the Atmospheric Sciences*, *48*: 264–282.

Brenguier, J.-L., H. Pawlowska & L. Schüller (2003), Cloud microphysical and radiative properties for parameterization and satellite monitoring of the indirect effect of aerosol on climate, *Journal of Geophysical Research*, *108*: CMP 6–1–CMP 6–14.

Brenguier, J.-L., H. Pawlowska, L. Schüller, R. Preusker & J. Fischer (2000), Radiative properties of boundary layer clouds: droplet effective radius versus number concentration, *Journal of the Atmospheric Sciences*, *57*: 803–821.

Briggs, W. M. & D. Ruppert (2004), Assessing the skill of yes/no forecasts for Markov observations, in *Proceedings of the 17th Conference on Probability and Statistics in the Atmospheric Sciences*, 1–20, American Meteorological Society, Seattle, Washington, USA.

Brooks, H. E. & C. A. I. Doswell (1996), A comparison of measures-oriented and distributions-oriented approaches to forecast verification, *Weather and Forecasting*, *11*: 288–303.

Brown, R. & W. T. Roach (1976), The physics of radiation fog: II – A numerical study, *Quarterly Journal of the Royal Meteorological Society*, *102*: 335–354.

Brown, R. & W. T. Roach (2004), Radiation fog and steam fog, *Weather*, *59*: 25–26.

Browning, K. (ed.) (1982), *Nowcasting*, Academic Press, London, UK.

Campbell, G. & K. Holmlund (2004), Geometric cloud heights from Meteosat, *International Journal of Remote Sensing*, *25*: 4505–4519.

Caughey, S. J., B. A. Crease & W. T. Roach (1982), A field study of nocturnal stratocumulus: II – Turbulence structure and entrainment, *Quarterly Journal of the Royal Meteorological Society*, *108*: 125–144.

Cermak, J. & J. Bendix (2006), A novel approach to fog/low stratus detection using Meteosat 8 data, *Atmospheric Research*, accepted.

Cermak, J., M. Schneebeli, D. Nowak, L. Vuilleumier & J. Bendix (2006), Characterization of low clouds with satellite and ground-based remote sensing systems, *Meteorologische Zeitschrift*, *15*: 65–72.

Cermak, J., B. Thies & J. Bendix (2004), A new approach to fog detection using SEVIRI and MODIS data, in *Proceedings of the 2004 EUMETSAT Meteorological Satellite Conference*, 130–136, EUMETSAT, Weimar, Germany.

CGMS (1999), LRIT/HRIT global specification, *CGMS 03*, Coordination Group for Meteorological Satellites (CGMS).

Chang, F.-L. & Z. Li (2002a), A bi-spectral near-infrared method for inferring the vertical variation of cloud droplet effective radius, in *Proceedings of the 11th Conference on Cloud Physics*, JP1.8.1–JP1.8.4, Ogden, UT, USA.

Chang, F.-L. & Z. Li (2002b), Estimating the vertical variation of cloud droplet effective radius using multispectral near-infrared satellite measurements, *Journal of Geophysical Research*, *107*: AAC 7–1–AAC 7–12.

Chang, F.-L. & Z. Li (2003), Retrieving vertical profiles of water-cloud droplet effective radius: Algorithm modification and preliminary application, *Journal of Geophysical Research*, *108*: AAC3–1–AAC3–11.

Chesters, D., L. W. Uccellini & W. D. Robinson (1983), Low-level water vapor fields from the VISSR atmospheric sounder (VAS) "split window"channels, *Journal of Applied Meteorology*, *22*: 725–743.

Chesters, S., W. D. Robinson & L. W. Uccellini (1987), Optimized retrievals of precipitable water from the VAS "split window", *Journal of Applied Meteorology*, *26*: 1059–1066.

Choudhury, B. J., T. J. Dorman & A. Y. Hsu (1995), Modeled and observed relations between the AVHRR split window temperature difference and atmospheric precipitable water over land surfaces, *Remote Sensing of Environment*, *51*: 281–290.

Chylek, P. (1978), Extinction and liquid water content of fogs and clouds, *Journal of the Atmospheric Sciences*, *35*: 296–300.

Clerbaux, N., C. Bertrand, D. Caprion, B. Depaepe, S. Dewitte, L. Gonzales & A. Ipe (2006), Narrowband-to-broadband conversions for SEVIRI, in *Proceedings of the 2005 EUMETSAT Meteorological Satellite Conference*, Dubrovnik, Croatia.

D'Entremont, R. & L. Thomason (1987), Interpreting meteorological satellite images using a color-composite technique, *Bulletin of the American Meteorological Society*, *68*: 762–768.

Derrien, M., B. Farki, L. Harang, H. LeGleau, A. Noyalet, D. Pochic & A. Sairouni (1993), Automatic cloud detection applied to NOAA-11 / AVHRR imagery, *Remote Sensing of Environment*, *46*: 246–267.

Doswell, C. A. I., R. Davies-Jones & D. L. Keller (1990), On summary measures of skill in rare event forecasting based on contingency tables, *Weather and Forecasting*, *5*: 576–585.

Dozier, J. (1989), Spectral signature of alpine snow cover from the Landsat Thematic Mapper, *Remote Sensing of Environment*, *28*: 9–22.

Dozier, J. & T. H. Painter (2004), Multispectral and hyperspectral remote sensing of alpine snow properties, *Annual Review of Earth and Planetary Sciences*, *32*: 465–494.

Driedonks, A. G. M. & P. G. Duynkerke (1989), Current problems in the stratocumulus-topped atmospheric boundary layer, *Boundary Layer Meteorology*, *46*: 275–303.

Duda, D. P., G. L. Stephens, B. Stevens & W. R. Cotton (1996), Effects of aerosol and horizontal inhomogeneity on the broadband albedo of marine stratus: Numerical simulations, *Journal of the Atmospheric Sciences*, *53*: 3757–3769.

Durand, P. & T. Bourcy (2001), Observations of the turbulence structure within two stratocumulus-topped marine boundary layers, *Boundary Layer Meteorology*, *99*: 105–125.

Dyras, I. (2000), The feasibility of 1.6 μm channel on NOAA-15 use for operational fog detection, in *Proceedings of the 2000 EUMETSAT Meteorological Satellite Data Users' Conference*, 773–777, Bologna, Italy.

Ellrod, G. P. (1995), Advances in the detection and analysis of fog at night using goes multispectral infrared imagery, *Weather & Forecasting*, *10*: 606–619.

Ellrod, G. P. (2002), Estimation of low cloud base heights at night from satellite infrared and surface temperature data, *National Weather Digest*, *26*: 39–44.

EUMETSAT (2001), Meteosat Second Generation – system overview, *Technical Description 07*, EUMETSAT.

EUMETSAT (2003), MSG - image data dissemination service, *Technical Description 08*, EUMETSAT.

EUMETSAT (2004), EUMETCast - EUMETSAT's broadcast system for environmental data, *Technical Description 15*, EUMETSAT.

EUMETSAT (2005a), MSG ground segment LRIT/HRIT mission specific implementation, *EUM/MSG/SPE 057*, EUMETSAT.

EUMETSAT (2005b), MSG level 1.5 image data format description, *EUM/MSG/ICD 105*, EUMETSAT.

Eyre, J. R., J. L. Brownscombe & R. J. Allam (1984), Detection of fog at night using Advanced Very High Resolution Radiometer (AVHRR) imagery, *Meteorological Magazine*, *113*: 266–271.

Findlater, J. (1985), Field investigations of radiation fog formation at outstations, *Meteorological Magazine*, *114*: 187–201.

Fischer, J., W. Cordes, A. Schmitz-Peiffer, W. Renger & P. Mörl (1991), Detection of cloud-top height from backscattered radiances within the oxygen A band. Part 2: Measurements, *Journal of Applied Meteorology*, *30*: 1260–1267.

Fischer, J. & H. Grassl (1991), Detection of cloud-top height from backscattered radiances within the oxygen A band. Part 1: theoretical study, *Journal of Applied Meteorology*, *30*: 1245–1259.

Fischer, J., R. Preusker & C. Rathke (2003), Cloud top pressure from geo-stationary satellite observations in the oxygen A-band, *Tech. Rep. EUM/CO/02/1014/SAT*, EUMETSAT.

Fitzjarrald, D. R. & G. G. Lala (1989), Hudson valley fog environments, *Journal of Applied Meteorology*, *28*: 1303–1328.

Flossmann, A. I. (1998), Clouds and pollution, *Pure and Applied Chemistry*, *17*: 1345–1352.

Fowler, T. L., J. T. Braid & A. Holmes (2004), Selecting METARs to verify ceiling and visibility forecasts, in *Proceedings of the 17th Conference on Probability and Statistics in the Atmospheric Sciences*, 2.4.1–2.4.5, American Meteorological Society, Seattle, Washington, USA.

Frey, R. A., B. A. Baum, W. P. Menzel, S. A. Ackerman, C. C. Moeller & J. D. Spinhirne (2003), A comparison of cloud top heights computed from airborne lidar and mas radiance data using CO2 slicing, *Journal of Geophysical Research*, *104*: 24547–24555.

Fu, Q. & K. N. Liou (1993), Parameterization of the radiative properties of cirrus clouds, *Journal of the Atmospheric Sciences*, *51*: 2008–2025.

Fuzzi, S., R. A. Castillo, J. E. Jiusto & G. G. Lala (1984), Chemical-composition of radiation fog water at Albany, New-York, and its relationship to fog microphysics, *Journal of Geophysical Research*, *89*: 7159–7164.

Gao, B. C. & Y. J. Kaufman (1997), MODIS total precipitable water, in Wharton, S. W. & M. F. Myers (eds.), *MTPE EOS Data Products Handbook*, 93–94, NASA Goddard Space Flight Center, Greenbelt, Maryland, USA.

Genio, A. D. D. & A. B. Wolf (2000), The temperature dependence of the liquid water path of low clouds in the southern Great Plains, *Journal of Climate*, *13*: 3465–3486.

Gerber, H. (1981), Microstructure of a radiation fog, *Journal of the Atmospheric Sciences*, *38*: 454–458.

Glickman, T. S. (ed.) (2000), *Glossary of Meteorology*, American Meteorological Society (AMS), Boston, USA.

Goody, R. (1995), *Principles of Atmospheric Physics and Chemistry*, Oxford University Press, New York, USA.

Greenwald, T. J. & S. A. Christopher (2000), The GOES I-M imagers: New tools for studying microphysical properties of boundary layer stratiform clouds, *Bulletin of the American Meteorological Society*, *81*: 2607–2620.

Güls, I. & J. Bendix (1996), Fog detection and fog mapping using low cost Meteosat-WEFAX transmission, *Meteorological Applications*, *3*: 179–187.

Gultepe, I. & G. A. Isaac (1997), Liquid water content and temperature relationship from aircraft observations and its applicability to GCMs, *Journal of Climate*, *10*: 446–452.

Hadamard, J. (1923), *Lectures on Cauchy's Problem in Linear Partial Differential Equations*, Yale University Press, New Haven, USA.

Hall, D., G. Riggs & V. Salomonson (2001), Algorithm theoretical basis document (ATBD) for the MODIS snow and sea ice-mapping algorithms, *Tech. rep.*.

Hansen, J. E. & L. D. Travis (1974), Light scattering in planetary atmospheres, *Space Science Reviews*, *16*: 527–610.

Harries, J. & D. Crommelynck (1999), The Geostationary Earth Radiation Budget experiment on MSG-1 and its potential applications, *Advances in Space Research*, *24*: 915–919.

Hayasaka, T., T. Nakajima, Y. Fujiyoshi, Y. Ishizaka, T. Takeda & M. Tanaka (1995), Geometrical thickness, liquid water-content, and radiative properties of stratocumulus clouds over the western north pacific, *Journal of Applied Meteorology*, *34*: 460–470.

Heidinger, A. K. & G. L. Stephens (2000), Molecular line absorption in a scattering atmosphere. part II: Application to remote sensing in the O2 A band, *Journal of the Atmospheric Sciences*, *57*: 1615–1634.

Heintzenberg, J., M. Wendisch, B. Yuskiewicz, D. Orsini, A. Wiedensohler, F. Stratmann, G. Frank, B. G. Martinsson, D. Schell, S. Fuzzi & G. Orsi (1998), Characteristics of haze, mist and fog, *Beiträge zur Physik der Atmosphäre*, *71*: 21–31.

Henning, S., T. Rosenorn, B. D'Anna, A. A. Gola, B. Svenningsson & M. Bilde (2005), Cloud droplet activation and surface tension of mixtures of slightly soluble organics and inorganic salt, *Atmospheric Chemistry and Physics*, *5*: 575–582.

Hess, M., P. Koepke & U. Schult (1998), Optical properties of aerosols and clouds: The software package OPAC, *Bulletin of the American Meteorological Society*, *79*: 831–844.

Hillger, D. W. & S. Q. Kidder (2003), A simple GOES skin temperature product, in *Proceedings of the 12th Conference on Satellite Meteorology and Oceanography*, P2.5–1–P2.5–4, Long Beach, California, USA.

Hoffmann, H.-E. & R. Roth (1989), Cloud physical parameters in dependence on height above cloud base in different clouds, *Meteorological and Atmospheric Physics*, *41*: 247–254.

Holets, S. & R. N. Swanson (1981), High-inversion fog episodes in central California, *Journal of Applied Meteorology*, *20*: 890–899.

Houghton, J. T., Y. Ding, D. J. Griggs, M. Noguer, P. J. van der Linden, X. Dai, K. Maskel & C. A. Johnson (eds.) (2001), *Climate Change 2001: The Scientific Basis*, Cambridge University Press, Cambridge, UK.

Houze, R. A. (1993), *Cloud Dynamics*, vol. 53 of *International Geophysics Series*, Academic Press, San Diego.

Hu, Y. X. & K. Stamnes (1993), An accurate parameterization of the radiative properties of water clouds suitable for use in climate models, *Journal of Climate*, *6*: 728–742.

Hunt, G. E. (1973), Radiative properties of terrestrial clouds at visible and infra-red thermal window wavelengths, *Quarterly Journal of the Royal Meteorological Society*, *99*: 346–369.

Hutchison, K. D. (2002), The retrieval of cloud base heights from MODIS and three-dimensional cloud fields from NASA's EOS Aqua mission, *International Journal of Remote Sensing*, *23*: 5249–5265.

INM (2005), Software user manual for the PGE06 of the SAFNWC / MSG: Scientific part, *Tech. rep.*, Instituto Nacional de Meteorologia.

Inoue, T. (1985), On the temperature and effective emissivity determination of semi-transparent cirrus clouds by bi-spectral measurements in the 10-μm window region, *Journal of the Meteorological Society of Japan*, *63*: 88–99.

Iwabuchi, H. & T. Hayasaka (2003), A multi-spectral non-local method for retrieval of boundary layer cloud properties from optical remote sensing data, *Remote Sensing of Environment*, *88*: 249–308.

Jacobs, W., V. Nietosvaara, S. C. Michaelides & H. Gmoser (eds.) (2005), *Short-range forecasting methods of fog, visibility and low clouds – COST action 722 phase I report*, Office for Official Publications of the European Communities.

Jaeschke, W., J. P. Dierssen, A. Günther, W. Schickedanz, A. Wolf, L. Ricci & B. G. Arends (1998), Mass fluxes and chemical pathways during a fog event, *Beiträge zur Physik der Atmosphäre*, *71*: 145–157.

Karlsson, K.-G. (1989), Development of an operational cloud classification model, *International Journal of Remote Sensing*, *10*: 687–693.

Kawamoto, K., T. Nakajima & T. Y. Nakajima (2001), A global determination of cloud microphysics with AVHRR remote sensing, *Journal of Climate*, *14*: 2054–2068.

Kerr, Y. H., J. P. Lagouarde & J. Imbernon (1992), Accurate land surface temperature retrieval from AVHRR data with use of an improved split window algorithm, *Remote Sensing of Environment*, *41*: 197–209.

Key, J. & A. J. Schweiger (1998), Tools for atmospheric radiative transfer: Streamer and FluxNet, *Computers and Geosciences*, *24*: 443–451.

Kietzig, E. (1991), Automatische Wolkenklassifizierung in Meteosat-Bildern mittels Bildmustererkennung unter Berücksichtigung von a-priori-Wissen, *Meteorologische Rundschau*, *43*: 42–58.

King, M. D. (1987), Determination of the scaled optical thickness of clouds from reflected solar radiation measurements, *Journal of the Atmospheric Sciences*, *44*: 1734–1751.

King, M. D., Y. J. Kaufman, W. P. Menzel & D. Tanré (1992), Remote sensing of cloud, aerosol, and water vapor properties from the moderate resolution imaging spectrometer (MODIS), *IEEE Transactions on Geoscience and Remote Sensing*, *30*: 2–27.

Kneizys, F. X., E. P. Shettle, L. W. Abreu, J. H. Chetwynd, G. P. Anderson, W. O. Gallery, J. E. A. Selby & S. A. Clough (1988), Users guide to LOWTRAN7, *Environmental Research Papers 1010, AFGL-TR-88-0177*, Air Force Geophysics Laboratory, Hanscom AFB, Massachusetts, USA.

Koelemeijer, R. B. A., P. Stammes, J. W. Hovenier & J. F. de Haan (2001), A fast method for retrieval of cloud parameters using oxygen a band measurements from the global ozone monitoring experiment, *Journal of Geophysical Research*, *106*: 3475–3490.

Köhler, H. (1936), The nucleus in and the growth of hygroscopic droplets, *Transactions of the Faraday Society*, *32*: 1152–1161.

Kokhanovsky, A. A. (2003), *Light scattering media optics – Problems and solutions*, Springer, Berlin, Heidelberg, New York, 3rd edn.

Kokhanovsky, A. A., W. v. Hoyningen-Huene, V. V. Rozanov, S. Noel, K. Gerilowski, H. Bovensmann, K. Bramstedt, M. Buchwitz & J. P. Burrows (2006), The semianalytical cloud retrieval algorithm for SCIAMACHY – II. The application to MERIS and SCIAMACHY data, *Atmospheric Chemistry and Physics Discussions*, *6*: 1813–1840.

Kokhanovsky, A. A. & V. V. Rozanov (2004), The physical parameterization of the top-of-atmosphere reflection function for a cloudy atmosphere -underlying surface system: the oxygen A-band case study, *Journal of Quantitative Spectroscopy and Radiative Transfer*, *85*: 35–55.

Kokhanovsky, A. A., V. V. Rozanov, T. Nauss, C. Reudenbach, J. S. Daniel, H. L. Miller & J. P. Burrows (2005), The semianalytical cloud retrieval algorithm for SCIAMACHY – I. The validation, *Atmospheric Chemistry and Physics Discussions*, *5*: 1995–2015.

Korolev, A. V., G. A. Isaac, I. P. Mazin & H. W. Barker (2001), Microphysical properties of continental clouds from in-situ measurements, *Quarterly Journal of the Royal Meteorological Society*, *127*: 2117–2151.

Kraus, H. & U. Ebel (1989), Atmospheric boundary layer characteristics in severe smog episodes, *Meteorological and Atmospheric Physics*, *40*: 211–224.

Kriebel, K.-T., G. Gesell, M. Kästner & H. Mannstein (2003), The cloud analysis tool APOLLO: Improvements and validations, *International Journal of Remote Sensing*, *24*: 2389–2408.

Kurosu, T. P., K. V. Chance & R. J. D. Spurr (1998), Cloud retrieval algorithm for the European Space Agency's Global Ozone Monitoring Experiment, *Satellite Remote Sensing of Clouds and the Atmosphere III*, *3495*: 17–26.

Kuze, A. & K. V. Chance (1994), Analysis of cloud top height and cloud coverage from satellites using the O2 A and B bands, *Journal of Geophysical Research*, *99*: 14481–14491.

Lee, T. E., F. J. Turk & K. Richardson (1997), Stratus and fog products using GOES-8-9 3.9-μm data, *Weather and Forecasting*, *12*: 664–677.

Leigh, R. J. (1995), Economic benefits of terminal aerodrome forecasts (TAFs) for Sydney airport, Australia, *Meteorological Applications*, *2*: 239–247.

Liang, S. (2001), Narrowband to broadband conversions of land surface albedo – I. algorithms, *Remote Sensing of Environment*, *76*: 213–238.

Liljas, E. (1981), An automated multispectral cloud classification technique for satellite imagery analysis, in *Proceedings of the Symposium on Current Problems of Weather Predictions*, Vienna, Austria.

Liljas, E. (1982), Automated techniques for the analysis of satellite cloud imagery, in Browning, K. A. (ed.), *Nowcasting*, chap. 3.2, 167–176, Academic Press, London, UK and New York, USA.

Lindner, T. H. & J. Li (2000), Parameterization of the optical properties for water clouds in the infrared, *Journal of Climate*, *13*: 1797–1805.

Liou, K. N. (2002), *An introduction to atmospheric radiation*, vol. 84 of *International Geophysics series*, Academic Press, London, UK and San Diego, USA.

Mahani, S. E., X. Gao, S. Sorooshian & B. Imam (2000), Estimating cloud top height and spatial displacement from scan-synchronous GOES images using simplified IR-based stereoscopic analysis, *Journal of Geophysical Research*, *105*: 15597–15608.

Manton, M. J. (1983), The physics of clouds in the atmosphere, *Reports on Progress in Physics*, *46*: 1393–1444.

Martin, G., D. Johnson & A. Spice (1994), The measurement and parameterization of effective radius and droplet in warm stratocumulus clouds, *Journal of the Atmospheric Sciences*, *51*: 1823–1842.

Marzban, C. (1998), Scalar measures of performance in rare-event situations, *Weather and Forecasting*, *13*: 753–763.

Marzban, C. (2004), The ROC curve and the area under it as performance measures, *Weather and Forecasting*, *19*: 1106–1114.

Masbou, M. & A. Bott (2006), LM_PAFOG: Three-dimensional fog forecasting with the Lokal-Modell, in *Proceedings of the COST722 workshop*, Langen, Germany.

Matveev, L. T. (1984), *Cloud Dynamics*, D. Reidel Publishing, Dordrecht.

McFarlane, N. A., G. J. Boer, J.-P. Blanchet & M. Lazare (1995), The Canadian Climate Centre second-generation general circulation model and its equilibrium climate, *Journal of Climate*, *5*: 1013–1044.

Menzel, P. & K. Strabala (1997), Cloud top properties and cloud phase (mod04), *Algorithm theoretical basis document*, NASA.

Meteo-France (2005), User manual for the PGE01-02-03 of the SAFNWC/MSG: Scientific part, *User manual SAF/NWC/IOP/MFL/SCI/SUM/01*, EUMETSAT SAFNWC.

Meyer, W. D. & G. V. Rao (1999), Radiation fog prediction using a simple numerical model, *Pure and Applied Geophysics*, *155*: 57–80.

Miles, N. L., J. Verlinde & E. E. Clothiaux (2000), Cloud droplet size distributions in low-level stratiform clouds, *Journal of the Atmospheric Sciences*, *57*: 295–311.

Minnis, P., P. W. Heck, D. F. Young, C. W. Fairall & J. B. Snider (1992), Stratocumulus cloud properties derived from simultaneous satellite and island-based instrumentation during FIRE, *Journal of Applied Meteorology*, *31*: 317–339.

Mueller, J., R. Stuhlmann, K. Dammann, R. Hollmann, J. E. Harries, S. Kellock, R. Mossavati, R. Wrigley, D. Crommelynck & S. Dewitte (1999), GERB: An earth radiation budget instrument on second generation Meteosat, *Advances in Space Research*, *24*: 921–924.

Muller, J.-P., R. Dundas & D. Bower (1999a), An automated processing system for cloud-top height and amount from ATSR(2) stereo, in *ATSR International Workshop on the Applications of the ERS Along Track Scanning Radiometer*, ESA, Frascati, Italy.

Muller, J.-P., R. Dundas & C. Vogt (1999b), Cloud-top height and cloud amount retrieval using digital stereo photogrammetry with ATSR and MISR, in *European Geophysical Society XXV General Assembly*, EGS, The Hague, Netherlands.

Müller, M. D. (2005), Development of a 1D ensemble forecast system with variational assimilation, in *Proceedings of the COST722 Mid-term workshop*, 25–33, Larnaka, Cyprus.

Munro, R., A. Ratier, J. Schmetz & D. Klaes (2002), Atmospheric measurements from the MSG and EPS systems, *Advances in Space Research*, *29*: 1609–1618.

Murphy, A. H. (1993), What is a good forecast? An essay on the nature of goodness in weather forecasting, *Weather and Forecasting*, *8*: 281–293.

Nakajima, T. & M. D. King (1990), Determination of the optical thickness and effective particle radius of clouds from reflected solar radiation measurements. part I: Theory, *Journal of the Atmospheric Sciences*, *47*: 1878–1893.

Nakajima, T., M. D. King, J. D. Spinhirne & L. F. Radke (1991), Determination of the optical thickness and effective particle radius of clouds from reflected solar radiation measurements. part II: Marine stratocumulus observations, *Journal of the Atmospheric Sciences*, *48*: 728–750.

Nakajima, T. & M. Tanaka (1986), Matrix formulations for the transfer of solar radiation in a plane-parallel scattering atmosphere, *Journal of Quantitative Spectroscopy and Radiative Transfer*, *35*: 13–21.

Nakajima, T. Y. & T. Nakajima (1995), Wide-area determination of cloud microphysical properties from NOAA AVHRR measurements for FIRE and ASTEX regions, *Journal of the Atmospheric Sciences*, *52*: 4043–4059.

Nauss, T., A. A. Kokhanovsky, T. Y. Nakajima, C. Reudenbach & J. Bendix (2005), The intercomparison of selected cloud retrieval algorithms, *Atmospheric Research*, *78*: 46–78.

Nauss, T., M. Wagner & J. Bendix (2004), Operational retrieval of microphysical properties for day- and night-time MSG/MODIS data, in *Proceedings of the 2003 EUMETSAT Meteorological Satellite Conference*, 281–285, EUMETSAT, Weimar, Germany.

Oke, T. R. (1987), *Boundary Layer Climates*, Methuen, London, 2nd edn.

Oliver, D. A., W. S. Lewellen & G. G. Williamson (1978), The interaction between turbulent and radiative transport in the development of fog and low-level stratus, *Journal of the Atmospheric Sciences*, *35*: 301–316.

Pagowski, M., I. Gultepe & P. King (2004), Analysis and modeling of an extremely dense fog event in southern ontario, *Journal of Applied Meteorology*, *43*: 3–16.

Pankiewicz, G. S. (1995), A neural network cloud classifier trained with AVHRR data for use on Meteosat imagery, in *Proceedings of the 1995 Meteorological Satellite Data Users' Conference*, 393–400, EUMETSAT, Winchester, United Kingdom.

Pankiewicz, G. S. (1997), New Meteosat pattern recognition products for use in weather forecasting, *Satellite Data Applications: Weather and Climate*, *19*: 443–446.

Park, H., P. F. Soulen & C. R. Prasad (1997), Novel spectrograph/radiometer for cloud top height measurement using three complementary techniques, *Sensors, Systems, and Next-Generation Satellites*, *3221*: 365–371.

Peres, L. F. & C. C. DaCamara (2003), An emissivity look-up table for LST estimations from MSG data, in *Proceedings of the Land Surface Analysis SAF Training Workshop*, 48–55, EUMETSAT, Lisbon, Portugal.

Pili, P. (2000), Overview of the SEVIRI instrument capabilities, in *Fourth EUMETSAT User Forum in Africa*, Fourth EUMETSAT User Forum in Africa, 1–12, EUMETSAT, Darmstadt, Germany.

Pinnick, R. G., D. L. Hoihjelle, G. Fernandez, E. B. Stenmark, J. D. Lindberg, G. B. Hoidale & S. G. Jennings (1978), Vertical

structure in atmospheric fog and haze and its effects on visible and infrared extinction, *Journal of the Atmospheric Sciences*, *35*: 2020–2032.

Pinnick, R. G., S. G. Jennings, P. Chylek & H. J. Auvermann (1979), Verification of a linear relation between IR extinction, absorption and liquid water content of fogs, *Journal of the Atmospheric Sciences*, *36*: 1577–1586.

Platnick, S. (2000), Vertical photon transport in cloud remote sensing problems, *Journal of Geophysical Research*, *105*: 22919–22935.

Poli, D., G. Seiz & M. Baltsavias (2000), Cloud-top height estimation from satellite stereopairs for weather forecasting and climate change analysis, *International Archive of Photogrammetry and Remote Sensing*, *XXXIII*.

Porcu, F. & V. Levizzani (1992), Cloud classification using Meteosat VIS-IR imagery, *International Journal of Remote Sensing*, *13*: 893–909.

Prata, A. J. & P. J. Turner (1997), Cloud-top height determination using ATSR data, *Remote Sensing of Environment*, *59*: 1–13.

Price, J. C. (1984), Land surface temperature measurements from the split window channels of the NOAA-7 Advanced Very High Resolution Radiometer, *Journal of Geophysical Research*, *89*: 7231–7237.

Prince, S. D., S. J. Goetz, R. O. Dubayah, K. P. Czajkowski & M. Thawley (1998), Inference of surface and air temperature, atmospheric precipitable water and vapor pressure deficit using Advanced Very High-Resolution Radiometer satellite observations: comparison with field observations, *Journal of Hydrology*, *212-213*: 230–249.

Pruppacher, H. R. & J. D. Klett (1997), *Microphysics of clouds and precipitation*, vol. 18 of *Atmospheric and oceanographic sciences library*, Kluwer, Dordrecht, Boston, London, 2nd edn.

Putsay, M., J. Kerényi, I. Szenyán, I. Sebok, P. Németh & M. Diószeghy (2001), Nighttime fog and low cloud detection in NOAA-16 AVHRR images and validation with ground observed SYNOP data and radar measurements, in *Proceedings of the 2001 EUMETSAT Meteorological Satellite Conference*, EUM P33, 365–373, EUMETSAT, Antalya, Turkey.

Randriamampianina, R., J. Nagy, T. Balogh & J. nyi (2000), Determination of cloud top height using meteorological satellite and radar data, *Physics and Chemistry of the Earth, Part B: Hydrology, Oceans and Atmosphere*, *25*: 1103–1106.

Reudenbach, C. & J. Bendix (1998), Experiments with a straightforward model for the spatial forecast of fog/low stratus clearance based on multisource data, *Meteorological Applications*, *5*: 205–216.

Reudenbach, C., T. Nauss, J. Cermak, M. Dobbermann, J. Bendix, W. Theissen, P. Scheidgen & O. Harmann (2004), An integrated receiving and processing unit for MSG, NOAA and Terra/Aqua data, in *Procceedings of the 2003 EUMETSAT Meteorological Satellite Conference*, 291–297, EUMETSAT, Weimar, Germany.

Reynolds, D. W. & T. H. von der Haar (1977), A bispectral method for cloud parameter determination, *Monthly Weather Review*, *105*: 1603–1603.

Roach, W. T. (1994), Back to basics: Fog: Part 1 - Definitions and basic physics, *Weather*, *49*: 411–415.

Roach, W. T. (1995), Back to basics: Fog: Part 2 - The formation and dissipation of land fog, *Weather*, *50*: 7–11.

Roach, W. T., R. Brown, S. J. Caughey, B. A. Crease & A. Slingo (1982), A field study of nocturnal stratocumulus: I – Mean structure and budgets, *Quarterly Journal of the Royal Meteorological Society*, *108*: 103–123.

Roach, W. T., R. Brown, S. J. Caughey, J. A. Garland & C. J. Readings (1976), The physics of radiation fog: I - A field study, *Quarterly Journal of the Royal Meteorological Society*, *102*: 313–333.

Rozanov, V. V. & A. A. Kokhanovsky (2004), Semianalytical cloud retrieval algorithm as applied to the cloud top altitude and the cloud geometrical thickness determination from top-of-atmosphere reflectance measurements in the oxygen A band, *Journal of Geophysical Research*, *109*.

Sandford, M. C. W., P. M. Allan, M. E. Caldwell, J. Delderfield, M. B. Oliver, E. Sawyer, J. E. Harries, J. Ashmall, H. Brindley & S. Kellock (2003), The geostationary Earth radiation budget (GERB)

instrument on EUMETSAT's MSG satellite, *Acta Astronautica*, *53*: 909–915.

Saunders, R. W. (1988), Cloud-top temperature/height: A high-resolution imagery product from AVHRR data, *Meteorological Magazine*, *117*: 211–221.

Saunders, R. W., S. English, P. Rayer, M. Matricardi, F. Chevallier, P. Brungel & G. Deblonde (2002), RTTOV-7: A satellite radiance simulator for the new millennium, in *Technical Proceedings of the ITSC-XII*, Lorne, Victoria, Australia.

Saunders, R. W. & K. T. Kriebel (1988), An improved method for detecting clear sky and cloudy radiances from AVHRR data, *International Journal of Remote Sensing*, *9*: 123–150.

Schiffer, R. A. & W. B. Rossow (1983), The International Satellite Cloud Climatology Project (ISCCP): The first project of the World Climate Research Programme, *Bulletin of the American Meteorological Society*, *64*: 779–784.

Schmetz, J., P. Pili, S. Tjemkes, D. Just, J. Kerkmann, S. Rota & A. Ratier (2002), An introduction to Meteosat Second Generation (MSG), *Bulletin of the American Meteorological Society*, *83*: 977–992.

Schüller, L., R. Bennartz, J. Fischer & J.-L. Brenguier (2005), An algorithm for the retrieval of droplet number concentration and geometrical thickness of stratiform marine boundary layer clouds applied to MODIS radiometric observations, *Journal of Applied Meteorology*, *44*: 28–38.

Schulze-Neuhoff, H. (1976), Nebelfeinanalyse mittels zusätzlicher 420 Klimastationen – Taktische Analyse 1:2 statt 1:5 Mill., *Meteorologische Rundschau*, *29*: 75–84.

Schumann, W., H. Stark, K. McMullan, D. M. A. Aminou & H.-J. Luhmann (2002), The MSG system, *ESA Bulletin*, *111*: 11–14.

Segelstein, D. J. (1981), *The complex refractive index of water*, M.S. thesis, University of Missouri – Kansas City, Department of Physics.

Seiz, G. & R. Davies (2006), Reconstruction of cloud geometry from multi-view satellite images, *Remote Sensing of Environment*, *100*: 143–149.

Shifrin, K. S. & G. Tonna (1993), Inverse problems related to light scattering in the atmosphere and ocean, *Advances in Geophysics*, *34*: 175–252.

Simmer, C., E. Raschke & E. Ruprecht (1982), A method for determination of cloud properties from two-dimensional histograms, *Annalen der Meteorologie*, *18*: 130–132.

Simpson, J. J., Z. Jin & J. R. Stitt (2000a), Cloud shadow detection under arbitrary viewing and illumination conditions, *IEEE Transactions on Geoscience and Remote Sensing*, *38*: 972–976.

Simpson, J. J., T. McIntire, Z. Jin & J. R. Stitt (2000b), Improved cloud top height retrieval under arbitrary viewing and illumination conditions using avhrr data, *Remote Sensing of Environment*, *72*: 95–110.

Slingo, A., R. Brown & C. L. Wrench (1982), A field study of nocturnal stratocumulus: III – High resolution radiative and microphysical observations, *Quarterly Journal of the Royal Meteorological Society*, *108*: 145–165.

Slingo, A. & H. M. Schrecker (1982), On the shortwave radiative properties of stratiform water clouds, *Quarterly Journal of the Royal Meteorological Society*, *108*: 407–426.

Snell, H. E., G. P. Anderson, J. Wang, J.-L. Moncet, J. H. Chetwynd & S. J. English (1995), Validation of FASE (FASCODE for the environment) and MODTRAN3: Updates and comparisons with clear-sky measurements, in *SPIE Conference 2578 Proceedings*, 194–204, Paris, France.

Sobrino, J. A. & M. Romaguera (2004), Land surface temperature retrieval from MSG1-SEVIRI data, *Remote Sensing of Environment*, *92*: 247–254.

Stamnes, K., S. C. Tsay, W. Wiscombe & K. Jayaweera (1988), Numerically stable algorithm for discrete-ordinate-method radiative transfer in multiple scattering and emitting layered media, *Applied Optics*, *27*: 2502–2509.

Stephens, G. L. (1979), Optical properties of eight water cloud types, *CSIRO Division of Atmospheric Physics technical paper 36*, CSIRO.

Stephens, G. L. (1994), *Remote Sensing of the Lower Atmosphere – An Introduction*, Oxford University Press, New York.

Stephens, G. L. (2005), Cloud feedbacks in the climate system: A critical review, *Journal of Climate*, *18*: 237–273.

Stephens, G. L. & P. J. Webster (1981), Clouds and climate: Sensitivity of simple systems, *Journal of the Atmospheric Sciences*, *38*: 235–247.

Stephenson, D. B. (2000), Use of the "odds ratio"for diagnosing forecast skill, *Weather and Forecasting*, *15*: 221–232.

Strabala, K. I., S. A. Ackerman & W. P. Menzel (1994), Cloud properties inferred from 8-12 μm data, *Journal of Applied Meteorology*, *33*: 212–229.

Taylor, G. I. (1917), The formation of fog and mist, *Quarterly Journal of the Royal Meteorological Society*, *43*: 241–268.

Taylor, J. P., M. D. Glew, J. A. C. Jr., W. R. Tahnk, S. Platnick, P. V. Hobbs & R. J. Ferek (2000), Effects of aerosols on the radiative properties of clouds, *Journal of the Atmospheric Sciences*, *57*: 2656–2670.

Thornes, J. E. & D. B. Stephenson (2001), How to judge the quality and value of weather forecast products, *Meteorological Applications*, *8*: 307–314.

Turner, J., R. Allam & D. Maine (1986), A case study of the detection of fog at night using channels 3 and 4 on the Advanced Very High Resolution Radiometer (AVHRR), *Meteorological Magazine*, *115*: 285–290.

Twomey, S. (1977a), The influence of pollution on the shortwave albedo of clouds, *Journal of the Atmospheric Sciences*, *34*: 1149–1152.

Twomey, S. (1977b), *Introduction to the Mathematics of Inversion in Remote Sensing and Indirect Measurements*, vol. 3 of *Developments in Geomathematics*, Elsevier Scientific, Amsterdam, The Netherlands.

Twomey, S. & T. Cocks (1982), Spectral reflectance of clouds in the near-infrared: Comparison of measurements and calculations, *Journal of the Meteorological Society of Japan*, *60*: 583–592.

Twomey, S. & T. Cocks (1989), Remotes sensing of cloud parameters from spectral reflectance in the near-infrared, *Beiträge zur Physik der Atmosphäre*, *62*: 172–179.

Ulivieri, C. (1985), Remote sensing of precipitable water by a thermal infrared multichannel approach, *Acta Astronautica*, *12*: 121–125.

Underwood, S. J., G. P. Ellrod & A. L. Kuhnert (2004), A multiple-case analysis of nocturnal radiation-fog development in the Central Valley of California utilizing the GOES nighttime fog product, *Journal of Applied Meteorology*, *43*: 297–311.

USGS (1993), Digital elevation models, *Data users' guide 5*, United States Geological Survey, Reston, Virginia, USA.

Vazquez, D. P., F. O. Reyes & L. A. Arboledas (1997), A comparative study of algorithms for estimating land surface temperature from AVHRR data, *Remote Sensing of Environment*, *62*: 215–222.

Vermote, E., D. Tanré, J. L. Deuzé, M. Herman & J. J. Morcrette (1997), Second Simulation of the Satellite Signal in the Solar Spectrum (6S). 6S user guide version 2, *Tech. rep.*.

Vogt, J., A. Viau & F. Paquet (1997), Mapping regional air temperature fields using satellite-derived surface skin temperatures, *International Journal of Climatology*, *17*: 1559–1579.

Walker, M. . (2003), The science of weather: Radiation fog and steam fog, *Weather*, *58*: 196–197.

Wan, Z. (1999), MODIS land-surface temperature algorithm theoretical basis document, *Atbd*, University of California.

Wanner, H. (1979), *Zur Bildung, Verteilung und Vorhersage winterlicher Nebel im Querschnitt Jura-Alpen*, vol. G7 of *Geographica Bernensia*, Geographisches Institut der Universität Bern, Bern, Switzerland.

Wanner, H. & S. Kunz (1983), Klimatologie der Nebel- und Kaltluftkörper im Schweizerischen Alpenvorland mit Hilfe von Wettersatellitenbildern, *Archives for Meteorology, Geophysics, and Bioclimatology*, *B33*: 31–56.

Warren, S. G. (1984), Optical constants of ice from the ultraviolet to the microwave, *Applied Optics*, *23*: 1026–1225.

Warren, S. G. & W. J. Wiscombe (1980), A model for the spectral albedo of snow. II: Snow containing atmospheric aerosols, *Journal of the Atmospheric Sciences*, *37*: 2734–2745.

Wehrli, C. (1985), Extraterrestrial solar spectrum, *Publications of the WRC 615*, World Radiation Center.

Wehrli, C. (1986), Spectral solar irradiance data, *WMO/TD 149*, WMO.

Welch, R. M. & B. A. Wielicki (1986), The stratocumulus nature of fog, *Journal of Climate and Applied Meteorology*, *25*: 101–111.

Wiegner, M., P. Seifert & P. Schlüssel (1998), Radiative effect of cirrus clouds in Meteosat Second Generation Spinning Enhanced Visible and Infrared Imager channels, *Journal of Geophysical Research*, *103*: 23217–23230.

Wieprecht, W., K. Acker, S. Mertes, J. Collett, W. Jaeschke, E. Bruggemann, D. Moller & H. Herrmann (2005), Cloud physics and cloud water sampler comparison during FEBUKO, *Atmospheric Environment*, *39*: 4267–4277.

Wilson, L. J. & W. R. Burrows (2004), Spatial verification using the relative operating characteristic curve, in *Proceedings of the 17th Conference on Probablity and Statistics in the Atmospheric Sciences*, 2.8.1–2.8.6, American Meteorological Society, Seattle, Washington, USA.

Winiger, M., M. Bachmann & J. Bendix (1992), Fog, air exchange and air quality in the alpine region. remote sensing applications in mountain climatology, *Erdkunde*, *46*: 188–202.

Wiscombe, W. J. & S. G. Warren (1980), A model for the spectral albedo of snow. I: Pure snow, *Journal of the Atmospheric Sciences*, *37*: 2712–2733.

WMO (1992), *International Meteorological Vocabulary*, vol. 182, World Meteorological Organization (WMO), Geneva, Switzerland, 2nd edn.

WMO (1995), *Manual on Codes – Volume I.1, International Codes*, 306, World Meteorological Organization (WMO), Geneva, Switzerland.

WMO (1996), *Guide to meteorological instruments and methods of observation*, vol. 8, World Meteorological Organization (WMO), Geneva, Switzerland, 6th edn.

Wright, B. J. & N. Thomas (1998), An objective visibility analysis and very-short-range forecasting system, *Meteorological Applications*, *5*: 157–181.

Wylie, D. P., D. Santek & D. O. Starr (1998), Cloud-top heights from GOES-8 and GOES-9 stereoscopic imagery, *Journal of Applied Meteorology*, *37*: 405–413.

Young, K. C. (1993), *Microphysical Processes in Clouds*, Oxford University Press, New York, Oxford.

Zhang, H. & T. Casey (2000), Verification of categorical probability forecasts, *Weather and Forecasting*, *15*: 80–89.

Zong, J. (1998), Geometric retrieval of cloud top height from MISR imagery, *Optical Remote Sensing of the Atmosphere and Clouds*, *3501*: 531–541.

Zong, J., R. Davies, J. P. Muller & D. J. Diner (2002), Photogrammetric retrieval of cloud advection and top height from the Multi-angle Imaging Spectroradiometer (MISR), *Photogrammetric Engineering and Remote Sensing*, *68*: 821–829.